The study of the formation and occurrence of metal(loid)-bearing nanoparticles in organic-rich colloids and particles within contaminated surficial soils in Rouyn Noranda, Quebec

by

Sarib Jadoon

A Thesis submitted to the Faculty of Graduate Studies of
The University of Manitoba
in partial fulfilment of the requirements of the degree of

MASTER OF SCIENCE

Department of Earth Sciences
University of Manitoba
Winnipeg

Abstract

Contamination of soils through deposition and alteration of metal(loid)-bearing particulate matter (PM) is a global problem. This study investigates the fate of Copper (Cu) in oxic organic-rich soil layers contaminated by mining and smelting operations around the Horne smelter, Rouyn Noranda, Quebec, Canada. The sequestration of Cu by organic colloids and particles is investigated by using column leaching experiments, ultra-centrifugation, focused ion beam technology (FIB), scanning electron microscopy (SEM), transmission electron microscopy (TEM) and atom probe tomography (APT). Cu occurs as nano-sized Cu-sulfides (CuS_x) phases within the matrix of micrometer-sized organic colloids and as nano-sized spinel phases such as Cu-Zn-bearing magnetite (Fe_3O_4) or nano-sized Cu-(hydr)oxides such as cuprite (Cu_2O) and spertiniite ($Cu(OH)_2$) within pre-mineralized organic matter (OM). The formation of these Cu-bearing NP is controlled by the porosity and occurrence of silicate phases, which mineralize the OM in multiple stages. Based on these observations models are developed for the sequestration of Cu by organic colloids and particles. The models include proposed mechanisms for (a) mineralization of OM, adsorption and distribution of ionic Cu-species and (b) nucleation and stabilization of nano-sized CuS_x, Cu-bearing spinels and Fe-(hydr)oxide phases. Here, diffusion of Cu and other metal(loid) species is promoted by the generation of porosity and nucleation of silicates during the mineralization of organic colloids and particles. Nucleation and formation of Cu-and Fe-bearing nanoparticles are promoted by the presence of hydrophilic silicate surfaces (which promote heterogeneous nucleation) and nanopores generated due to hydrodynamic properties of pore channels (which control the availability of metal(loid) species and pore size-controlled solubility effects (PCS). The characterization of OM with APT allowed for the first time the visualization of clusters of polymerized CuO_x polyhedra in smaller pore spaces of the OM. These clusters are considered precursors of nanoparticles and their occurrence in smaller pore spaces suggests that pore size and PCS strongly control the formation of Cu-bearing nanoparticles within OM.

Acknowledgements

I would like to start by thanking my supervisor, Dr. Michael Schindler, who meticulously guided me throughout my research, which could not be completed without his continuous support. As I experienced many new challenges researching a branch of geochemistry and mineralogy, I was not accustomed to, your patience and assistance were greatly appreciated. I also want to thank you for giving me the opportunity to work on this interesting project, allowing me to become familiar with the field of environmental nanoscience.

My sincere thanks go to my committee members, Dr. Feiyue Wang and Dr. Anton Chakhmouradian for their support and guidance. In addition, I would like to thank technicians at Manitoba Institute of Materials (Canada), Abdul Khan and Ravinder Sidu for their assistance with transmission electron microscopy (TEM) and scanning electron microscopy (SEM). I am also grateful to the associates at the Pacific Northwest National Laboratories (United States), Mark Wirth, Daniel Perrera, Odeta Qafoku and Libor Kovarik for help with focused ion beam (FIB) and atom probe tomography (APT).

Lastly, I am forever grateful to my mother Sobia Jadoon, my father Shoukat Naveed, my brother Saifullah Jadoon and my friends for their continuous prayers and support for me, which got me through stressful times of the Covid-19 pandemic.

Table of Contents

List of Figures

List of Appendices

List of Abbreviations

APT, Atom Probe Tomography

BF, Bright Field

BSE, Backscattering Electron

DOM, Dissolved Organic Matter

EDS, Electron Dispersive X-Ray Spectroscopy

Eh, Reduction Potential

FA, Fulvic Acids

FFT, Fast Fourier Transformations

FIB, Focused Ion Beam

HA, Humic Acids

HAADF, High Angle Annular Dark Field

HS, Humic Substances

ICP-MS, Inductively Coupled-Plasma Mass Spectrometry

NP, Nanoparticles

INP, Incidental nanoparticles

OM, Organic Matter

PM, Particulate Matter

PZC, Point of Zero Charge

SAED, Selected Area Electron Diffraction

SEM, Scanning Electron Microscopy

SOM, Soil Organic Matter

STEM, Scanning-Transmission Electron Microscopy

TEM, Transmission Electron Microscopy

XRD, X-ray Diffraction

Chapter 1: Introduction

1.1. Soil contamination by mining-related activities

Mining and smelting operations have contaminated different environmental components around the world (Nriagu, 1996). Pollutants released from these operations are mostly metal(loid)-bearing aerosols (It is defined as collection of suspended particles and the surrounding gases) and particulate matter (It is defined as suspended solid or liquid matter that will settle down eventually with time) (PM) (Knight & Henderson, 2006). Although many studies focused on the characterization of the extent of contamination (total concentration levels of metal(loid)s) and type of contamination (type of metal(loid)s) (Adamo et al., 1996; Henderson et al., 1998), bio-availability of metal(loid)s (Rieuwerts, 2007; Ettler et al., 2012) and processes that govern the interaction of metal(loid)s with soil constituents (Lanteigne et al., 2012; Lanteigne et al., 2014; Ettler et al., 2016; Schindler et al., 2016), we still lack knowledge on chemical and mineralogical processes in pore spaces formed during weathering of minerals and organic matter.

1.1.1 Particulate matter emitted by smelter

The chemical and mineralogical composition of PM has been characterized in many studies but still, processes that control it's interaction with other soil constituents are the focus of many environmental studies (Lanteigne et al., 2012; Schindler & Hochella, 2017; Schindler et al., 2021). Various reclamation methods are used in smelter-impacted areas but the effective application of these remediation methods requires an understanding of the cycling of the emitted elements in a soil environment (Mantha et al., 2019). Hence, we need to better understand the environmental fate of elements released during the weathering of PM, specifically factors that control their mobility and sequestration such as adsorption, diffusion, nucleation and dissolution processes within pore spaces (Mantha et al., 2019).

The gaseous condensation and cooling processes during smelting operations mostly result in the formation of smelter-derived PM (Samuelsson & Björkman, 1998). Before the onset of environmental regulations, smelters did not use filters to curb the release of metal(loid)-bearing PM (Henderson et al., 1998). A small fraction of PM was released even after the installation of filters at times of their degradation (Ettler et al., 2016). Micrometer-size PM released during smelting operation is spherical in shape, has high-temperature features such as tabular, skeletal, porphyritic and dendritic patterns (Lanteigne et al., 2012). The composition, structure and the

metal(loid) content of the PM depend on the furnace temperatures, ore processing methods used and the composition of the ore processed within the smelter (Knight & Henderson, 2006). The extent of the metal(loid) released from PM during weathering in a soil environment is therefore dependent on the ore composition as well as the processing methods used within the smelter.

1.1.2 Particulate matter deposition

Upon release of metal(loid)-bearing PM in the atmosphere, the extent of spatial coverage depends on the particle size and wind speed/direction (Ettler et al., 2005; Csavina et al., 2012). PM of small size has the tendency to travel greater distances as compared to their large counterparts; however, structural obstacles such as trees or buildings can shorten their travel distance (Ettler et al., 2005). Various physico-chemical processes can occur after the deposition of PM into the surficial soils and these processes are dependent on the composition as well as the surrounding environmental conditions, which are mostly dependent on the pH, Eh and the availability of complexing agents (Schindler & Hochella, 2017; Mantha et al., 2019; Schindler et al., 2019). Surficial layers of soils mostly retain the metal(loid)s released during the weathering of the PM (Spiers et al., 2004; Mantha et al., 2019). The concentrations of the released elements commonly decrease exponentially in a soil-depth profile impacted by deposited PM. A considerable portion of metal(loid)s released from the PM is temporarily retained by various hosts in the soil and is thus not bioavailable. However, the metal(loid)s are released over time by their hosts (Mantha et al., 2019), and their speciation will then depend on the chemical and mineralogical processes which occurred in the pore spaces of their original host.

1.2. The smelter-impacted soils at Rouyn-Noranda (Horne Smelter)

The study area extends around the city limits of Rouyn-Noranda, Quebec and surrounds the Horne smelter, which is considered a critical emission source of PM contaminated with heavy metal(loid)s. The ore processed at the Horne smelter included sphalerite, pyrite, galena, pyrrhotite, chalcopyrite and magnetite, as well as native silver and gold (Kerr & Gibson, 1993) with pyrite, pyrrhotite, chalcopyrite and magnetite comprising up to 85% of the mass (Denis, 1933). In the period of 1927 to 1976, the smelter has released PM containing Ni, Pb, Zn, Cu and Cd with a peak value of more than 1.5 million metric tons in 1965. The implementation of pollution controls in 1970 greatly reduced the annual emission of PM (Kettles & Bonham-Carter, 2002). After 1976, the smelter processed predominantly electronic waste containing base metal(loid)s such as Cu.

The environmental impact of the smelting activities in Rouyn Noranda has been addressed in numerous geochemical, mineralogical and biological studies focused on the concentrations and speciation of metal(loid)s in soils, lakes, rock coatings, snow samples and biota (Bonham-Carter et al., 2006; Knight & Henderson, 2006; Telmer et al., 2006; Zdanowicz et al., 2006; Masson et al., 2010; Caplette et al., 2015; Dinis et al., 2020). Telmer et al. (2006) sampled 99 lakes surrounding the Horne smelter and detected extensive smelter impact in lakes located within 50 km of the point source. They reported no obvious correlation between metal(loid)s concentrations and lake pH, morphology, and surrounding bedrock geology but element ratios suggested recycling and remobilization of metal(loid)s with time. The source apportionment of metal(loid) contamination in peat, snow, humus and lakes surrounding the Horne smelter indicated contribution from the smelter within 75 km of the point source but the differentiation between the smelter and non-smelter sources of metal(loid)s became difficult as the distance from smelter increases (Bonham-Carter et al., 2006). Dinis et al. (2020) used tree-ring dating in the Rouyn Noranda area to study the bioavailability of the metal(loid)s Zn and Mg with time. Their study indicated a reduction in the bioavailability of metal(loid)s after the government imposed regulations in the 1970s.

Banic et al. (2006), Zdanowicz et al. (2006) and Knight & Henderson (2006) characterized the chemical and mineralogical composition of metal(loid)s in air, snow and soil samples around the Horne Smelter. They showed that PM emitted from the smelter can be composed of Fe-Cu-Zn- bearing sulfides and spherical PM composed of silicates and oxides. Knight & Henderson (2006) proposed that micrometer spherical PM is very resistant to weathering and hardly contributes to the metal(loid) concentrations in humus, whereas the majority of Cu, Zn and Pb metal(loid) phases in humus originated from weathered and altered nanometer-sized aerosols. Caplette et al. (2015) showed that black rock coatings occur within 6 km of the point source. The coatings contain chemical and mineralogical footprints of the smelter emissions between 1927 and 1975 and are predominantly composed of Cu-Zn-Fe-spinels (mostly oxide spinels such as cuprospinel), Pb-sulfates, Pb-silicates, Fe-(hydr)oxides and minerals from the surrounding bedrocks, which have been preserved for decades and are quite resistant to physical and chemical weathering. The coating thickness decreases as a function of distance from smelter, which indicates that a greater deposition of sulfuric acid and PM resulted in the enhanced weathering of the underlying bedrock and PM (Caplette et al., 2015).

1.3. Interaction of soil components with metal(loid) species

Deposition of metal(loid)-bearing PM by aeolian processes leads to their enrichment of the metal(loid)s in the surface layers of the soils. Weathering of the PM results in the release of the metal(loid)s in the pore solutions. Various constituents present in the soil bind the metal(loid)s through different processes (Thompson & Goyne, 2012). Adsorption of metal(loid)s on the surface of mineral grains can take place by both physical and chemical interactions. Physical interactions including binding through van der waals forces lead to the formation of outer-sphere complexes, which are weak and irreversible, whereas chemical interactions (formation of chemical bonds) lead to the formation of inner-sphere complexes, which are relatively stronger than outer-sphere complexes (Sparks, 2003; Thompson & Goyne, 2012). The adsorption mechanisms are mostly dependent on environmental factors such as pH, Eh and ionic strength as well as the point of zero charge (PZC) of substrate and sorbent. The PZC of any particular phase dictates its surface charge and is mostly dependent on the pH of the surrounding environment and the type and concentration of electrolytes present in the pore solution (Mantha et al., 2019).

In organic-rich soils, organic matter (OM) can serve as a sorbent for metal(loid)s (Caporale & Violante, 2016). This ability of OM to sorb metal(loid)s depends on the type of OM and on the ratio between the total surface area of minerals versus OM (Adamo et al., 1996; Gustafsson et al., 2003; Neagoe et al., 2012). An important group of meta(loid)-complexing organic molecules are humic substances (HS) such as humin, fulvic and humic acids which form during the decomposition of natural soil organic matter (SOM). The extent of binding and formation of metal(loid)-HS complexes depends on local environmental conditions and other factors such as pH, ionic strength and origin/type of HS (Alloway, 2012; Pham et al., 2012). As OM has PZC values of between 2 and 3, it has a negative surface charge at pH values typical for soils (pH > 4.5). This results in a strong interaction between cationic species and OM surfaces. Many studies indicate that Cu ionic species such as Cu^{2+} are sequestered by organics; however, synchrotron-based spectroscopy and diffraction studies have not provided a uniform picture of the fate of Cu in surficial soils containing minerals and OM. For example, some studies state that Cu predominantly sorbs to OM (Strawn & Baker, 2007; Thomasi et al., 2015), whereas other work reports a close association of Cu with Fe-(hydr)oxides (Li et al., 2006; Yang et al., 2014). The latter observations indicate uncertainty with respect to the fate of metal(loid)s in contaminated surficial soil horizons containing organic particles, colloids and inorganic phases. Mantha et al.

(2019) showed that Cu is sequestered as covellite (CuS) nanoparticles (NP) within the nanopores of OM colloids and particles. These authors argued that some of the pores may be confined and act as nano- to micrometer-sized anoxic environments within a surficial (oxic) environment. However, there is still a lack of knowledge regarding processes that control the nucleation of metal(loid)-bearing NP within OM colloids and particles in contaminated oxic soils.

1.4. Research objectives

As discussed above, bulk analytical techniques could not provide an unequivocal answer with respect to the sequestration of Cu in contaminated organic-rich soils. Hence, there is a need for probing Cu-bearing OM colloids and particles at the atomic to micrometer scale, which will provide a better understanding of the mechanisms that govern the sequestration of Cu in organic-rich soils surrounding a smelter stack. The overall aim of this M.Sc. thesis is therefore to identify underlying mechanisms that control the sequestration of Cu in OM colloids and particles.

Hence, the objectives of this thesis are to examine whether:

a) The sequestration of metal(loid)s occurs via the formation of nanoparticles in the pore spaces of the colloids and particles;
b) The retention of Cu by OM is also controlled by the occurrence of other phases present in OM such as Fe-(hydr)oxides and silicates;
c) Pore space and pore size effects such as an increasing solubility of precipitates control the nucleation of Cu-bearing phases within OM;

1.5. Summary of key characterization methods

1.5.1. Scanning electron microscopy (SEM)

Scanning electron microscopy (SEM) is now a routine technique for imaging geological material due to its larger depth of field, strong stereoscopic vision, high magnification and high resolution (Smith & Oatley, 1955; Wen et al., 2021). It uses a focused beam of high-energy electrons that interact with the surface of a specimen to generate a variety of signals (secondary electrons, backscattered electrons and characteristic X-rays) that reveal information about the surface morphology, atomic density and chemical composition of material under observation (Smith & Oatley, 1955; Wen et al., 2021). Secondary electrons and backscattering electrons are can be used for the imaging of organic and inorganic material: secondary electron images depict

the surface topography and morphology, whereas backscattered electron images visualize contrasts in atomic densities. Energy dispersive spectroscopy are commonly used to record chemical maps or to analyze the chemical composition of small areas (spot analyses). Both analysis techniques are useful for studying the chemical composition and spatial distribution of metal(loid)s (Smith & Oatley, 1955; Wen et al., 2021).

1.5.2. Transmission electron microscopy (TEM)

The characterization of soil samples with transmission electron microscopy (TEM) provides information on environmental processes occurring at the nano-scale (Yang et al., 2015; Schindler & Hochella Jr, 2016). The technique is not typically used for the characterization of environmental samples due to the high cost of sample preparation and operation. A TEM instrument can operate in either TEM mode or in both TEM and Scanning transmission electron microscopy (STEM) hybrid mode (Phillips & Williams, 2009).

In a TEM instrument, a beam of electrons is transmitted through the material under investigation, which is then magnified, refocused and projected on a phosphor screen. This results in the conversion of an electron image into a visible image (Phillips & Williams, 2009). TEM spatial resolution ranges from 0.1 to 0.2 nm and only allows analysis of samples that are less than 100 nm thick (Phillips & Williams, 2009). The 2D images obtained from TEM provide information on the size, shape and morphology of the material under observation (Mantha et al., 2019). By controlling the aperture of the objective lens, both bright and dark field images can be produced. In brightfield mode, the scattering of the direct beam by atoms in the sample results in images where areas of higher atomic density appear darker than those of lower atomic density. In darkfield mode, the scattered incident electrons are used to produce an image (so called dark field image) in which areas of higher-atomic density appear brighter than those of lower atomic density (Williams & Carter, 1996). In STEM mode, an area under observation is scanned with a highly focused beam of electrons. The scattered electrons are detected by a high angle dark field (HAADF) detector and produce a three-dimensional image by yielding Z-contrast in final reconstructions (Jesson & Pennycook, 1995; Zhong et al., 2016). X-rays emitted by the sample in the STEM mode produce an energy-dispersive X-ray spectrum (EDS), which is used to quantify the chemical composition of a sample and to generate chemical distribution maps of elements (Loretto, 1984; Kosasih et al., 2021).

Electron diffraction patterns are generated in TEM mode upon removal of the objective aperture. Here, both transmitted and diffracted electron beams are allowed to pass through the instrument column and the constructive inference between diffracted electron beams results in the generation of a diffraction pattern (Loretto, 1984). In addition, a selected area aperture can be used to limit the diffraction pattern to a certain region, which allows the identification of NP or aggregates as small as 200 nm in diameter.

1.5.3. Atom Probe Tomography (APT)

APT is a destructive analytical technique that is capable to position and identify almost every atom in a specimen. APT data acquisition utilizes time-of-flight mass spectrometry to generate a large dataset comprising several million individual atoms in a 3D spatial coordinate system (Reddy et al., 2020). APT systems utilize either ultra-fast voltage or laser pulses to erode the atoms located at the tip of a needle-shaped specimen and convert them into charged ions by a process known as field evaporation. An electric field accelerates these ions towards a position-sensitive detector that registers the time of flight and impact position of each individual ion (Reddy et al., 2020).

The energy applied to the surface of a specimen is already known and can be used to calculate each ion's mass-to-charge ratio based on its travel time, which is in most cases sufficient for the identification of an individual atom. Impact positions on the position-sensitive-detector plot the locations of individual atoms. The location and identity of individual atoms can be used to calculate a 3D plot which has both, the chemical composition and atomic structure of the specimen at nanoscale and can serve as a powerful tool to examine interfaces between different regions (Saxey et al., 2018; Reddy et al., 2020).

1.6. M.Sc. thesis structure

This M.Sc. thesis is written in the grouped manuscript style (sandwich thesis), following the guidelines of the Faculty of Graduate Studies and Department of Earth Sciences at the University of Manitoba. The first chapter of this thesis (i.e., the current chapter) contains an introduction to the research topics, study site description, research objectives and the general outline of the thesis. Chapters 2 and 3 are the major data chapters of this thesis and have been structured as two manuscripts.

- Chapter 2 describes the characterization of colloidal OM and focuses on the research objectives (a, b and c) outlined in Section 1.4. This chapter has been submitted to *Environmental Science: Nano* journal, where it has been accepted with major revisions.
- Chapter 3 describes the characterization of OM particles using a combination of TEM and APT and also focuses on the research objectives (a, b and c) outlined in Section 1.4. It is ready for submission.

Chapters 2 and 3 have been reformatted from the submitted or submission ready versions for inclusions in the thesis. Chapter 4 provides an overall conclusion and recommendations for future research.

1.7. References

Adamo, P., Dudka, S., Wilson, M., & McHardy, W. (1996). Chemical and Mineralogical Forms of Cu and Ni in Contaminated Soils from the Sudbury Mining and Smelting Region, Canada. *Environmental Pollution, 91*(1), 11-19.

Alloway, B. J. (2012). *Heavy Metals in Soils: Trace Metals and Metalloids in Soils and Their Bioavailability* (Vol. 22): Springer Science & Business Media.

Banic, C., Leaitch, W. R., Strawbridge, K., Tanabe, R., Wong, H., Gariépy, C., Simonetti, A., Nejedly, Z., Campbell, J. I., & Lu, J. (2006). The Physical and Chemical Evolution of Aerosols in Smelter and Power Plant Plumes: An Airborne Study. *Geochemistry: Exploration, Environment, Analysis, 6*(2-3), 111-120.

Bonham-Carter, G., Henderson, P., Kliza, D., & Kettles, I. (2006). Comparison of Metal Distributions in Snow, Peat, Lakes and Humus around a Cu Smelter in Western Quebec, Canada. *Geochemistry: Exploration, Environment, Analysis, 6*(2-3), 215-228.

Caplette, J. N., Schindler, M., & Kyser, T. K. (2015). The Black Rock Coatings in Rouyn-Noranda, Québec: Fingerprints of Historical Smelter Emissions and the Local Ore. *Canadian Journal of Earth Sciences, 52*(11), 952-965.

Caporale, A. G., & Violante, A. (2016). Chemical Processes Affecting the Mobility of Heavy Metals and Metalloids in Soil Environments. *Current Pollution Reports, 2*(1), 15-27.

Csavina, J., Field, J., Taylor, M. P., Gao, S., Landázuri, A., Betterton, E. A., & Sáez, A. E. (2012). A Review on the Importance of Metals and Metalloids in Atmospheric Dust and Aerosol from Mining Operations. *Science of The Total Environment, 433*, 58-73.

Denis, F. T. (1933). An Investigation of the Mineral Composition of the Ores of Noranda Mines Ltd. *McGill University Libraries*.

Dinis, L., Bégin, C., Savard, M. M., & Parent, M. (2020). Impacts of Smelter Atmospheric Emissions on Forest Nutrient Cycles: Evidence from Soils and Tree Rings. *Science of The Total Environment*, 141427.

Ettler, V., Johan, Z., Kříbek, B., Veselovský, F., Mihaljevič, M., Vaněk, A., Penížek, V., Majer, V., Sracek, O., & Mapani, B. (2016). Composition and Fate of Mine-and Smelter-Derived Particles in Soils of Humid Subtropical and Hot Semi-Arid Areas. *Science of The Total Environment, 563*, 329-339.

Ettler, V., Kříbek, B., Majer, V., Knésl, I., & Mihaljevič, M. (2012). Differences in the Bioaccessibility of Metals/Metalloids in Soils from Mining and Smelting Areas (Copperbelt, Zambia). *Journal of Geochemical Exploration, 113*, 68-75.

Ettler, V., Vaněk, A., Mihaljevič, M., & Bezdička, P. (2005). Contrasting Lead Speciation in Forest and Tilled Soils Heavily Polluted by Lead Metallurgy. *Chemosphere, 58*(10), 1449-1459.

Gustafsson, J. P., Pechová, P., & Berggren, D. (2003). Modeling Metal Binding to Soils: The Role of Natural Organic Matter. *Environmental Science & Technology, 37*(12), 2767-2774.

Henderson, P., McMartin, I., Hall, G., Percival, J., & Walker, D. (1998). The Chemical and Physical Characteristics of Heavy Metals in Humus and Till in the Vicinity of the Base Metal Smelter at Flin Flon, Manitoba, Canada. *Environmental Geology, 34*(1), 39-58.

Jesson, D., & Pennycook, S. J. (1995). Incoherent Imaging of Crystals Using Thermally Scattered Electrons. *Proceedings of the Royal Society of London. Series A: Mathematical and Physical Sciences, 449*(1936), 273-293.

Kerr, D. J., & Gibson, H. L. (1993). A Comparison of the Horne Volcanogenic Massive Sulfide Deposit and Intracauldron Deposits of the Mine Sequence, Noranda, Quebec. *Economic Geology, 88*(6), 1419-1442.

Kettles, I. M., & Bonham-Carter, G. F. (2002). Modelling Dispersal of Metals from a Copper Smelter at Rouyn-Noranda (Québec, Canada) Using Peatland Data. *Geochemistry: Exploration, Environment, Analysis, 2*(2), 99-110.

Knight, R., & Henderson, P. (2006). Smelter Dust in Humus around Rouyn-Noranda, Quebec. *Geochemistry: Exploration, Environment, Analysis, 6*(2-3), 203-214.

Kosasih, F. U., Cacovich, S., Divitini, G., & Ducati, C. (2021). Nanometric Chemical Analysis of Beam-Sensitive Materials: A Case Study of Stem-Edx on Perovskite Solar Cells. *Small Methods, 5*(2), 2000835.

Lanteigne, S., Schindler, M., & McDonald, A. (2014). Distribution of Metals and Metalloids in Smelter-Derived Particulate Matter in Soils and Mineralogical Insights into Their Retention and Release in a Low-T Environment. *The Canadian Mineralogist, 52*(3), 453-471.

Lanteigne, S., Schindler, M., McDonald, A. M., Skeries, K., Abdu, Y., Mantha, N. M., Murayama, M., Hawthorne, F. C., & Hochella, M. F. (2012). Mineralogy and Weathering of Smelter-Derived Spherical Particles in Soils: Implications for the Mobility of Ni and Cu in the Surficial Environment. *Water, Air, & Soil Pollution, 223*(7), 3619-3641.

Li, W., Zhang, S., Jiang, W., & Shan, X.-q. (2006). Effect of Phosphate on the Adsorption of Cu and Cd on Natural Hematite. *Chemosphere, 63*(8), 1235-1241.

Loretto, M. (1984). Analysis of Micrographs in Tem, Stem, Hrem and Sem *Electron Beam Analysis of Materials* (pp. 113-152): Springer.

Mantha, H., Schindler, M., & Hochella, M. F. (2019). Occurrence and Formation of Incidental Metallic Cu and Cus Nanoparticles in Organic-Rich Contaminated Surface Soils in Timmins, Ontario. *Environmental Science: Nano, 6*(1), 163-179.

Masson, S., Couillard, Y., Campbell, P. G., Olsen, C., Pinel-Alloul, B., & Perceval, O. (2010). Responses of Two Sentinel Species (Hexagenia Limbata—Mayfly; Pyganodon Grandis—Bivalve) Along Spatial Cadmium Gradients in Lakes and Rivers in Northwestern Québec. *Journal of Environmental Monitoring, 12*(1), 143-158.

Neagoe, A., Iordache, V., & Fărcăşanu, I. C. (2012). The Role of Organic Matter in the Mobility of Metals in Contaminated Catchments *Bio-Geo Interactions in Metal-Contaminated Soils* (pp. 297-325): Springer.

Nriagu, J. O. (1996). A History of Global Metal Pollution. *Science, 272*(5259), 223-223.

Pham, A. N., Rose, A. L., & Waite, T. D. (2012). Kinetics of Cu (Ii) Reduction by Natural Organic Matter. *The Journal of Physical Chemistry A, 116*(25), 6590-6599.

Phillips, G. O., & Williams, P. A. (2009). *Handbook of Hydrocolloids*: Elsevier.

Reddy, S. M., Saxey, D. W., Rickard, W. D., Fougerouse, D., Montalvo, S. D., Verberne, R., & Van Riessen, A. (2020). Atom Probe Tomography: Development and Application to the Geosciences. *Geostandards and Geoanalytical Research, 44*(1), 5-50.

Rieuwerts, J. S. (2007). The Mobility and Bioavailability of Trace Metals in Tropical Soils: A Review. *Chemical Speciation & Bioavailability, 19*(2), 75-85.

Samuelsson, C., & Björkman, B. (1998). Dust Forming Mechanisms in the Gas Cleaning System after the Copper Converting Process:(Ii). Thermodynamic Studies. *Scandinavian Journal of Metallurgy, 27*(2), 64-72.

Saxey, D., Moser, D., Piazolo, S., Reddy, S., & Valley, J. (2018). Atomic Worlds: Current State and Future of Atom Probe Tomography in Geoscience. *Scripta Materialia, 148*, 115-121.

Schindler, M., & Hochella Jr, M. F. (2016). Nanomineralogy as a New Dimension in Understanding Elusive Geochemical Processes in Soils: The Case of Low-Solubility-Index Elements. *Geology, 44*(7), 515-518.

Schindler, M., & Hochella, M. F. (2017). Sequestration of Pb–Zn–Sb-and as-Bearing Incidental Nanoparticles by Mineral Surface Coatings and Mineralized Organic Matter in Soils. *Environmental Science: Processes & Impacts, 19*(8), 1016-1027.

Schindler, M., Lanteigne, S., McDonald, A. M., & Hochella Jr, M. F. (2016). Evidence of Cu-and Ni-Bearing Surface Precipitates and Adsorption Complexes in Remediated Soils at the Nanoscale: A Tem, Micro-Raman, and Laser-Ablation Icp-Ms Study of Mineral Surface Coatings. *The Canadian Mineralogist, 54*(1), 285-309.

Schindler, M., Mantha, H., & Hochella, M. F. (2019). The Formation of Spinel-Group Minerals in Contaminated Soils: The Sequestration of Metal (Loid) S by Unexpected Incidental Nanoparticles. *Geochemical Transactions, 20*(1), 1.

Schindler, M., Santosh, M., Dotto, G., Silva, L. F., & Hochella Jr, M. F. (2021). A Review on Pb-Bearing Nanoparticles, Particulate Matter and Colloids Released from Mining and Smelting Activities. *Gondwana Research*.

Smith, K., & Oatley, C. (1955). The Scanning Electron Microscope and Its Fields of Application. *British Journal of Applied Physics, 6*(11), 391.

Sparks, D. L. (2003). *Environmental Soil Chemistry*: Elsevier.

Spiers, G., Hawson, C., & Prevost, F. (2004). Metal Levels in the Soils of the Sudbury Smelter Footprint. *A Report To: Safety, Health and Environment, INCO Ltd., Ontario Division,*

Copper Cliff, ON. P0M 1N0 and Falconbridge Ltd., Sudbury Smelter Business Unit, Falconbridge, ON. P0M 1S0. Submitted: July, 12, 2004.

Strawn, D. G., & Baker, L. L. (2007). Speciation of Cu in a Contaminated Agricultural Soil Measured by Xafs, M-Xafs, and M-Xrf. *Environmental Science & Technology, 42*(1), 37-42.

Telmer, K. H., Daneshfar, B., Sanborn, M. S., Kliza-Petelle, D., & Rancourt, D. G. (2006). The Role of Smelter Emissions and Element Remobilization in the Sediment Chemistry of 99 Lakes around the Horne Smelter, Quebec. *Geochemistry: Exploration, Environment, Analysis, 6*(2-3), 187-202.

Thomasi, S., Fernandes, R., Fontes, R., & Jordão, C. (2015). Sequential Extraction of Copper, Nickel, Zinc, Lead and Cadmium from Brazilian Oxysols: Metal Leaching and Metal Distribution in Soil Fractions. *International Journal of Environmental Studies, 72*(1), 41-55.

Thompson, A., & Goyne, K. (2012). Introduction to the Sorption of Chemical Constituents in Soils. *Nature Education Knowledge, 4*(4), 7.

Wen, S., Liu, J., & Deng, J. (2021). Methods for the Detection and Composition Study of Fluid Inclusions. *Fluid Inclusion Effect in Flotation of Sulfide Minerals*, 27-68.

Williams, D. B., & Carter, C. B. (1996). The Transmission Electron Microscope *Transmission Electron Microscopy* (pp. 3-17): Springer.

Yang, J., Liu, J., Dynes, J. J., Peak, D., Regier, T., Wang, J., Zhu, S., Shi, J., & John, S. T. (2014). Speciation and Distribution of Copper in a Mining Soil Using Multiple Synchrotron-Based Bulk and Microscopic Techniques. *Environmental Science and Pollution Research, 21*(4), 2943-2954.

Yang, Y., Colman, B. P., Bernhardt, E. S., & Hochella, M. F. (2015). Importance of a Nanoscience Approach in the Understanding of Major Aqueous Contamination Scenarios: Case Study from a Recent Coal Ash Spill. *Environmental science & technology, 49*(6), 3375-3382.

Zdanowicz, C. M., Banic, C. M., Paktunc, D. A., & Kliza-Petelle, D. A. (2006). Metal Emissions from a Cu Smelter, Rouyn-Noranda, Quebec: Characterization of Particles Sampled in Air and Snow. *Geochemistry: Exploration, Environment, Analysis, 6*(2-3), 147-162.

Zhong, Z., Goris, B., Schoenmakers, R., Bals, S., & Batenburg, K. J. (2016). *3d Structure and Chemical Composition Reconstructed Simultaneously from Haadf-Stem Images and Eds-Stem Maps.* Paper presented at the European Microscopy Congress 2016: Proceedings.

Chapter 2: The role of nanopores within organic colloids in the sequestration and mobilization of Copper within contaminated oxic soils

Abstract

Major emitters of Cu are smelters and coal-power plants, which cause severe damages to the health of soils and aquatic systems as elevated Cu concentrations are toxic for terrestrial and aquatic organisms. Toxic effects and long-term environmental fate of Cu depend among many other factors on its speciation in soil and water bodies. This study explores the role of nanopores within organic (OM) colloids in the sequestration of Cu in contaminated oxic soils around the Horne smelter, Rouyn Noranda, Quebec, Canada. The sequestration and mobilization of Cu by porous OM colloids is studied using a combination of column leaching experiments, ultra-centrifugation and transmission electron microscopy (TEM). TEM analysis indicates that Cu occurs as nano-sized CuS_x phases in nanopores of micrometer-sized OM colloids, an observation that can easily be overlooked during analysis through bulk-scale examination tools such as X-ray diffraction and synchrotron-based spectroscopic methods. The nano-sized CuS_x phases occur along the rim of OM colloids or heterogeneously nucleate on silica inclusions located within nanopores of OM colloids, indicating their nucleation is strongly controlled by porosity and permeability. The proportion of Cu-Fe-bearing colloids in the soil leachates ranges from 20 to 40% of the total colloidal fraction, which suggests that sequestration of metal(loid)s within nanopores of OM colloids can play a vital role in the long-term stability of nano-sized CuS_x phases in an oxic surficial environment. Based on these observations, a model for the sequestration process of Cu by OM is developed. This model includes proposed underlying mechanisms for (a) adsorption and diffusion of ionic Cu-species and (b) nucleation and stabilization of nano-sized CuS_x and Fe-(hydr)oxide phases. Here, diffusion of Cu-species and nucleation of nano-sized CuS_x phases is promoted through the generation of porosity during pre-mineralization of OM colloids via the formation of Fe-(hydr)oxide and silica phases. Nucleation of nano-sized CuS_x phases occurs through reduction of Cu and S species by humic and fulvic acids. The presence of sulfide and silicate species in the OM plays most likely a vital role in inhibiting the transformation of CuS_x and ferrihydrite to metallic Cu and goethite or hematite, respectively.

2.1. Introduction

In organic-rich soils, organic matter (OM) and especially OM colloids can serve as a sorbent for metal(loid)s (Caporale & Violante, 2016), this ability of OM to serve as sorbent depends on the type of OM and on the ratio between the total surface area of minerals versus total surface area of OM. An important group of metal(loid)-complexing organic molecules are humic substances (HS) such as fulvic acids (FA) and humic acids (HA), which form during the decomposition of natural soil OM. The extent of binding and formation of metal(loid)-HS complexes depends on local environmental conditions and other factors such as pH, ionic strength and origin/type of HS (Alloway, 2012; Pham et al., 2012).

OM colloids mostly include organic biopolymers formed by the disintegration of organic remains in soil (Kretzschmar & Schafer, 2005). They include humic and fulvic acids, exocellular biopolymeric material, polysaccharides and biocolloids (including bacteria and viruses) (Kretzschmar & Schafer, 2005). These OM colloids are not crystalline in nature and contain long chains and rings of Carbon (C) bonded to Hyrdogen (H), Oxygen (O) and Nitrogen (N) (Wilkinson et al., 1997). They have a high cation exchange capacity and usually, a negative surface charge as their point of zero charge is between pH = 2 and 3 (Kretzschmar & Schafer, 2005). They have diverse surface reactive sites ranging from cationic amino groups ($R\text{-}NH_2$) to anionic hydroxyls (R-OH) and carboxylic groups (R-COOH) and the neutral aromatic and aliphatic moieties (Thompson & Goyne, 2012) OM in colloids is considered an effective sorbent and carrier of heavy metal(loid)s in aqueous environments due to its strong affinity towards metal(loid)s such as Cd, Cu and Ni (Dai et al., 1995; Oursel et al., 2013) Hence, sequestration and mobilization of metal(loid)s via OM colloids greatly affect their bio-availability, natural cycling and transport in various surficial environments (Hartland et al., 2015; Lee et al., 2019). For example, Grolimund & Borkovec (2005), Denaix et al. (2001) and Schindler et al. (2021) showed that the transport of Pb in surficial contaminated soils is predominantly facilitated by organic- and inorganic-based colloids.

In surficial contaminated soils, Cu occurs in the form of Cu-bearing particulate matter (PM), Cu-bearing colloids (organic and inorganic) and Cu aqueous species in soil pore-solutions. Cu-bearing nanoparticles and colloids have been observed in various anoxic environments such as in flooded soils (Weber et al., 2009; Hofacker et al., 2013a; Hofacker et al., 2013b), anaerobic

wetlands (Gammons & Frandsen, 2001), clay minerals (Ilton & Veblen, 1988; Ilton et al., 1992; Ilton & Veblen, 1993; Ahn et al., 1997; Suárez et al., 2011) and anoxic solutions (Hoffmann et al., 2020). Hoffmann et al. (2020) explored the effect of natural OM on the stability, growth and dissolution of Cu-sulfide nanoparticles under anoxic and oxic environments. The authors showed that these nanoparticles could persist under oxic conditions for at least 22 days. This is in accord with spectroscopy studies which showed that CuS_x aqueous species exist in natural oxic surface waters (Rozan et al., 2000).

The speciation of Cu and its adsorption on mineral surfaces depends on the chemical composition of the porewater as well as on its pH, Eh and ionic strength and the mineralogical composition of its environment. For example, classical sequential-extraction methods of organic-rich soils have suggested that organic material can be an important (even dominant) sorbent for Cu in the surface horizons of soils, depending on the type of OM, and the ratio between the total surface areas of OM and minerals (Adamo et al., 1996; Gustafsson et al., 2003; Mantha et al., 2019). Furthermore, synchrotron-based spectroscopy and diffraction studies showed that Cu is associated with both OM (Strawn & Baker, 2007; Thomasi et al., 2015) and Fe-(hydr)oxides (Li et al., 2006). Mantha et al. (2019) explored for the first time the nano-mineralogical composition of OM colloids in Cu-contaminated surficial oxic soils. The authors showed that Cu is sequestrated as covellite (CuS) nanoparticles within the nanopores of OM colloids and argued that the interior of the OM colloids may be considered nano- to micrometer-sized anoxic environments within a surficial (oxic) environment. Furthermore, they proposed the recycling of Cu in the surficial environment, which involves the dissolution of the Cu-bearing phases during OM decomposition; the partial oxidation of the reduced Cu- and S-bearing species, the diffusion of Cu and S-bearing phases into the OM matrix, the reduction of oxidized species and the neoformation of CuS_x phases in OM. However, there is still a lack of knowledge on the formation mechanisms of the CuS_x phases and the role of other inorganic phases within and outside OM colloids. Hence, this study will investigate systematically the association of CuS_x phases with other inorganic phases within OM colloids using scanning- and high resolution-transmission electron microscopy (STEM and HRTEM) Furthermore, it will use the TEM observations to develop a model for the formation mechanisms of CuS_x phases in nanopores of OM colloids.

2.1.1. Cu-emissions by smelters and coal-power plants

The study area is a typical smelter impacted area that extends around the city limits of Rouyn-Noranda, Quebec, Canada and surrounds the Horne smelter. The ore processed at the Horne smelter included sphalerite, pyrite, galena, pyrrhotite, chalcopyrite and magnetite, as well as native silver and gold (Kerr & Gibson, 1993) with pyrite, pyrrhotite, chalcopyrite and magnetite comprising up to 85% of the mass (Denis, 1933). In the period of 1927 to 1976, the smelter has released PM containing Ni, Pb, Zn, Cu and Cd with a peak value of more than 1.5 million metric tons in 1965. The implementation of pollution controls in 1970 greatly reduced the annual emission of PM (Kettles & Bonham-Carter, 2002). After 1976, the smelter processed predominantly electronic waste containing precious metal(loid)s such as Cu. The smelter contaminated soils in Rouyn Noranda are comparable to their counterparts in Timmins (Mantha et al., 2019) (Canada), Sudbury (Lanteigne et al., 2014) (Canada), Flin Flon (Henderson et al., 1998) (Canada), Anaconda (Burt et al., 2003) (USA), Prescot (Clemente et al., 2008) (UK), Harjavalta (Derome & Lindross, 1998) (Finland), Lommel (Nachtegaal et al., 2005) (Belgium), Krompachy (Bigalke et al., 2010) (Slovakia), Veles (Stafilov et al., 2010) (Macedonia), Kitwe (Kříbek et al., 2010) (Zambia), Port Kembla (Martley et al., 2004) (Australia) and Hubei (Cai et al., 2019) (China) in terms of Cu concentrations but they may contain different types and amounts of emitted particulate matter (PM) as those are controlled by the processed ore and smelting methods employed.

Coal-power plants also emit Cu as Cu-sulfides can occur in elevated concentrations in coal (Sullivan et al., 2005). Although the concentrations of Cu in the combusted coal are much lower relative to those in Cu-bearing ores, recent studies showed that Cu emissions by coal-power plants across the world have a large impact on their surrounding environments and human health (Mandal & Sengupta, 2006; Huang et al., 2017; Li et al., 2017; Burachevskaya et al., 2019; Turhan et al., 2020).

2.1.2. The environmental fate of PM in soils impacted by smelter emissions

Soils surrounded by mining sites often contain the contamination footprint of mining activities in the form of metal(loid)-bearing PM. The deposition of this PM results in elevated concentration levels of metal(loid)s in soil (Schindler & Hochella, 2017). After deposition, the PM generally resides in the soil's surficial layers. Weathering of PM is not only initiated and controlled by pore water volume, soil matrix conditions, and environmental conditions such as precipitation

rates and temperature but also depends on the mineralogical and chemical composition of PM (Ettler, 2016). Weathering of the PM results in the release of metal(loid)s which are often sequestered and mobilized by the colloidal soil fraction.

The environmental fate of PM in smelter-impacted soils is commonly assessed through the concentrations of released metal(loid)s, their bioavailability and spatial distribution around the source (Adamo et al., 1996; Ettler et al., 2004; Knight & Henderson, 2006; Lanteigne et al., 2012; Lanteigne et al., 2014; Qasim et al., 2015). However, the results of these studies can be sometimes misleading when it comes to the mobility and bioavailability of metal(loid)s in soils. For example, the distributions of Cu and Ni with depth in soils around the smelter complexes in Sudbury suggest higher mobility of Cu than Ni, although the former element has a higher affinity to sorb to Fe-oxides and OM (Schindler et al., 2016). Lanteigne et al. (2012) and (Schindler et al., 2016) showed that this apparent higher mobility of Cu than Ni is due to the higher solubility of Cu- versus Ni-bearing spinel phases in PM. Hence, mineralogical information about metalloid-bearing hosts is of great importance for our understanding of the mobility, transport and sequestration of metal(loid)s within contaminated soils.

2.1.3. The ecological impact of Cu emitted by smelters

The environmental impact of the smelting activities in Rouyn Noranda has been addressed in numerous geochemical, mineralogical and biological studies focused on the concentrations and speciation of metal(loid)s in soils, lakes, rock coatings, snow samples and biota (Bonham-Carter et al., 2006; Knight & Henderson, 2006; Telmer et al., 2006; Zdanowicz et al., 2006; Masson et al., 2010; Caplette et al., 2015; Dinis et al., 2020). Studies on the ecological impact of Cu emissions were studied for example by Skalny et al. (2018) who showed that children from residential areas near a Cu smelter have elevated levels of Cu in their biosamples. Furthermore, Liu et al. (2021) showed that 15-75% of the total Cu, Cd and Pb concentrations in vegetables grown in smelter-impacted soils originated from the Cu smelter emissions. Additionally, Gashkina et al. (2015) showed that Cu and other metal(loid)s accumulated in organs and tissues of fish in contaminated lakes around a large Cu smelter in Karabash, Russia.

Elevated Cu concentrations in soil and water bodies can be toxic to humans, animals, plants and micro-organism (Alloway, 2012). Cu is needed for normal growth and functioning of the human body but can be toxic above a certain threshold (10 mg/day) and can lead to various diseases

such as Wilson disease and other free radical-induced oxidative damages (Hayashi et al., 2000; Sayre et al., 2000; Liang & Dedon, 2001; Letelier et al., 2010; de Romaña et al., 2011; Gaetke et al., 2014). Phytotoxic effects on plants are also common in soils with excess of Cu, which retards their growth and cause leaf chlorosis (Sheldon & Menzies, 2005; Kopittke & Menzies, 2006). Furthermore, aquatic biota are more sensitive to Cu toxicity compared to terrestrial organisms as their toxicological tolerance limit is 10 to 1000 fold lower than in mammals (Hodson et al., 1979). For example, Cu toxicity in fish species results in alteration of their growth and reproductive system, whereas substantial reduction in algal biomass and shift in algal communities is observed with increased Cu concentrations in freshwater lakes (Guasch et al., 2002; Driessnack et al., 2017; Morin et al., 2017; Cao et al., 2019).

2.1.4. Studying mineralogical processes in soils at the nano- and micrometer scale

The electron beam techniques such as transmission electron microscopy (TEM) and scanning electron microscopy (SEM) can be used to explore mineralogical details about metal(loid)-bearing phases in soils. For example, Knight & Henderson (2006), Mantha et al. (2012), Ettler et al. (2014) and Caplette & Schindler (2018) conducted SEM and TEM studies on metal(loid)-bearing PM in soils and rock coatings around smelters in Trail, British Columbia, Rouyn Noranda, Quebec and Sudbury, Ontario and Zambian copperbelt. Similarly, SEM and TEM studies were conducted on the occurrence of metal(loids) in secondary phases within contaminated soils by Buatier et al. (2001), Schindler & Hochella (2017), Schindler & Hochella (2017) and Schindler et al. (2021).

Soil processes and properties at the nanometer scale such as weathering and cohesion affect processes at the kilometer scale such as the formation of landscapes and flooding. Examinations at the nanoscale also help explain the mobility of elements in soils as their sequestration and adsorption in heterogeneous mineral assemblages cannot be resolved in bulk studies or studies at the micrometer scale (Schindler & Hochella Jr, 2016; Schindler & Hochella, 2017; Mantha et al., 2019). For example, the occurrence of metallic Cu and covellite phases in nanopores of OM particles and colloids Mantha et al. (2019) partially explains the observed high affinity of Cu towards OM in Cu-contaminated soils, an observation that would have been impossible to make at the micrometer-scale with SEM. The disadvantage of nano-scale examination is that observed features at this scale are not always representative features for a larger scale geological unit such

as a soil layer in a specific area. Hence, this study does not intend to depict a representative mineralogy of the colloidal fraction in the contaminated surficial soils of Rouyn Noranda. It rather tries to decipher underlying mechanisms for the sequestration of Cu in organic-rich contaminated oxic soils.

2.1.5. Objectives

Given the uncertainty on the role of colloidal OM in the sequestration of Cu, and the limited knowledge on the formation and stability of CuS_x phases in the surficial oxic environment, the objectives of this study are to examine the role of colloidal OM in the sequestration and transport of Cu in the oxic organic-rich soils around the Horne smelter in Rouyn Noranda. It specifically examines whether

(a) The sequestration of the metal(loid)s occurs via the formation of nanoparticles in the nanopores of OM colloids;
(b) The retention of Cu by OM is also controlled by the occurrence of other phases present in OM such as Fe-(hydr)oxides, amorphous silica and $CaCO_3$ phases;
(c) The colloidal transport of metal(loid)s contributes to their cycling in surficial soils;

Furthermore, we review factors that influence the movement and nucleation of metal(loid)-bearing species within nano-porous media.

In this study, *nanopore* is defined here as a pore with a diameter below 100 nm (McNaught & Wilkinson, 1997) and the term *organic matter (OM)* is used for HS that are mainly formed during the decomposition of organic material. The fraction deposited during centrifugation is represented by the term *colloidal fraction*, the term *dissolved organic matter* (DOM) is used to describe carbon-based aqueous species, the term *nanoparticle* represents particles that have a diameter below 100 nm and particles in solution with diameters in the range of 100 to 1000 nm are termed *colloids*.

2.2. Methodology

Knight & Henderson (2006) characterized the regional distribution of metal(loid)s around the Horne smelter. On the basis of their study, we sampled twenty-one surficial soil samples (upper 5 cm) at seven different sites within a two-km radius of the Horne smelter in Rouyn-Noranda in the late summer of 2017 (Figure 1). Two to three samples were taken from each site (A-C) (Figures

2-2a and 2-2c). On the basis of their distance from the smelter and the Cu- and Zn-concentrations, the samples 5A, 7A-B were selected for further characterization (Tables 2-S1 and 2-S2). Site 5

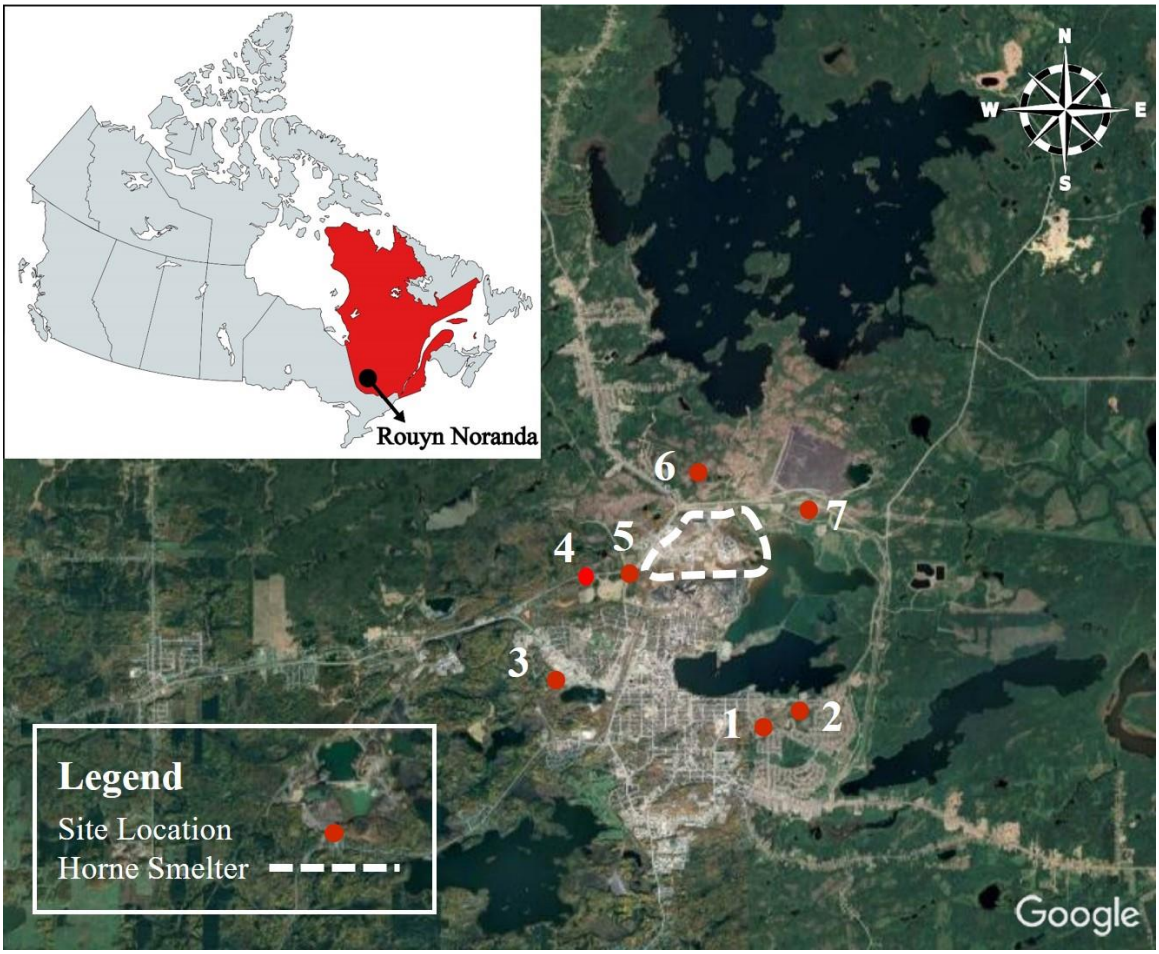

Figure 2-1: Map of study area surrounding the Horne smelter (white dashed lines) with red dots representing the locations of the seven sampling sites. The inserted image indicates the location of Rouyn Noranda within Quebec, Canada.

was located west of the smelter in a forest; the sampled material was a humus-rich surficial soil (Figures 2-1 and 2-2a). Site 7 was located north-east of the Horne smelter and the soils were collected from Ahgy soil layers (Figures 2-1, 2-2b, 2-2c and 2-S1). None of the surficial soil samples were collected in proximity to surficial waters (at least 50 m from the nearest lake shoreline, river bank or wetland) and thus were most likely only water-saturated during the spring thaw. The chemical and mineralogical compositions of the soil samples were characterized with

ICP-MS for Ag, Co, Cu, Pb, Sb, Sn and Zn, C-N-S analyzer for C, N and S (Tables 2-S1, 2-S2, 2S-3, 2-S4 and 2S5) and X-ray powder diffraction for mineral phases, respectively (Figure 2-S2).

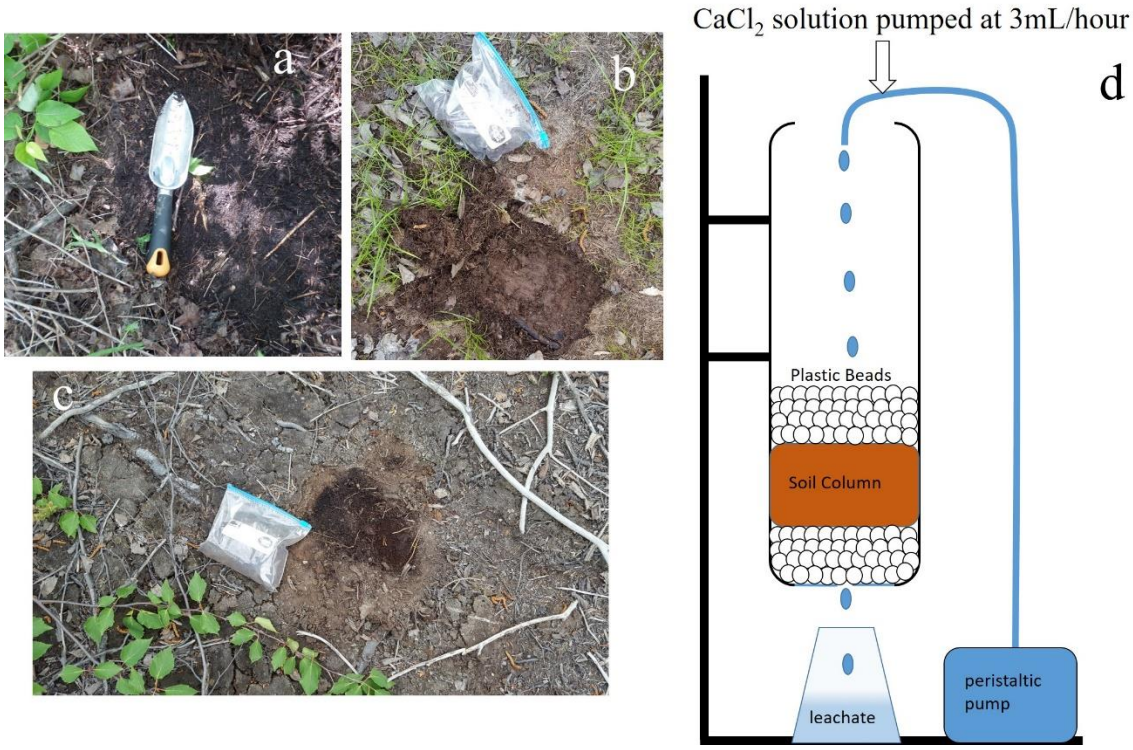

Figure 2-2: Photographs of the organic-rich soils sampled at the locations (a) 5A, (b) 7A and (c) 7B; (d) schematic sketch showing the leaching experiment setup.

The soil leachates were collected through column leaching experiments from the soil samples 7A, 7B and 5A (Figure 2-2d). The colloidal fraction was then extracted from leachates using ultra-centrifugation and filtration process, and then further characterized with TEM. ICP-MS analysis was performed on the leachate fraction after acidification (to determine the total concentrations of the metal(loid)s) and a centrifuged/filtered (0.1 μm) leachate (to determine the concentrations of the metal(loid)s in solution). The size distribution of the colloids was determined with a dynamic light scattering method and the TEM analysis was conducted with a field emission TEM FEI Talos F200x at the Manitoba Institute of Materials. Technical details for each type of analysis is provided in the materials and methods section in the Appendix A (Supplementary information).

2.2.1. Identification of metal(loid) bearing phases with TEM and STEM.

The metal(loid)-bearing phases in the colloids were identified based on a combination of *d*-spacings observed in selected area diffraction (SAED) pattern and high-resolution TEM (HRTEM) images (in combination with FFT pattern) and semi-quantitative chemical analyses determined with energy dispersive spectroscopy (EDS) analyses in Scanning TEM mode. An example for the identification of a covellite precipitate using chemical analyses and SAED pattern are provided in Figure 2-S3. In the absence of any structural information (no diffraction spots in SAED pattern or lattice fringes in HRTEM images), phases within OM colloids are named based on their chemical composition (e.g. Cu-Fe-sulfide or Al-silicate).

2.2.2. Characterization of textural features with STEM

In STEM mode, transmitted beam electrons that have been scattered through a large angle are detected using a high angle annular dark field (HAADF) detector and are used to generate three-dimensional images that provide information on textural features such as surface topography and porosity. These images help to distinguish for example surface precipitations (Figure 2-3e) from the occurrence of mineralogical phases within a colloid (Figure 2-3g) or can be used to resolve the porosity of organic colloids (Figures 2-3a, 2-3b, 2-3c, 2-3d and S4).

2.3. Results

2.3.1. Bulk Soil Chemistry and Mineralogy

Only samples used in the leaching experiments are described here in detail. Sample 5A is a black, organic, fibric and mineral-rich layer with litter on top, its color code 10YR [2/1] (dry) and its pH 4.74 (Figure 2-2a). Sample 7A is composed of a brown thin litter of fibric mineral layer over a light reddish-brown organic layer. Its color code 7.5YR [4/2] (dry) and has a pH of 4.39 (Figure 2-2b). Sample 7B mostly represents black humus, has color code 5YR [2.5/1] (dry) and pH of 3.84 (Figure 2-2c). All these samples contain Cu, Zn and Pb concentrations above the average of all collected samples (Table 2-S2).

The samples contain high amounts of OM (total C $\geq$ 22%, Table 2-S1) and are primarily mineralogically composed of quartz (SiO_2), albite ($NaAlSi_3O_8$) with traces of magnesioferrite ($MgFe_2O_4$), protoenstatite ($Mg_2Si_2O_6$), magnetite (Fe_3O_4) and clinochlore $Mg_5Al(AlSi_3O_{10})(OH)_8$ (Figure 2-S2).

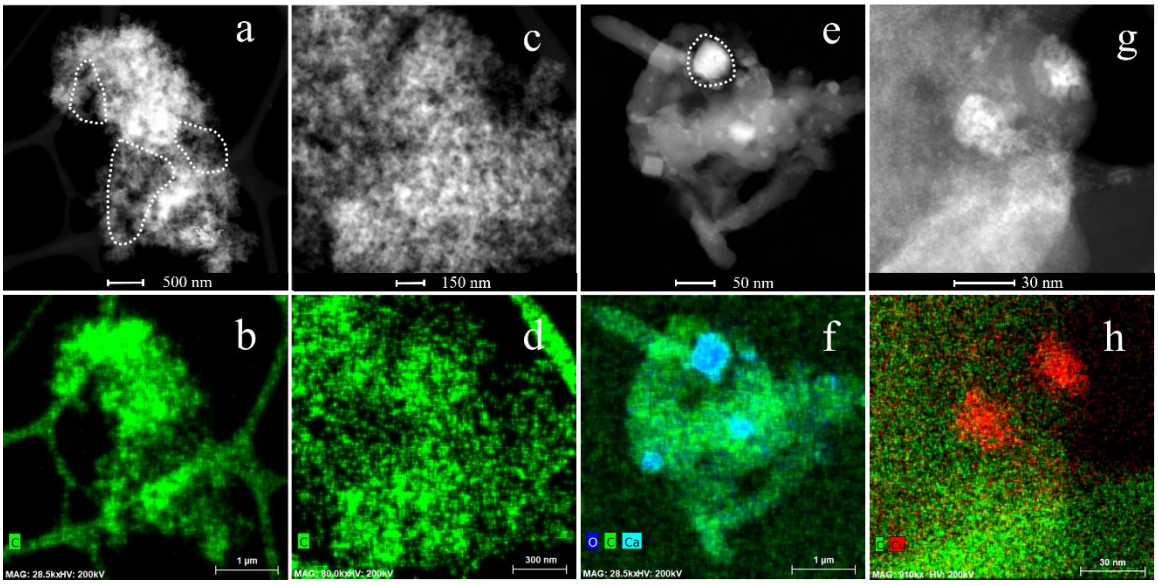

Figure 2-3: Morphology of organic colloids: (a and c) STEM images and (b and d) STEM-EDS chemical distribution maps for C (green); (a) Large pores or porous zones are visible within organic colloids (highlighted with white dashed lines). (c) STEM image and (d) STEM-EDS chemical distribution maps for C (green); Nanopores are visible within organic colloid. (e) STEM image and (f) STEM-EDS chemical distribution map for O (blue), C (green) and Ca (turquoise); Calcium carbonate precipitate on the surface of organic colloid indicated by high relief (white dashed lines in (e). (g) STEM image and (h) STEM-EDS chemical distribution map for C (green) and Cu (red); Cu-sulfide precipitates embedded within organic colloid as indicated by no surface relief in (g).

2.3.2. Size and Morphology of the Colloidal Material

The colloids have an average size of 500 nm (TEM data) with particle size being normally distributed between 200 and 1000 nm (Figure 2-S5). Many organic colloids are highly porous (Figures 2-3 and 2-S4). Areas of high porosity commonly occur in close proximity to the exterior surfaces of the colloids but can also extent toward their interior, especially along cracks (Figures 2-3 and 2-S4). Nanopores are more abundant than microspores (indicated with dashed lines in Figures 2-3c and 2-S4), which themselves are composed of nanopores.

Surface precipitates on organic colloids can be recognized on their high relief in STEM images, whereas metal(loid)-bearing phases embedded within colloids show low reliefs in STEM

images. For example, the occurrence of a calcium carbonate (highlighted with white dashed line) on the surface of an organic colloid can be easily recognized on its relief in the STEM image (Figures 2-3e and 2-3f), whereas precipitates of covellite mineral grain embedded within a colloid has in comparison a much lower relief in a STEM image (Figures 2-3g and 2-3h).

2.3.3. Mineralogy and Chemistry of the Colloidal Material

The majority of colloids host metal(loid) bearing phases in their nanopores or on their surfaces, which are predominantly composed of Cu-sulfides, Cu-Sn-sulfides, Fe-(hydr)oxides and Fe-Cr-sulfates.

2.3.3.1. Cu and Fe sulfide phases within OM

Copper sulfides nanoparticles (CuS_x with x = 0.5-2) are common constituents in OM colloids and are not identified in inorganic-based colloids, composed of e.g. Fe-(hydr)oxides or calcium carbonates. CuS_x phases such as covellite (CuS), villamaninite (CuS_2) and anilite (Cu_7S_4) were identified on the basis of their composition, SAED pattern and lattice fringes visible in high-resolution TEM images (Figures 2-4, 2-5, 2-6, 2-7 and 2-8). STEM images indicate that CuS_x phases are embedded in the matrix of OM colloids (Figures 2-4, 2-5, 2-6, 2-7 and 2-8). Hence, lattice fringes of their precipitates are only visible in small nanosize domains where the thickness of the OM does not exceed circa 100 nm (indicated with dashed lines in the Figures 2-4, 2-5, 2-6, 2-7, 2-8 and 2-9). The STEM images also indicate that these CuS_x precipitates have various morphologies, porous surfaces and diffuse particle boundaries (Figures 2-4, 2-5, 2-6 and 2-7). For example, a cluster of CuS_x nanoparticles occurs between CuS_x-rich layers, in which the mineral villamaninite (CuS_2) is sandwiched between two covellite nanoparticles with lattice fringes in the same orientation (Figure 2-4). Here, CuS_x-rich layers are parallel to each other and parallel to OM depleted in CuS_x phases (Figure 2-4). In general, OM colloids can contain multiple (Figure 2-4) or individual CuS_x-rich layers (Figure 2-5). In some cases, the layers are branched (Figures 2-5a, 2-5b and 2-5c) or show uneven surfaces (Figures 2-5d, 2-5e and 2-5f).

CuS_x phases also occur along the rims of OM colloids (Figures 2-6, 2-7 and 2-8), where they can be in association with amorphous silica inclusions (Figures 2-7 and 2-8). For example, the CuS_x phases (covellite (CuS) and anilite (Cu_7S_4,)) occur within a circa 10 nm wide area along the rim of an OM colloid (Figure 2-6). Heterogeneous nucleation and growth of covellite and kuramite (Cu_3SnS_4) occurred on silica inclusions within OM colloids where nano-crystallites with diameters of 20-40 nm sandwich larger amorphous silica inclusions (Figures 2-7 and 2-8).

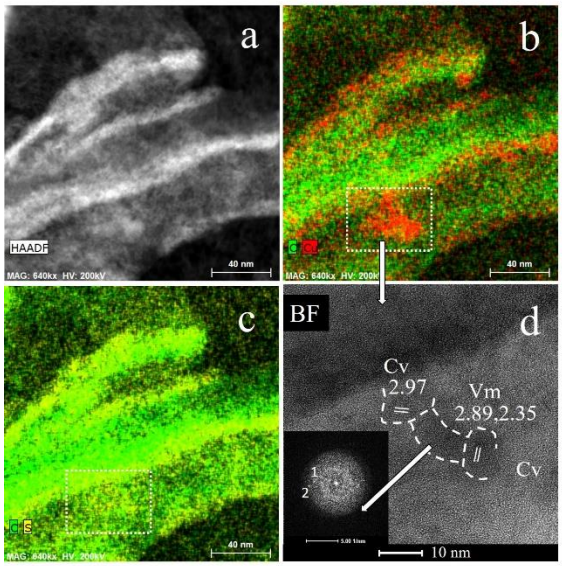

Figure 2-4: CuS_x rich layers of colloidal OM: (a) STEM image and (b)-(c) STEM-EDS chemical distribution maps for (b) C (green) and Cu (red) and (c) C (green) and S (yellow); the area shown in (d) is indicated with a white rectangle in (b) and (c); (d) high-resolution TEM image of a CuS_x cluster composed of covellite (Cv) and villamaninite (Vm), characteristic *d*-spacing of 2.97Å for Cv is highlighted with white lines and *d*-spacings of 2.89 Å and 2.35 Å for Vm are labelled "1" and "2" in the FFT pattern shown in the lower-left corner.

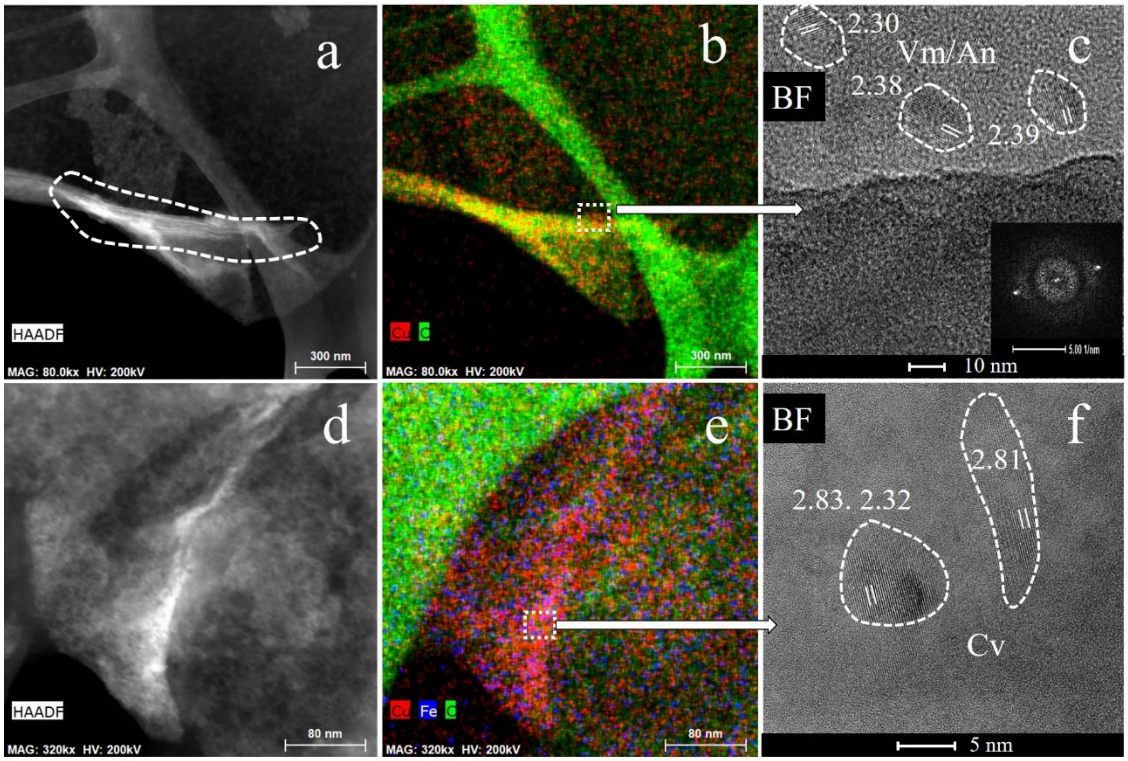

Figure 2-5: CuS_x rich branched layers of OM: (a)-(f): (a) STEM image, (b) STEM-EDS chemical distribution map for Cu (red) and C (green) and (c) high-resolution TEM image of villamaninite/anilite (Vm/An) within organic colloid; lattice fringes are visible in domains (dashed lines) and their d-spacings of 2.30 Å and 2.38/2.39 Å are highlighted with white lines; (d) STEM image and (e) STEM-EDS chemical distribution maps for Cu (red), C (green) and Fe (blue) and (f) high-resolution TEM image of covellite (Cv), lattice fringes with d-spacings of 2.83/2.81 Å and 2.32 Å are highlighted with white lines in domains composed of Cv; note that that the intensity for C (green) in the chemical distribution in (e) is affected by the thickness of the sample.

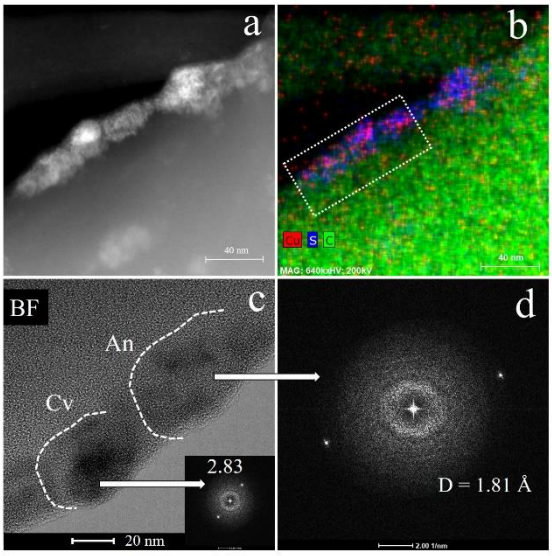

Figure 2-6: CuS_x phases along the rim of organic colloids: (a) STEM image, (b) STEM-EDS chemical distribution map of Cu (red), C (green) and S (blue) and (c) high-resolution TEM image; *d*-spacings of lattice fringes of 2.83 Å and 1.81 Å in domains of Cv and An (white dashed line in (c)) are indicated in FFT pattern in (c) and (d), respectively.

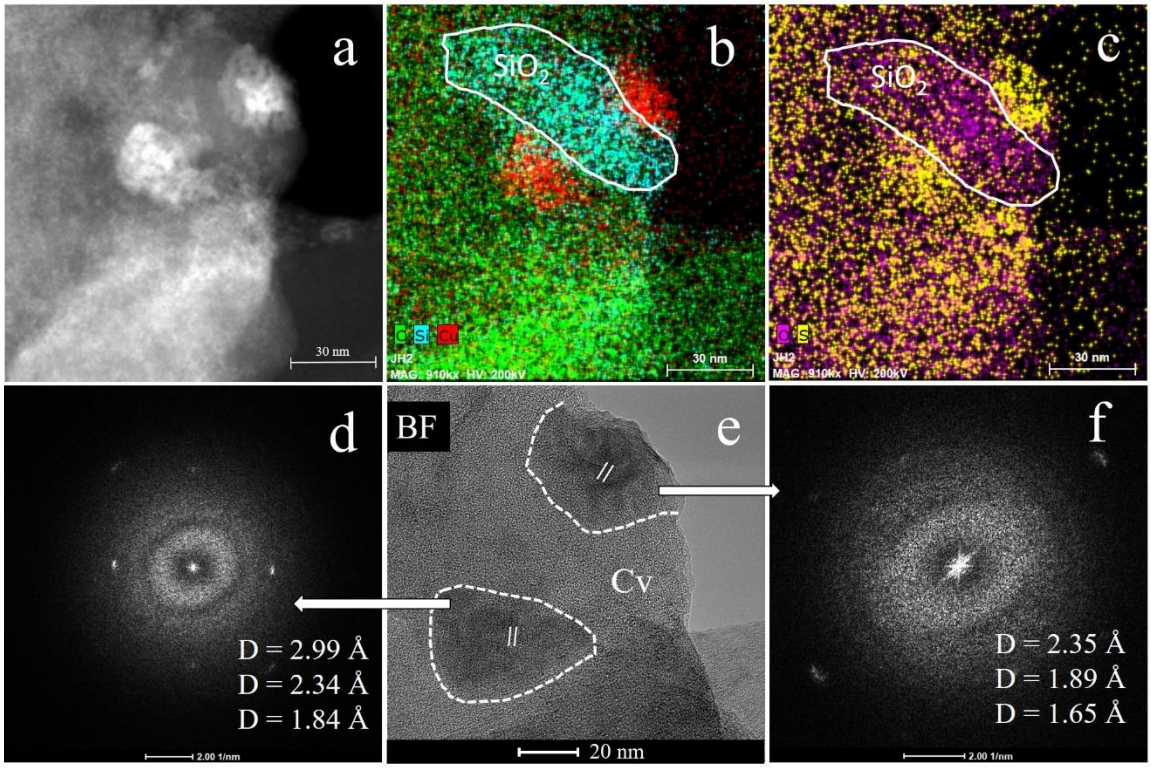

Figure 2-7: Covellite (Cv) nanoparticles on the surface of an amorphous silica inclusion: (a) STEM image, (b)-(c) STEM-EDS chemical distribution map for (b) Cu (red), C (green) and Si (light blue) and (c) S (yellow) and O (violet), (d)-(f) High-resolution TEM images with corresponding FFT pattern; (e) lattice fringes in the Cv nanoparticles (dashed white lines) are highlighted with solid white lines and corresponding *d*-spacings are shown in the FFT pattern in (d) and (f).

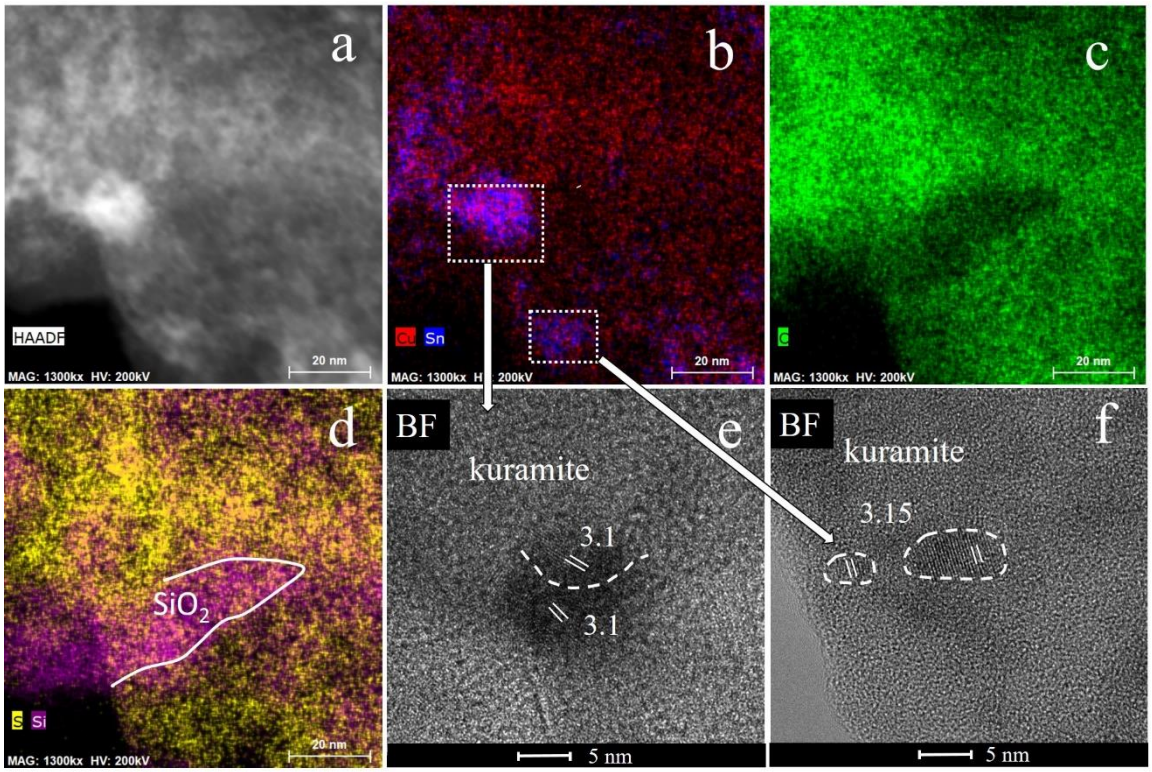

Figure 2-8: Kuramite, Cu_3SnS_4 nanoparticles grown on the surface of amorphous silica within an organic colloid: (a) STEM image, (b)-(d) STEM-EDS chemical distribution map for (b) Cu (red) and Sn (blue) and (c) C (green) and (d) S (yellow) and Si (violet), (e)-(f) high-resolution TEM images indicating lattice fringes (highlighted with solid-white lines) in nano-domains (white dashed); the *d*-spacing of ~3.1-3.15 Å match the strongest X-ray diffraction peak (100) reported for kuramite.

2.3.3.2. Cu-bearing Fe-(hydr)oxide and –sulfates within and outside of OM

Fe-(hydr)oxides can form fragmented aggregates within porous OM colloids (Figure 2-9). Partial coverage of the aggregates by OM (Figures 2-9a and 2-9e) indicates that the Fe-(hydr)oxides are embedded within the OM rather than being part of a surface precipitate. These aggregates and the surrounded organic matrix contain higher concentrations of Cu (~12 wt%) (Figure 2-9b) than the corresponding bulk soil from site 7A with 0.27 wt% Cu (Table 2-S1). In the Fe-(hydr)oxide aggregates occur domains with visible lattice fringes and with diameters of circa 10 to 60 nm. The *d*-spacings of the lattice fringes suggest the occurrence of ferrihydrite and hematite, whereby the *d*-spacings of 4.0 Å and 3.6 Å (not observed for ferrihydrite) indicate the

exclusive occurrence of hematite (Figures 2-9d and 2-9h). For example, domains of most likely ferrihydrite and hematite form an aggregate with an outline depicting rhombohedral symmetry (Figure 2-9d). The heterogeneous distribution of Cu, as well as Si within and around this aggregate, indicates that these elements did not accumulate on the organic-based surface of the colloid during sample preparation as in such case a more homogeneous distribution of Cu and Si would be expected (Figures 2-9b and 2-9f). Similarly, a complex assemblage of Fe-Cr-sulfates, $(Fe_{0.5}Cr_{1.5})(SO_4)_3$ - $(Fe_{1.0}Cr_{1.0})(SO_4)_3$ and ferrihydrite/hematite domains occur in an OM colloid, which has a higher Cu concentration (~ 8 wt% Cu) relative to the corresponding bulk soil at site 7B with 0.38 wt% (Figures 2-9e, 2-9f, 2-9g, 2-9h and Table 2-S1). The Fe-Cr-sulfates are heterogeneous in composition and size with Fe:Cr ratios between 1:2 and 1:1 (solid solution between mikasaite, $Fe_2(SO_4)_3$ and $Cr_2(SO_4)_3$) and with particle sizes ranging from >70 nm to 10-15 nm (Figure 2-S6). These anhydrous Fe-Cr-sulfates commonly form above room T in volcanic fumaroles (Balić-Žunić et al., 2016), whereas hydrous phases such as melanterite $FeSO_4 \cdot 7H_2O$ and rozenite, $FeSO_4 \cdot 4H_2O$ are typical evaporation products of Fe^{3+}-sulfate bearing solutions (Xu & Parise, 2012).

Copper-bearing Fe-(hydr)oxides also occur outside of OM colloids. For example, hematite nanoparticles with well-defined edges, and without any visible porosity or fragmentation occur in the colloidal fraction (Figure 2-10). These can include almost euhedral Cr-rich hematite nanoparticles (part of the Fe_2O_3-Cr_2O_3 solid solution) (Figures 2-10a, 2-10b, 2-10c, 2-10d and S7) and hematite nanoparticles with elevated concentration of Cu (8-9 wt%) (Figure 10d-f). In general, colloids composed solely of Fe-(hydr)oxides, are enriched in Cu (8-9 wt%) relative to their corresponding bulk soils (Table 2-S1).

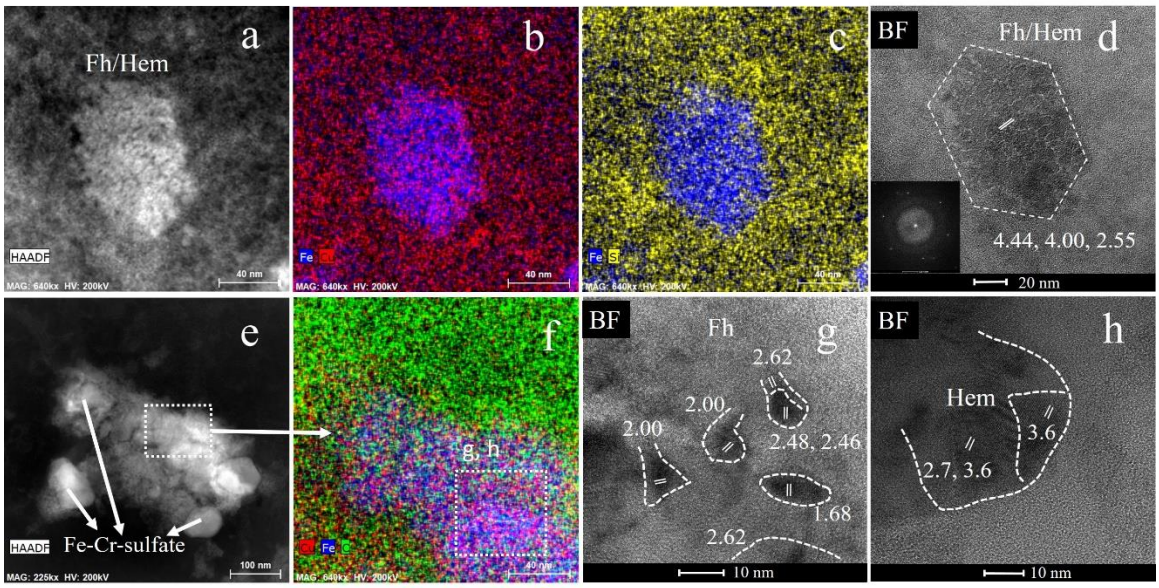

Figure 2-9: (a)-(h) Assemblages of ferrihydrite (Fh) and hematite (Hem) within organic colloids containing on average 10 wt% Cu; (a)-(d) fragmented assemblage of Fh and Hem nanodomains: (a) STEM image, (b)-(c) STEM-EDS chemical distribution maps for (b) Fe (blue) and Cu (red) and (c) Fe (blue) and Si (yellow) and (d) high-resolution TEM image of an aggregate indicating lattice fringes (highlighted in solid white line) within a fragmented assemblage of Fh and Hem nanodomains; (e)-(h) ferrihydrite (Fh) and hematite (Hem) nanodomains in association with $(Fe_{0.5}Cr_{1.5})(SO_4)_3$-$(Fe_{1.0}Cr_{1.0})(SO_4)_3$ within an organic colloid (e) STEM image, (f) STEM-EDS chemical distribution map for Cu (red) Fe (blue) and C (green), (g)-(h) high-resolution TEM images indicating characterizing lattice fringes (highlighted with solid white lines) within nanodomains of Fh and Hem; all *d*-spacings are given in Å.

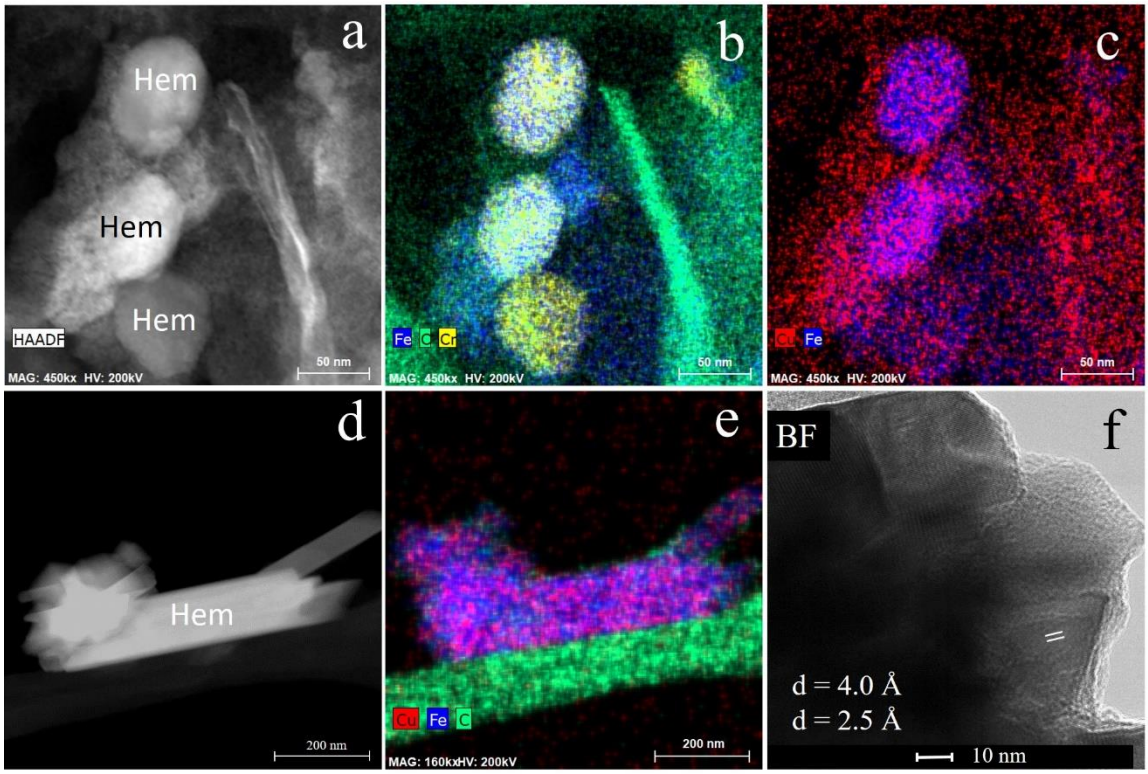

Figure 2-10: (a)-(c) Almost euhedral Cr-bearing hematite (Hem) nanoparticles containing clusters of Cu around edges (9 wt% Cu): (a) STEM image, (b)-(c) STEM-EDS chemical distribution maps for (b) Fe (blue), Cr (yellow) and C (green) and (c) Cu (red) and Fe (blue); (d)-(f) euhedral hematite (Hem) crystal in the colloidal fraction containing 8 wt% Cu: (d) STEM image, (e) STEM-EDS chemical distribution map for Cu (red), Fe (blue) and C (green) and (f) high-resolution TEM image indicating characteristic lattice fringes for Hem (highlighted with solid white lines).

2.3.3.3. Cu-bearing carbonates and phosphates in OM colloids

OM colloids derived (most likely) from former bacterium cells (indicated by presence of distinct round nuclei of phosphorus and magnesium (Figure 2-S8), which are characteristic of bacterium cells) also occur in the leachates (Figure 2-11). One of these colloids contains (unidentified) calcium carbonate phases (Figure 2-11a and 2-11b), Cu-bearing nanoparticles and Ca-Mg-phosphate (Figure 2-11 and 2-S8). The occurrence of the Cu-bearing nanoparticles in the organic matrix coincides here with those of the carbonates and phosphates (compare Figures 2-

11c and 2-11d). The $CaCO_3$ particles occur as euhedral crystals of rhombohedral symmetry (most likely calcite), suggesting that they are formed during biogenic crystallization processes (Dupraz et al., 2009; Perito & Mastromei, 2011). Their relatively high porosity (Figure 2-10e) indicates that they were altered at a later stage, perhaps through the interaction with Cu-bearing pore solutions.

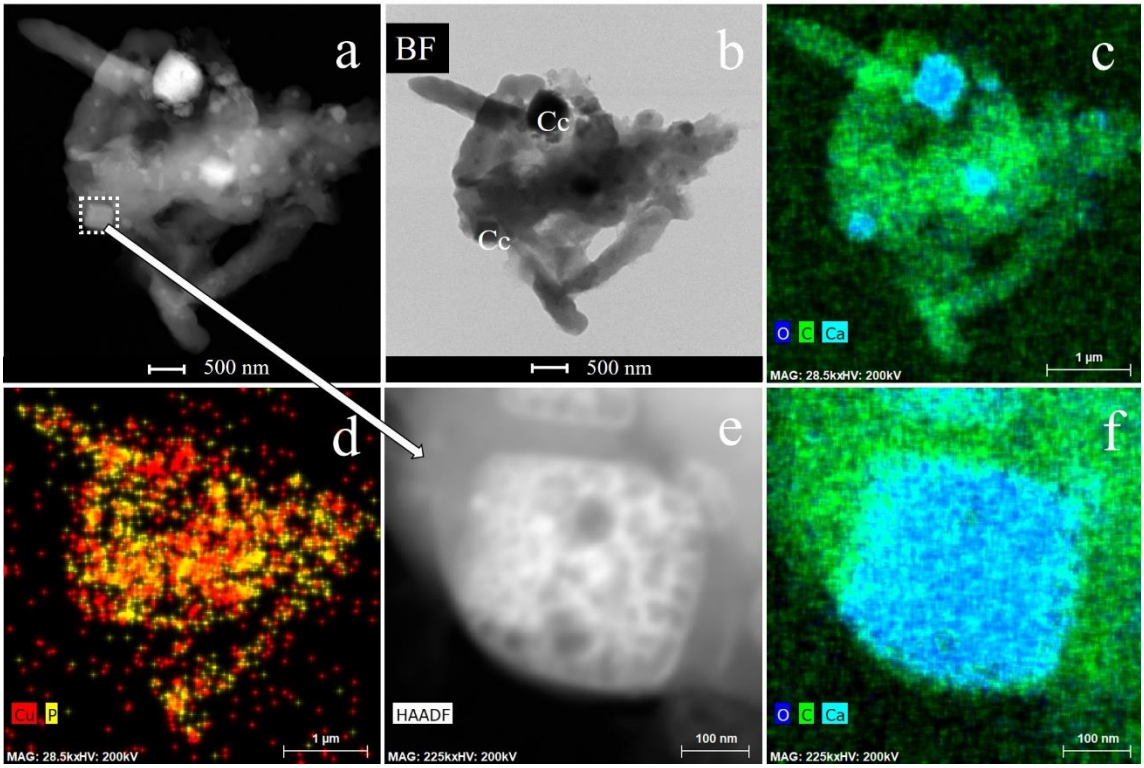

Figure 2-11: Calcium carbonate mineralized (Cc) colloidal phases in a porous matrix of an organic colloid containing on average 4 wt% Cu: (a) STEM image, (b) TEM image, (c)-(d) STEM-EDS chemical distribution map for (c) O (blue), C (green) and Ca (light blue) and (d) Cu (red) and P (yellow); an euhedral calcium carbonate crystal shown in (e) is indicated with a white square in (a); (e) STEM image of the euhedral crystal indicated in (a) and (f) corresponding STEM-EDS chemical distribution map for O (blue), C (green) and Ca (light blue).

2.3.4. Proportion of metal(loid)s in the colloidal versus solute fraction of the leachate

Chemical analysis of the leachates indicates that the Cu-Fe-sulfides bearing colloids have a considerable impact on the colloidal transport of Cu as the proportion of Cu in the colloidal

fraction of the leachates ranges from 20 to 40% with respect to the total concentration of Cu (Tables 2-S4 and 2-S5, Figure 2-S9). The total concentrations of Cu in the leachates range from 8000 to 20000 µg L^{-1} (Table 2-S4). Similarly, the proportions of other base metals such as Cd, Fe, Mn and Zn in the colloidal fraction of the leachate are also in the 20 to 40% range (Table 2-S4, Figure 2-S9), although their total concentrations in the leachate are much lower relative to those of Cu (Table 2-S4).

2.4. Discussion

The atmospheric deposition of metal(loid)-bearing PM emitted from a smelter or windblown from mine-waste piles severely deteriorates the quality of water and soil systems and also has negative repercussions for human health (Freedman & Hutchinson, 1980; Adamo et al., 1996; Leverington & Schindler, 2018). At Rouyn Noranda smelter emissions are considered the primary source of metal(loid)-bearing contaminants in surficial soils based on the general trend of decreasing metal(loid) contamination in surficial soils with increasing distance from the smelter and their corresponding distribution patterns (Knight & Henderson, 2006) (Table 2-S1). The observations above indicate that metal(loid)s released and deposited by smelter emissions are an intrinsic part of the colloidal fraction in organic-rich soils of Rouyn Noranda. The mineralogy in the colloidal fraction is characterized predominantly by the occurrence of Fe-(hydr)oxides (Figure 2-9 and 2-10) and CuS_x phases (Figures 2-4, 2-5, 2-6, 2-7 and 2-8). We will first discuss these two groups of minerals before addressing the formation of phases within nanopores of OM.

2.4.1. CuS_x phases

The chalcophile character of Cu has led to a large variety of CuS_x minerals with chalcopyrite ($CuFeS_2$) being the most abundant (Amcoff & Holényi, 1992). The thermodynamic stability of a CuS_x mineral is controlled by the total concentration of S and the type of sulfur species. For example, experimental studies indicate a shift in stability of CuS_x phase with increasing sulfur concentration: at low sulfur concentration, sulfur deficient phases such as chalcocite (Cu_2S) form followed by numerous intermediate phases and the sulfur-rich phases covellite and villamaninite at high sulfur concentration (Amcoff & Holényi, 1992). Hoffmann et al. (2020) showed that the stability of CuS_x nanoparticles under anoxic and oxic conditions decreases in the presence of FA as these acids (a) hinder the growth of CuS_x nanoparticles, (b) prevent their aggregation and (c) plays an active role in their oxidative dissolution.

Covellite is the major Cu phase in OM colloids (Figures 2-4, 2-5, 2-6 and 2-7) and its occurrence is in accord with the observations of Mantha et al. (2019) and others on the occurrence of sulfides in surficial organic-rich soils (Zdanowicz et al., 2006; Lanteigne et al., 2012). Mantha et al. (2019) argued that the formation of covellite nanoparticles in the OM colloids could not be attributed to the breakdown of larger micrometer-sized covellite particles as the mineral was not identified outside the OM in the surficial soils around the Kidd Creek smelter. Similarly, this study showed that covellite precipitates are always embedded in OM colloids of the surficial soils around the Horne smelter.

The occurrence of CuS_x phases in the surficial soils at Rouyn Noranda and Kidd Creek indicates high concentration of sulfide species (HS^-/S^{2-}) in nanopores of OM. Furthermore, the occurrence of different CuS_x phases in close proximity to each other (at the nanoscale; Figures 2-4, 2-5 and 2-6) suggests that disequilibria occurred between nanopores and between these pores and the oxidizing conditions of the surrounding bulk soil. The reason for these disequilibria may be related to unique conditions in nanopores, identified in numerous experimental studies (Wang, 2014). For example, Schindler & Singer (2017) indicated that mineralogical phases comprising of both As(III) and As(V) species occur in close proximity to each other in pore spaces of mineral surface coatings and argued that limited flow potentials created confined environments which most likely promoted the formation of various As phases. Some of these conditions and how these affect nucleation and stability phases will be addressed later.

2.4.2. Fe-(hydr)oxides

The weathering of bedrocks contributes primarily to the Fe-budget of soils, although PM added a considerable amount of Fe to the surficial soils in Rouyn Noranda. Dissolution-precipitation processes, physico-chemical parameters (oxygen concentration levels and pH), complexing DOM and microbial activity primarily control the release and mobilization of Fe in surficial soil environments (Cornell & Schwertmann, 2003).

Iron-(hydr)oxide phases such as ferrihydrite and hematite occur within and outside OM in the colloidal fraction (Figures 2-9 and 2-10). Ferrihydrite, ($Fe^{3+}{}_{10}O_{14}(OH)_2$) is a nanocrystalline phase, contains variable amounts of hydroxyl groups and is a widely distributed phase in the near-surface, low-temperature environment (Janney et al., 2000; Cornell & Schwertmann, 2003; Boily & Song, 2020). Hematite (Fe_2O_3) is stable under a wide range of thermodynamic conditions in the bulk environment and is usually formed as a result of the transformation of earlier-formed

ferrihydrite (Guo & Barnard, 2013). Schindler et al. (2019) showed that the aggregation of ferrihydrite nanoparticles promotes their transformation into hematite. This process may have occurred in the colloid depicted in Figure 2-9d, which contains most likely domains composed of hematite and ferrihydrite. The observations above show that Fe-(hydr)oxides in and outside of OM colloids often contain higher concentrations of Cu than the bulk soils. This close association of Fe-(hydr)oxides and Cu is in accord with spectroscopy data, which showed a close association of Cu and Fe even in organic-rich soils (Smith, 1999; Li et al., 2006; Strawn & Baker, 2007; Grover et al., 2012; Thomasi et al., 2015). It is also in accord; however, with the observation that Cu is enriched in the organic fraction of the soil (Mantha et al., 2019), as both, Cu and Fe-(hydr)oxides can be part of the organic fraction. These observations recorded at the nanometer scale show specifically that TEM of individual OM- colloids or particles is a valuable complementary analytical technique to sequential extractions and spectroscopy studies, especially when the results obtained by these techniques contradict each other (Li et al., 2006; Strawn & Baker, 2007; Thomasi et al., 2015).

2.5. Model of formation of CuS_x and Fe-(hydr)oxides in nanopores of organic colloids

The mass flux of Fe and Cu and the nucleation and stability of the CuS_x and Fe-hydr(oxide) phases in the colloidal OM may have been controlled by the following processes and steps:

I. ***Adsorption***

Although TEM and STEM cannot distinguish between adsorbed and incorporated Cu- and Fe-species, adsorption of these species played most likely a fundamental role in the nucleation of the observed phases in nanopores of the OM colloids (Figures 2-3, 2-4, 2-5, 2-6, 2-7, 2-8, 2-9, 2-10 and 2-11). Adsorption of Fe, and Cu aqueous species on the surface of the OM colloids was most likely promoted by electrostatic attractions as Fe- and Cu aqueous species, including protonated $Fe(HS)^+$ and $Cu(HS)^+$ species (Thompson & Goyne, 2012) as these are positively charged under weakly acidic conditions and OM colloids (PZC ≈ 2-3) and DOM species are commonly negatively charged (Kretzschmar & Schafer, 2005).

Additionally, the adsorption of positively-charged Cu- and Fe-species on OM colloids under weakly acidic conditions potentially reversed the charge of the OM, which then promoted the adsorption of anionic aqueous species such as $(SO_4)^{2-}$, HS^- and polynuclear FeS_x and CuS_x species (Tiberg et al., 2013; Schindler et al., 2016). Similarly, adsorption of HS on positive-

charged surfaces of Fe-(hydr)oxide colloids (PZC values > pH 7) might have partially reversed their surface charges and subsequently promoted the adsorption of positive-charged Cu aqueous species (Li et al., 2006; Li et al., 2007; Antelo et al., 2010; Tiberg et al., 2013; Fink et al., 2016).

Figures 2-7 and 2-8 show that the nucleation of Cu-sulfide phases in OM was controlled by the presence of silica inclusions. Silicification of OM is a common process in soils and is initiated by the adsorption of silicic acid to hydroxyl groups in holoocellulose and ligins, which are structural components of plants vascular tissue (Mustoe, 2017).

II. ***Development of porosity***

The rate of mineralization of OM by inorganic phases such as Fe-(hydr)oxides (Figures 2-9 and 2-10), amorphous silica (Figure 2-6 and 2-7) and Ca-carbonates and phosphates (Figure 2-11) controls the carbon budget of soil (Zhang & Zhou, 2018). Mustoe (2017) showed that the exterior surface of OM is mineralized first and that mineralization proceeds towards the interior of OM along cracks. The mineralization of OM follows here the same principle as a mineral replacement reaction (Figures 2-3, 2-4, 2-5, 2-6, 2-7, 2-8, 2-9, 2-10 and 2-11). During a mineral replacement reaction, dissolution-precipitation reactions occur along the interface between the dissolving (parent) and the replacing phase (daughter) (Putnis, 2015). The mass exchange between the interface and the bulk solution thus requires the development of porosity in the daughter phase; this process leads to generation of porosity in organic colloids (Figures 2-3 and 2-S4). In addition, the decomposition of OM through abiotic- and biotic-controlled oxidation processes result also in the formation of porosity (Modica & Lapierre, 2012), which may be recognized on the occurrence of nano- and micropores along the edges of colloids with low degrees of mineralization (Figure 2-6).

These considerations are in accord with the occurrence of CuS_x phases/species along the edges of the colloids (Figure 2-5) and their association with Fe-(hydr)oxides (Figure 2-9), amorphous silica (Figure 2-7) and Ca-carbonates and phosphates (Figure 2-11). The porosity most likely promoted the diffusion of Cu, $CuHS^+$ and HS^- species into the OM matrix and provided the necessary spaces for the nucleation of covellite, villamaninite, anilite, kuramite and unidentified Cu-nanoparticles (Figures 2-4, 2-5, 2-6, 2-7, 2-8 and 2-11).

III. *Nucleation*

Experimental and simulation studies indicate that nucleation of crystals preferentially occurs in regions of higher supersaturation within a matrix, which are usually areas of initial fluid penetration (Noiriel et al., 2016; Fazeli et al., 2020). Furthermore, pore size can limit or promote nucleation of phases within an OM matrix as the physical limitations of a pore control the size of a nucleus, which, in turn, controls the solubility of the nucleus itself; i.e. the smaller the nucleus the larger its surface energy and solubility (Stack, 2015). In this regard, the Pore Controlled Solubility (PCS) model states that a higher supersaturation is required to induce heterogeneous nucleation in a smaller than larger pore (or bulk fluid) (Putnis, 2015). Hence, nucleation of a phase at a given degree of intrinsic supersaturation may be inhibited in a smaller, but can occur in a larger nanopore. Furthermore, Stack et al. (2014) showed that the occurrence of polar functional groups along pore walls can enhance nucleation, suggesting that favorable surface chemistry can promote nucleation, even in nanopores. These observations are in accord with the occurrence of CuS_x phases in relatively larger pore spaces, which occur in close proximity to the more porous exterior surfaces of the colloids (Figures 2-6, 2-7 and 2-8).

The chemical composition of a pore wall and thus its polar character can not only induce nucleation, but it can be also actively involved in chemical reactions such as redox processes. For example, oxidized and reduced HA and FA functional groups in the OM matrix can be active redox centers (Akaighe et al., 2011; Fulda et al., 2013). Phenolic, hydroxyl and carboxylic groups of OM can induce a reduction of Fe-oxide phases via electron shuttling (Sansom & Biggin, 2001; Hyun et al., 2007). This process is also observed for other metal(loid)s such as Cu, where electron transfer reactions induced by redox-active natural OM result in the extensive formation of Cu^+ and metallic Cu (Maurer et al., 2013). These observations suggest that the polar character of pore walls in and on the surface of OM (reduced HA and FA groups) induced reduction of oxidized Cu and S species and enhanced nucleation. The Cu species mostly nucleated as sulfide phases such as covellite (Figures 2-4, 2-6 and 2-7) in which the oxidation state of Cu is +1. In this regard, the absence of CuS_x phases outside OM suggests that reduced organic functional groups specifically promoted the formation and enhanced stabilization of reduced S-species within the OM colloids. This conclusion is in accord with the formation of CuS_x nanoparticles on the surface or interlayer of reducing Fe-bearing minerals such as magnetite (Mantha et al., 2019) and metallic Cu in the interlayer of Fe^{2+}-bearing clay minerals (Ahn et al., 1997). However, the presence of the sulfates

$Fe_2(SO_4)_3$ and $Cr_2(SO_4)_3$ (Figure 2-S6) within the colloidal OM indicates that not all Fe^{3+} and sulfate (S^{6+}) species were reduced within OM and thus nucleated in the form of Fe^{3+}-sulfates.

The heterogeneous nucleation of covellite on silica inclusions in OM (Figure 2-7) suggests that silica stabilized and aided in the formation of covellite nanoparticles, in accord with the observed growth of covellite nanoparticles on glass surfaces during synthesis experiments (Yadav & Bajpai, 2018). The nucleation of covellite nanoparticles on the surface of silica inclusions in the OM (Figure 2-7) may have been promoted by the presence of hydrophilic functional groups on the surfaces of silica inclusions, which, in contrast to the hydrophobic sites in the OM, promoted the nucleation of covellite nanoparticles on these hydrophilic functional groups (Wang et al., 2019).

Other matrix effects affecting nucleation and adsorption of Cu species might have been the heterogeneous distribution of hydrophobic/hydrophilic or oxidized/reduced functional groups. For example, the parallel-elongated Cu enriched areas in an OM matrix of homogenous porosity (Figures 2-4 and 2-5a) might have been the result of a higher proportion of hydrophobic groups in localized bands, which promoted either the diffusion, adsorption, or nucleation of Cu-species and phases. However, these bands may also be explained with the Ostwald-Liesegang hypothesis. This hypothesis is used to explain the formation of Liesegang rings, which are banded growth features observed in silica-gel experiments, sedimentary rocks and solid-gaseous systems. The formation of these bands has been proposed to occur through various models (Hantz, 2006; Ramírez-Álvarez et al., 2016) based on crystal growth, nucleation, reaction and diffusion but Ostwald's pre-nucleation theory is the basic component of most of these models. The Ostwald-Liesegang hypothesis states that supersaturation and subsequent nucleation in a homogenous matrix occurs in localized bands which causes depletion of reactants and thus the lowering of supersaturation levels in the surrounding pore spaces (DeCelles & Gutschick, 1983; Steefel, 2008). This might relate to the occurrence of alternating Cu-rich zones in organic colloids (Figures 2-4 and 2-5).

IV. *Phase stability*

The thermodynamic stability of nanoparticles is shifted with the decrease in particle size and is mostly governed by the surface interactions due to unique physico-chemical properties at the nanoscale (Navrotsky, 2003; Chernyshova et al., 2007; Guo & Barnard, 2013). Hence, there is a crossover in surface free energy between phases stable at the bulk scale and those more stable at the nanoscale. For example, Navrotsky et al. (2008) determined the surface energy vs surface area

relationship for Fe-(hydr)oxides using dissolution enthalpies (approximated for ferrihydrite due to its variable chemical composition) and showed that akaganeite (β-FeOOH) becomes the most stable Fe-hydroxide with decreasing particle size. Pore-size controlled solubility and its control on the size of nucleus might have affected nucleation in the OM colloids as all the observed Fe-(hydr)oxide and CuS_x nanoparticles, clusters and layers have average diameters above 15 nm (Figures 2-4, 2-5, 2-6, 2-7, 2-8 and 2-9). However, the stability of the observed Fe-(hydr)oxides was most likely also affected by the presence of adsorbed silica species (Figure 2-9c) and DOM species in the OM colloids (Figure 2-10e). The co-existence of ferrihydrite and hematite (Figure 2-9) suggests that ferrihydrite formed first due to its lower surface energy and transformed later into the more stable phases such as hematite. This conclusion is also in accord with the observations by Schindler et al. (2019), who showed that hematite forms during the aggregation of ferrihydrite nanoparticles during the alteration of volcanic glass.

Silica species attached to the surface of ferrihydrite could have suppressed its transformation into the more stable Fe-(hydr)oxide phases such as goethite and hematite (Figure 2-9) (Rzepa et al., 2016). This suppression effect is controlled by Fe-O-Si surface terminations which impede crystal growth (Zhao et al., 1994). The presence of Si also hampers the rearrangement and structural ordering of particles, resulting in the need of higher temperatures for the transformation of ferrihydrite into, for example, hematite (Rzepa et al., 2016). Similarly, the transformation of ferrihydrite into goethite and hematite might have been suppressed through adsorbed HA or FA species or through the formation of organic coatings on their surface (Chen et al., 2015).

The stability of the CuS_x nanoparticles (Figures 2-4, 2-5, 2-6, 2-7 and 2-8) in the OM was most likely controlled by high concentration of sulfide species within the OM as the latter species lead to the stabilization of CuS_x phases with respect to metallic Cu (Amcoff & Holényi, 1992). This is in accord with observations by Weber et al. (2009), who showed that in a sulfide-free reduced environment, the absence of chelators cannot prevent the disproportionation of Cu^{1+}, and thus the formation of metallic Cu. The reaction of metallic Cu nanoparticles with reduced sulfur species, present as biogenic sulfides in flooded soils, most likely resulted in the formation of Cu-sulfide nanoparticles in these environments. Hence, the CuS_x phases in the OM colloids most likely

formed in nanopores with a high content of sulfide species stabilizing Cu^{+1} against its disproportionation.

2.6. The role of colloids in metal(loid)s transport

The literature on the colloid transport and mobilization models is very comprehensive and gives insights into the various factors that control the colloid-metal(loid) interactions and colloid mobilization (Roy & Dzombak, 1996; Khilar & Fogler, 1998; Citeau et al., 2003; Kretzschmar & Schafer, 2005; Sen & Khilar, 2006; Pédrot et al., 2008; Matura et al., 2012; Xia et al., 2018; Hoffmann et al., 2020). These studies indicate that movement of colloids and their role in the metal(loid) transport depends on the physico-chemical conditions induced by the land use and soil type such as clay mineralogy, water saturation, flow velocity and aqueous solution composition (ionic strength, pH and redox potential).

The majority of the colloids observed in this study are OM-based (n =62) and have high potential to mobilize the metal(loid)s as also evident from previous studies (Pokrovsky et al., 2006; Dahlqvist et al., 2007; Pédrot et al., 2008). Based on the sample size in this study, our data has; however, limited statistical representation but provides valuable insights into the colloidal OM-metal(loid) interactions at the nanoscale.

2.7. Conclusions

Our study shows the importance of nano-scale techniques in the characterization of Cu-bearing colloids in organic-rich soils impacted by smelter and coal-power plant emissions. These soils occur in many countries around the world such as in Lommel (Horckmans et al., 2006), Belgium; Anaconda (Burt et al., 2003), United States; Prescot (Clemente et al., 2008), United Kingdom and Flin Flon (McMartin et al., 1999), Canada (smelter impacted soils) Novocherkassk (Burachevskaya et al., 2019); Russia and Jinsha (Huang et al., 2017); China (coal-power plant impacted soils). The characterization of Cu-bearing soil constituents at the nano-scale is crucial to avoid pitfalls that arise due to the generalization of data gathered through techniques at a larger scale. Most of the identified Cu-Fe-bearing nano-phases located within OM colloids cannot be identified via bulk-scale techniques and therefore, their characterization provides valuable insights into mineralogical processes in colloidal OM at the nano-scale.

We showed in this study that the colloidal fraction in organic-rich soils is a chemically and structurally complex fraction containing nano-sized phases. The adsorption of ionic Cu-S-Fe-Cr-Sn-bearing species on OM colloids is facilitated by the electrostatic attractions, which also control the pre-mineralization of OM colloids. Porosity generated through decomposition and mineralization of OM along with the hydrophobic character of the OM matrix control diffusion of cationic and anionic species and nucleation of Cu-Fe-S-bearing phases within nanopores of OM. Heterogeneity of OM, involving variations in polar character (due to silica inclusions) and distribution of OM functional groups controlled in addition to porosity the nucleation of secondary phases. Pore-size controlled solubility effects inhibited the formation of nanoparticles below a critical size. Adsorption of silica species and high concentration of sulfide species stabilized most likely precipitates of ferrihydrite and CuS_x within nanopores of OM, respectively.

Our study provides new insights on colloid-metal(loid)s interactions and indicate that sequestration of metal(loid)s by colloidal OM can occur through their diffusion into the matrix of individual OM colloids and the formation of unexpected phases, which are most likely metastable with respect to the surrounding soil environment. The occurrence of 20 to 40% of the metal(loid)s in the colloidal fraction suggests that this formerly unknown sequestration process may play a vital role in the retention and mobilization of metal(loid)s in the soil environment. However, more field, as well as experimental studies, are needed to (a) quantify the proportion of metal(loid)-bearing phases in OM within colloidal fractions and (b) to identify in greater detail the underlying mechanisms of the diffusion of metal(loid)s into colloidal OM and the subsequent nucleation of secondary mineral phases.

2.8. References

Adamo, P., Dudka, S., Wilson, M., & McHardy, W. (1996). Chemical and Mineralogical Forms of Cu and Ni in Contaminated Soils from the Sudbury Mining and Smelting Region, Canada. *Environmental Pollution, 91*(1), 11-19.

Ahn, J. H., Xu, H., & Buseck, P. R. (1997). Transmission Electron Microscopy of Native Copper Inclusions in Illite. *Clays and Clay Minerals, 45*(2), 295-297.

Akaighe, N., MacCuspie, R. I., Navarro, D. A., Aga, D. S., Banerjee, S., Sohn, M., & Sharma, V. K. (2011). Humic Acid-Induced Silver Nanoparticle Formation under Environmentally Relevant Conditions. *Environmental Science & Technology, 45*(9), 3895-3901.

Alloway, B. J. (2012). *Heavy Metals in Soils: Trace Metals and Metalloids in Soils and Their Bioavailability* (Vol. 22): Springer Science & Business Media.

Amcoff, Ö., & Holényi, K. (1992). *Stability of Metallic Copper in the near Surface Environment*. Retrieved from

Antelo, J., Fiol, S., Pérez, C., Mariño, S., Arce, F., Gondar, D., & López, R. (2010). Analysis of Phosphate Adsorption onto Ferrihydrite Using the Cd-Music Model. *Journal of colloid and interface science, 347*(1), 112-119.

Balić-Žunić, T., Garavelli, A., Jakobsson, S. P., Jonasson, K., Katerinopoulos, A., Kyriakopoulos, K., & Acquafredda, P. (2016). Fumarolic Minerals: An Overview of Active European Volcanoes. *Updates in volcanology-from volcano modelling to volcano geology. InTech open access publishers*, 267-322.

Bigalke, M., Weyer, S., Kobza, J., & Wilcke, W. (2010). Stable Cu and Zn Isotope Ratios as Tracers of Sources and Transport of Cu and Zn in Contaminated Soil. *Geochimica et Cosmochimica Acta, 74*(23), 6801-6813.

Boily, J.-F., & Song, X. (2020). Direct Identification of Reaction Sites on Ferrihydrite. *Communications chemistry, 3*(1), 1-8.

Bonham-Carter, G., Henderson, P., Kliza, D., & Kettles, I. (2006). Comparison of Metal Distributions in Snow, Peat, Lakes and Humus around a Cu Smelter in Western Quebec, Canada. *Geochemistry: Exploration, Environment, Analysis, 6*(2-3), 215-228.

Buatier, M. D., Sobanska, S., & Elsass, F. (2001). Tem-Edx Investigation on Zn-and Pb-Contaminated Soils. *Applied Geochemistry, 16*(9-10), 1165-1177.

Burachevskaya, M., Minkina, T., Mandzhieva, S., Bauer, T., Chaplygin, V., Zamulina, I., Sushkova, S., Fedorenko, A., Ghazaryan, K., & Movsesyan, H. (2019). Study of Copper, Lead, and Zinc Speciation in the Haplic Chernozem Surrounding Coal-Fired Power Plant. *Applied Geochemistry, 104*, 102-108.

Burt, R., Wilson, M., Keck, T., Dougherty, B., Strom, D., & Lindahl, J. (2003). Trace Element Speciation in Selected Smelter-Contaminated Soils in Anaconda and Deer Lodge Valley, Montana, USA. *Advances in Environmental Research, 8*(1), 51-67.

Cai, L.-M., Wang, Q.-S., Luo, J., Chen, L.-G., Zhu, R.-L., Wang, S., & Tang, C.-H. (2019). Heavy Metal Contamination and Health Risk Assessment for Children near a Large Cu-Smelter in Central China. *Science of The Total Environment, 650*, 725-733.

Cao, J., Wang, G., Wang, T., Chen, J., Wenjing, G., Wu, P., He, X., & Xie, L. (2019). Copper Caused Reproductive Endocrine Disruption in Zebrafish (Danio Rerio). *Aquatic Toxicology, 211*, 124-136.

Caplette, J. N., & Schindler, M. (2018). Black Rock-Coatings in Trail, British Columbia, Canada: Records of Past Emissions of Lead, Zinc, Antimony, Arsenic, Tellurium, Tin, Selenium, Silver, Bismuth, and Indium-Bearing Atmospheric Contaminants. *The Canadian Mineralogist, 56*(2), 113-127.

Caplette, J. N., Schindler, M., & Kyser, T. K. (2015). The Black Rock Coatings in Rouyn-Noranda, Québec: Fingerprints of Historical Smelter Emissions and the Local Ore. *Canadian Journal of Earth Sciences, 52*(11), 952-965.

Caporale, A. G., & Violante, A. (2016). Chemical Processes Affecting the Mobility of Heavy Metals and Metalloids in Soil Environments. *Current Pollution Reports, 2*(1), 15-27.

Chen, C., Kukkadapu, R., & Sparks, D. L. (2015). Influence of Coprecipitated Organic Matter on Fe2+ (Aq)-Catalyzed Transformation of Ferrihydrite: Implications for Carbon Dynamics. *Environmental science & technology, 49*(18), 10927-10936.

Chernyshova, I., Hochella Jr, M., & Madden, A. (2007). Size-Dependent Structural Transformations of Hematite Nanoparticles. 1. Phase Transition. *Physical Chemistry Chemical Physics, 9*(14), 1736-1750.

Citeau, L., Lamy, I., van Oort, F., & Elsass, F. (2003). Colloidal Facilitated Transfer of Metals in Soils under Different Land Use. *Colloids and Surfaces A: Physicochemical and Engineering Aspects, 217*(1-3), 11-19.

Clemente, R., Dickinson, N. M., & Lepp, N. W. (2008). Mobility of Metals and Metalloids in a Multi-Element Contaminated Soil 20 Years after Cessation of the Pollution Source Activity. *Environmental Pollution, 155*(2), 254-261.

Cornell, R. M., & Schwertmann, U. (2003). *The Iron Oxides: Structure, Properties, Reactions, Occurrences and Uses*: John Wiley & Sons.

Dahlqvist, R., Andersson, K., Ingri, J., Larsson, T., Stolpe, B., & Turner, D. (2007). Temporal Variations of Colloidal Carrier Phases and Associated Trace Elements in a Boreal River. *Geochimica et Cosmochimica Acta, 71*(22), 5339-5354.

Dai, M., Martin, J.-M., & Cauwet, G. (1995). The Significant Role of Colloids in the Transport and Transformation of Organic Carbon and Associated Trace Metals (Cd, Cu and Ni) in the Rhône Delta (France). *Marine Chemistry, 51*(2), 159-175.

de Romaña, D. L., Olivares, M., Uauy, R., & Araya, M. (2011). Risks and Benefits of Copper in Light of New Insights of Copper Homeostasis. *Journal of Trace Elements in Medicine and Biology, 25*(1), 3-13.

DeCelles, P. G., & Gutschick, R. C. (1983). Mississippian Wood-Grained Chert and Its Significance in the Western Interior United States. *Journal of Sedimentary Research, 53*(4), 1175-1191.

Denaix, L., Semlali, R., & Douay, F. (2001). Dissolved and Colloidal Transport of Cd, Pb, and Zn in a Silt Loam Soil Affected by Atmospheric Industrial Deposition. *Environmental Pollution, 114*(1), 29-38.

Denis, F. T. (1933). An Investigation of the Mineral Composition of the Ores of Noranda Mines Ltd. *McGill University Libraries*.

Derome, J., & Lindross, A.-J. (1998). Copper and Nickel Mobility in Podzolic Forest Soils Subjected to Heavy Metal and Sulphur Deposition in Western Finland. *Chemosphere, 36*(4-5), 1131-1136.

Dinis, L., Bégin, C., Savard, M. M., & Parent, M. (2020). Impacts of Smelter Atmospheric Emissions on Forest Nutrient Cycles: Evidence from Soils and Tree Rings. *Science of The Total Environment*, 141427.

Driessnack, M. K., Jamwal, A., & Niyogi, S. (2017). Effects of Chronic Exposure to Waterborne Copper and Nickel in Binary Mixture on Tissue-Specific Metal Accumulation and Reproduction in Fathead Minnow (Pimephales Promelas). *Chemosphere, 185*, 964-974.

Dupraz, C., Reid, R. P., Braissant, O., Decho, A. W., Norman, R. S., & Visscher, P. T. (2009). Processes of Carbonate Precipitation in Modern Microbial Mats. *Earth-Science Reviews, 96*(3), 141-162.

Ettler, V. (2016). Soil Contamination near Non-Ferrous Metal Smelters: A Review. *Applied Geochemistry, 64*, 56-74.

Ettler, V., Mihaljevič, M., & Komárek, M. (2004). Icp-Ms Measurements of Lead Isotopic Ratios in Soils Heavily Contaminated by Lead Smelting: Tracing the Sources of Pollution. *Analytical and bioanalytical chemistry, 378*(2), 311-317.

Ettler, V., Vítková, M., Mihaljevič, M., Šebek, O., Klementová, M., Veselovský, F., Vybíral, P., & Kříbek, B. (2014). Dust from Zambian Smelters: Mineralogy and Contaminant Bioaccessibility. *Environmental geochemistry and health, 36*(5), 919-933.

Fazeli, H., Masoudi, M., Patel, R. A., Aagaard, P., & Hellevang, H. (2020). Pore-Scale Modeling of Nucleation and Growth in Porous Media. *ACS Earth and Space Chemistry, 4*(2), 249-260.

Fink, J. R., Inda, A. V., Tiecher, T., & Barrón, V. (2016). Iron Oxides and Organic Matter on Soil Phosphorus Availability. *Ciencia e agrotecnologia, 40*(4), 369-379.

Freedman, B., & Hutchinson, T. (1980). Pollutant Inputs from the Atmosphere and Accumulations in Soils and Vegetation near a Nickel–Copper Smelter at Sudbury, Ontario, Canada. *Canadian Journal of Botany, 58*(1), 108-132.

Fulda, B., Voegelin, A., Maurer, F., Christl, I., & Kretzschmar, R. (2013). Copper Redox Transformation and Complexation by Reduced and Oxidized Soil Humic Acid. 1. X-Ray Absorption Spectroscopy Study. *Environmental Science & Technology, 47*(19), 10903-10911.

Gaetke, L. M., Chow-Johnson, H. S., & Chow, C. K. (2014). Copper: Toxicological Relevance and Mechanisms. *Archives of toxicology, 88*(11), 1929-1938.

Gammons, C. H., & Frandsen, A. K. (2001). Fate and Transport of Metals in H2s-Rich Waters at a Treatment Wetland. *Geochemical Transactions, 2*(1), 1-15.

Gashkina, N., Tatsii, Y. G., Udachin, V., & Aminov, P. (2015). Biogeochemical Indication of Environmental Contamination: A Case Study of a Large Copper Smelter. *Geochemistry International, 53*(3), 253-264.

Grolimund, D., & Borkovec, M. (2005). Colloid-Facilitated Transport of Strongly Sorbing Contaminants in Natural Porous Media: Mathematical Modeling and Laboratory Column Experiments. *Environmental science & technology, 39*(17), 6378-6386.

Grover, V. A., Hu, J., Engates, K. E., & Shipley, H. J. (2012). Adsorption and Desorption of Bivalent Metals to Hematite Nanoparticles. *Environmental Toxicology and Chemistry, 31*(1), 86-92.

Guasch, H., Paulsson, M., & Sabater, S. (2002). Effect of Copper on Algal Communities from Oligotrophic Calcareous Streams1. *Journal of Phycology, 38*(2), 241-248.

Guo, H., & Barnard, A. S. (2013). Naturally Occurring Iron Oxide Nanoparticles: Morphology, Surface Chemistry and Environmental Stability. *Journal of Materials Chemistry A, 1*(1), 27-42.

Gustafsson, J. P., Pechová, P., & Berggren, D. (2003). Modeling Metal Binding to Soils: The Role of Natural Organic Matter. *Environmental Science & Technology, 37*(12), 2767-2774.

Hantz, P. (2006). *Pattern Formation in a New Class of Precipitation Reactions.* Verlag nicht ermittelbar.

Hartland, A., Larsen, J. R., Andersen, M. S., Baalousha, M., & O'Carroll, D. (2015). Association of Arsenic and Phosphorus with Iron Nanoparticles between Streams and Aquifers: Implications for Arsenic Mobility. *Environmental Science & Technology, 49*(24), 14101-14109.

Hayashi, M., Kuge, T., Endoh, D., Nakayama, K., Arikawa, J., Takazawa, A., & Okui, T. (2000). Hepatic Copper Accumulation Induces DNA Strand Breaks in the Liver Cells of Long-Evans Cinnamon Strain Rats. *Biochemical and Biophysical Research Communications, 276*(1), 174-178.

Henderson, P., McMartin, I., Hall, G., Percival, J., & Walker, D. (1998). The Chemical and Physical Characteristics of Heavy Metals in Humus and Till in the Vicinity of the Base Metal Smelter at Flin Flon, Manitoba, Canada. *Environmental Geology, 34*(1), 39-58.

Hodson, P., Borgmann, U., & Shear, H. (1979). Nriagu Io.(Ed). Copper in the Environment. Part 2: Health Effects: John Wiley, New York.

Hofacker, A. F., Voegelin, A., Kaegi, R., & Kretzschmar, R. (2013a). Mercury Mobilization in a Flooded Soil by Incorporation into Metallic Copper and Metal Sulfide Nanoparticles. *Environmental Science & Technology, 47*(14), 7739-7746.

Hofacker, A. F., Voegelin, A., Kaegi, R., Weber, F.-A., & Kretzschmar, R. (2013b). Temperature-Dependent Formation of Metallic Copper and Metal Sulfide Nanoparticles During Flooding of a Contaminated Soil. *Geochimica et Cosmochimica Acta, 103*, 316-332.

Hoffmann, K., Bouchet, S., Christl, I., Kaegi, R., & Kretzschmar, R. (2020). Effect of Nom on Copper Sulfide Nanoparticle Growth, Stability, and Oxidative Dissolution. *Environmental Science: Nano, 7*(4), 1163-1178.

Horckmans, L., Swennen, R., & Deckers, J. (2006). Geochemical and Mineralogical Study of a Site Severely Polluted with Heavy Metals (Maatheide, Lommel, Belgium). *Environmental Geology, 50*(5), 725-742.

Huang, X., Hu, J., Qin, F., Quan, W., Cao, R., Fan, M., & Wu, X. (2017). Heavy Metal Pollution and Ecological Assessment around the Jinsha Coal-Fired Power Plant (China). *International Journal of Environmental Research and Public Health, 14*(12), 1589.

Hyun, J.-H., Smith, A. C., & Kostka, J. E. (2007). Relative Contributions of Sulfate-and Iron (Iii) Reduction to Organic Matter Mineralization and Process Controls in Contrasting Habitats of the Georgia Saltmarsh. *Applied Geochemistry, 22*(12), 2637-2651.

Ilton, E. S., Earley, D., Marozas, D. C., & Veblen, D. R. (1992). Reaction of Some Trioctahedral Micas with Copper Sulfate Solutions at 25 Degrees C and 1 Atmosphere; an Electron Microprobe and Tem Investigation. *Economic Geology, 87*(7), 1813-1829.

Ilton, E. S., & Veblen, D. R. (1988). Copper Inclusions in Sheet Silicates from Porphyry Cu Deposits. *Nature, 334*(6182), 516-518.

Ilton, E. S., & Veblen, D. R. (1993). Origin and Mode of Copper Enrichment in Biotite from Rocks Associated with Porphyry Copper Deposits; a Transmission Electron Microscopy Investigation. *Economic Geology, 88*(4), 885-900.

Janney, D. E., Cowley, J. M., & Buseck, P. R. (2000). Transmission Electron Microscopy of Synthetic 2-and 6-Line Ferrihydrite. *Clays and Clay Minerals, 48*(1), 111-119.

Kerr, D. J., & Gibson, H. L. (1993). A Comparison of the Horne Volcanogenic Massive Sulfide Deposit and Intracauldron Deposits of the Mine Sequence, Noranda, Quebec. *Economic Geology, 88*(6), 1419-1442.

Kettles, I. M., & Bonham-Carter, G. F. (2002). Modelling Dispersal of Metals from a Copper Smelter at Rouyn-Noranda (Québec, Canada) Using Peatland Data. *Geochemistry: Exploration, Environment, Analysis, 2*(2), 99-110.

Khilar, K. C., & Fogler, H. S. (1998). Practical Consequences of Release and Migration of Fines in Porous Media *Migrations of Fines in Porous Media* (pp. 1-8): Springer.

Knight, R., & Henderson, P. (2006). Smelter Dust in Humus around Rouyn-Noranda, Quebec. *Geochemistry: Exploration, Environment, Analysis, 6*(2-3), 203-214.

Kopittke, P. M., & Menzies, N. W. (2006). Effect of Cu Toxicity on Growth of Cowpea (Vigna Unguiculata). *Plant and Soil, 279*(1), 287-296.

Kretzschmar, R., & Schafer, T. (2005). Metal Retention and Transport on Colloidal Particles in the Environment. *Elements, 1*(4), 205-210.

Kříbek, B., Majer, V., Veselovský, F., & Nyambe, I. (2010). Discrimination of Lithogenic and Anthropogenic Sources of Metals and Sulphur in Soils of the Central-Northern Part of the Zambian Copperbelt Mining District: A Topsoil Vs. Subsurface Soil Concept. *Journal of Geochemical Exploration, 104*(3), 69-86.

Lanteigne, S., Schindler, M., & McDonald, A. (2014). Distribution of Metals and Metalloids in Smelter-Derived Particulate Matter in Soils and Mineralogical Insights into Their Retention and Release in a Low-T Environment. *The Canadian Mineralogist, 52*(3), 453-471.

Lanteigne, S., Schindler, M., McDonald, A. M., Skeries, K., Abdu, Y., Mantha, N. M., Murayama, M., Hawthorne, F. C., & Hochella, M. F. (2012). Mineralogy and Weathering of Smelter-Derived Spherical Particles in Soils: Implications for the Mobility of Ni and Cu in the Surficial Environment. *Water, Air, & Soil Pollution, 223*(7), 3619-3641.

Lee, S., Ko, I.-W., Yoon, I.-H., Kim, D.-W., & Kim, K.-W. (2019). Colloid Mobilization and Heavy Metal Transport in the Sampling of Soil Solution from Duckum Soil in South Korea. *Environmental Geochemistry and Health, 41*(1), 469-480.

Letelier, M. E., Sánchez-Jofré, S., Peredo-Silva, L., Cortés-Troncoso, J., & Aracena-Parks, P. (2010). Mechanisms Underlying Iron and Copper Ions Toxicity in Biological Systems: Pro-Oxidant Activity and Protein-Binding Effects. *Chemico-biological interactions, 188*(1), 220-227.

Leverington, D. W., & Schindler, M. (2018). Delineating Areas of Past Environmental Degradation near Smelters Using Rock Coatings: A Case Study at Rouyn-Noranda, Quebec. *Scientific reports, 8*(1), 1-15.

Li, R., Li, J., Cui, L., Wu, Y., Fu, H., Chen, J., & Chen, M. (2017). Atmospheric Emissions of Cu and Zn from Coal Combustion in China: Spatio-Temporal Distribution, Human Health Effects, and Short-Term Prediction. *Environmental Pollution, 229*, 724-734.

Li, W., Zhang, S., Jiang, W., & Shan, X.-q. (2006). Effect of Phosphate on the Adsorption of Cu and Cd on Natural Hematite. *Chemosphere, 63*(8), 1235-1241.

Li, W., Zhang, S., & Shan, X.-q. (2007). Surface Modification of Goethite by Phosphate for Enhancement of Cu and Cd Adsorption. *Colloids and Surfaces A: Physicochemical and Engineering Aspects, 293*(1-3), 13-19.

Liang, Q., & Dedon, P. C. (2001). Cu (Ii)/H2o2-Induced DNA Damage Is Enhanced by Packaging of DNA as a Nucleosome. *Chemical research in toxicology, 14*(4), 416-422.

Liu, H.-L., Zhou, J., Li, M., Obrist, D., Wang, X.-Z., & Zhou, J. (2021). Chemical Speciation of Trace Metals in Atmospheric Deposition and Impacts on Soil Geochemistry and Vegetable Bioaccumulation near a Large Copper Smelter in China. *Journal of hazardous materials, 413*, 125346.

Mandal, A., & Sengupta, D. (2006). An Assessment of Soil Contamination Due to Heavy Metals around a Coal-Fired Thermal Power Plant in India. *Environmental Geology, 51*(3), 409-420.

Mantha, H., Schindler, M., & Hochella, M. F. (2019). Occurrence and Formation of Incidental Metallic Cu and Cus Nanoparticles in Organic-Rich Contaminated Surface Soils in Timmins, Ontario. *Environmental Science: Nano, 6*(1), 163-179.

Mantha, N. M., Schindler, M., Murayama, M., & Hochella Jr, M. F. (2012). Silica-and Sulfate-Bearing Rock Coatings in Smelter Areas: Products of Chemical Weathering and Atmospheric Pollution I. Formation and Mineralogical Composition. *Geochimica et Cosmochimica Acta, 85*, 254-274.

Martley, E., Gulson, B., & Pfeifer, H.-R. (2004). Metal Concentrations in Soils around the Copper Smelter and Surrounding Industrial Complex of Port Kembla, Nsw, Australia. *Science of The Total Environment, 325*(1-3), 113-127.

Masson, S., Couillard, Y., Campbell, P. G., Olsen, C., Pinel-Alloul, B., & Perceval, O. (2010). Responses of Two Sentinel Species (Hexagenia Limbata—Mayfly; Pyganodon Grandis—Bivalve) Along Spatial Cadmium Gradients in Lakes and Rivers in Northwestern Québec. *Journal of Environmental Monitoring, 12*(1), 143-158.

Matura, M., Ettler, V., & Klementová, M. (2012). Transmission Electron Microscopy Investigation of Colloids and Particles from Landfill Leachates. *Waste Management & Research, 30*(5), 530-541.

Maurer, F., Christl, I., Fulda, B., Voegelin, A., & Kretzschmar, R. (2013). Copper Redox Transformation and Complexation by Reduced and Oxidized Soil Humic Acid. 2.

Potentiometric Titrations and Dialysis Cell Experiments. *Environmental Science & Technology, 47*(19), 10912-10921.

McMartin, I., Henderson, P., & Nielsen, E. (1999). Impact of a Base Metal Smelter on the Geochemistry of Soils of the Flin Flon Region, Manitoba and Saskatchewan. *Canadian Journal of Earth Sciences, 36*(2), 141-160.

McNaught, A. D., & Wilkinson, A. (1997). Compendium of Chemical Terminology. Iupac Recommendations.

Modica, C. J., & Lapierre, S. G. (2012). Estimation of Kerogen Porosity in Source Rocks as a Function of Thermal Transformation: Example from the Mowry Shale in the Powder River Basin of Wyoming. *AAPG bulletin, 96*(1), 87-108.

Morin, S., Lambert, A. S., Rodriguez, E. P., Dabrin, A., Coquery, M., & Pesce, S. (2017). Changes in Copper Toxicity Towards Diatom Communities with Experimental Warming. *Journal of Hazardous Materials, 334*, 223-232.

Mustoe, G. E. (2017). Wood Petrifaction: A New View of Permineralization and Replacement. *Geosciences, 7*(4), 119.

Nachtegaal, M., Marcus, M., Sonke, J., Vangronsveld, J., Livi, K., Van der Lelie, D., & Sparks, D. (2005). Effects of in Situ Remediation on the Speciation and Bioavailability of Zinc in a Smelter Contaminated Soil. *Geochimica et Cosmochimica Acta, 69*(19), 4649-4664.

Navrotsky, A. (2003). Energetics of Nanoparticle Oxides: Interplay between Surface Energy and Polymorphism. *Geochemical Transactions, 4*(1), 1-4.

Navrotsky, A., Mazeina, L., & Majzlan, J. (2008). Size-Driven Structural and Thermodynamic Complexity in Iron Oxides. *Science, 319*(5870), 1635-1638.

Noiriel, C., Steefel, C. I., Yang, L., & Bernard, D. (2016). Effects of Pore-Scale Precipitation on Permeability and Flow. *Advances in Water Resources, 95*, 125-137.

Oursel, B., Garnier, C., Durrieu, G., Mounier, S., Omanović, D., & Lucas, Y. (2013). Dynamics and Fates of Trace Metals Chronically Input in a Mediterranean Coastal Zone Impacted by a Large Urban Area. *Marine Pollution Bulletin, 69*(1-2), 137-149.

Pédrot, M., Dia, A., Davranche, M., Bouhnik-Le Coz, M., Henin, O., & Gruau, G. (2008). Insights into Colloid-Mediated Trace Element Release at the Soil/Water Interface. *Journal of Colloid and Interface Science, 325*(1), 187-197.

Perito, B., & Mastromei, G. (2011). Molecular Basis of Bacterial Calcium Carbonate Precipitation. *Molecular Biomineralization*, 113-139.

Pham, A. N., Rose, A. L., & Waite, T. D. (2012). Kinetics of Cu (Ii) Reduction by Natural Organic Matter. *The Journal of Physical Chemistry A, 116*(25), 6590-6599.

Pokrovsky, O., Schott, J., & Dupré, B. (2006). Trace Element Fractionation and Transport in Boreal Rivers and Soil Porewaters of Permafrost-Dominated Basaltic Terrain in Central Siberia. *Geochimica et Cosmochimica Acta, 70*(13), 3239-3260.

Putnis, A. (2015). Transient Porosity Resulting from Fluid–Mineral Interaction and Its Consequences. *Reviews in Mineralogy and Geochemistry, 80*(1), 1-23.

Qasim, B., Motelica-Heino, M., Joussein, E., Soubrand, M., & Gauthier, A. (2015). Potentially Toxic Element Phytoavailability Assessment in Technosols from Former Smelting and Mining Areas. *Environmental Science and Pollution Research, 22*(8), 5961-5974.

Ramírez-Álvarez, E., Montoya, F., Buhse, T., Rios-Herrera, W., Torres-Guzmán, J., Rivera, M., Martínez-Mekler, G., & Müller, M. F. (2016). On the Dynamics of Liesegang-Type Pattern Formation in a Gaseous System. *Scientific reports, 6*(1), 1-13.

Roy, S. B., & Dzombak, D. A. (1996). Colloid Release and Transport Processes in Natural and Model Porous Media. *Colloids and Surfaces A: Physicochemical and Engineering Aspects, 107*, 245-262.

Rozan, T. F., Lassman, M. E., Ridge, D. P., & Luther, G. W. (2000). Evidence for Iron, Copper and Zinc Complexation as Multinuclear Sulphide Clusters in Oxic Rivers. *Nature, 406*(6798), 879-882.

Rzepa, G., Pieczara, G., Gaweł, A., Tomczyk, A., & Zalecki, R. (2016). The Influence of Silicate on Transformation Pathways of Synthetic 2-Line Ferrihydrite. *Journal of Thermal Analysis and Calorimetry, 125*(1), 407-421.

Sansom, M. S., & Biggin, P. C. (2001). Water at the Nanoscale. *Nature, 414*(6860), 157-159.

Sayre, L. M., Perry, G., Harris, P. L., Liu, Y., Schubert, K. A., & Smith, M. A. (2000). In Situ Oxidative Catalysis by Neurofibrillary Tangles and Senile Plaques in Alzheimer's Disease: A Central Role for Bound Transition Metals. *Journal of Neurochemistry, 74*(1), 270-279.

Schindler, M., & Hochella Jr, M. F. (2016). Nanomineralogy as a New Dimension in Understanding Elusive Geochemical Processes in Soils: The Case of Low-Solubility-Index Elements. *Geology, 44*(7), 515-518.

Schindler, M., & Hochella, M. F. (2017). Sequestration of Pb–Zn–Sb-and as-Bearing Incidental Nanoparticles by Mineral Surface Coatings and Mineralized Organic Matter in Soils. *Environmental Science: Processes & Impacts*, *19*(8), 1016-1027.

Schindler, M., Lanteigne, S., McDonald, A. M., & Hochella Jr, M. F. (2016). Evidence of Cu-and Ni-Bearing Surface Precipitates and Adsorption Complexes in Remediated Soils at the Nanoscale: A Tem, Micro-Raman, and Laser-Ablation Icp-Ms Study of Mineral Surface Coatings. *The Canadian Mineralogist*, *54*(1), 285-309.

Schindler, M., Michel, S., Batcheldor, D., & Hochella Jr, M. F. (2019). A Nanoscale Study of the Formation of Fe-(Hydr) Oxides in a Volcanic Regolith: Implications for the Understanding of Soil Forming Processes on Earth and Mars. *Geochimica et Cosmochimica Acta*, *264*, 43-66.

Schindler, M., Santosh, M., Dotto, G., Silva, L. F., & Hochella Jr, M. F. (2021). A Review on Pb-Bearing Nanoparticles, Particulate Matter and Colloids Released from Mining and Smelting Activities. *Gondwana Research*.

Schindler, M., & Singer, D. M. (2017). Mineral Surface Coatings: Environmental Records at the Nanoscale. *Elements: An International Magazine of Mineralogy, Geochemistry, and Petrology*, *13*(3), 159-164.

Sen, T. K., & Khilar, K. C. (2006). Review on Subsurface Colloids and Colloid-Associated Contaminant Transport in Saturated Porous Media. *Advances in colloid and interface science*, *119*(2-3), 71-96.

Sheldon, A., & Menzies, N. (2005). The Effect of Copper Toxicity on the Growth and Root Morphology of Rhodes Grass (Chloris Gayana Knuth.) in Resin Buffered Solution Culture. *Plant and Soil*, *278*(1), 341-349.

Skalny, A. V., Zhukovskaya, E. V., Kireeva, G. N., Skalnaya, M. G., Grabeklis, A. R., Radysh, I. V., Shakieva, R. A., Nikonorov, A. A., & Tinkov, A. A. (2018). Whole Blood and Hair Trace Elements and Minerals in Children Living in Metal-Polluted Area near Copper Smelter in Karabash, Chelyabinsk Region, Russia. *Environmental Science and Pollution Research*, *25*(3), 2014-2020.

Smith, K. S. (1999). Metal Sorption on Mineral Surfaces: An Overview with Examples Relating to Mineral Deposits. *The Environmental Geochemistry of Mineral Deposits. Part B: Case Studies and Research Topics*, *6*, 161-182.

Stack, A. G. (2015). Precipitation in Pores: A Geochemical Frontier. *Reviews in Mineralogy and Geochemistry, 80*(1), 165-190.

Stack, A. G., Fernandez-Martinez, A., Allard, L. F., Bañuelos, J. L., Rother, G., Anovitz, L. M., Cole, D. R., & Waychunas, G. A. (2014). Pore-Size-Dependent Calcium Carbonate Precipitation Controlled by Surface Chemistry. *Environmental Science & Technology, 48*(11), 6177-6183.

Stafilov, T., Šajn, R., Pančevski, Z., Boev, B., Frontasyeva, M. V., & Strelkova, L. P. (2010). Heavy Metal Contamination of Topsoils around a Lead and Zinc Smelter in the Republic of Macedonia. *Journal of Hazardous Materials, 175*(1-3), 896-914.

Steefel, C. I. (2008). Geochemical Kinetics and Transport *Kinetics of Water-Rock Interaction* (pp. 545-589): Springer.

Strawn, D. G., & Baker, L. L. (2007). Speciation of Cu in a Contaminated Agricultural Soil Measured by Xafs, M-Xafs, and M-Xrf. *Environmental Science & Technology, 42*(1), 37-42.

Suárez, S., Nieto, F., Velasco, F., & Martín, F. J. (2011). Serpentine and Chlorite as Effective Ni-Cu Sinks During Weathering of the Aguablanca Sulphide Deposit (Sw Spain). Tem Evidence for Metal-Retention Mechanisms in Sheet Silicates. *European Journal of Mineralogy, 23*(2), 179-196.

Sullivan, P., Agardy, F. J., & Clark, J. J. (2005). *The Environmental Science of Drinking Water*: Elsevier.

Telmer, K. H., Daneshfar, B., Sanborn, M. S., Kliza-Petelle, D., & Rancourt, D. G. (2006). The Role of Smelter Emissions and Element Remobilization in the Sediment Chemistry of 99 Lakes around the Horne Smelter, Quebec. *Geochemistry: Exploration, Environment, Analysis, 6*(2-3), 187-202.

Thomasi, S., Fernandes, R., Fontes, R., & Jordão, C. (2015). Sequential Extraction of Copper, Nickel, Zinc, Lead and Cadmium from Brazilian Oxysols: Metal Leaching and Metal Distribution in Soil Fractions. *International Journal of Environmental Studies, 72*(1), 41-55.

Thompson, A., & Goyne, K. (2012). Introduction to the Sorption of Chemical Constituents in Soils. *Nature Education Knowledge, 4*(4), 7.

Tiberg, C., Sjöstedt, C., Persson, I., & Gustafsson, J. P. (2013). Phosphate Effects on Copper (Ii) and Lead (Ii) Sorption to Ferrihydrite. *Geochimica et Cosmochimica Acta, 120*, 140-157.

Turhan, Ş., Garad, A., Hançerlioğulları, A., Kurnaz, A., Gören, E., Duran, C., Karataşlı, M., Altıkulaç, A., Savacı, G., & Aydın, A. (2020). Ecological Assessment of Heavy Metals in Soil around a Coal-Fired Thermal Power Plant in Turkey. *Environmental Earth Sciences, 79*(6), 1-15.

Wang, M., Dissanayake, T. U., Park, C., Gaskell, K., & Woehl, T. J. (2019). Nanoscale Mapping of Nonuniform Heterogeneous Nucleation Kinetics Mediated by Surface Chemistry. *Journal of the American Chemical Society, 141*(34), 13516-13524.

Wang, Y. (2014). Nanogeochemistry: Nanostructures, Emergent Properties and Their Control on Geochemical Reactions and Mass Transfers. *Chemical Geology, 378*, 1-23.

Weber, F.-A., Voegelin, A., Kaegi, R., & Kretzschmar, R. (2009). Contaminant Mobilization by Metallic Copper and Metal Sulphide Colloids in Flooded Soil. *Nature Geoscience, 2*(4), 267-271.

Wilkinson, K. J., Negre, J.-C., & Buffle, J. (1997). Coagulation of Colloidal Material in Surface Waters: The Role of Natural Organic Matter. *Journal of Contaminant Hydrology, 26*(1-4), 229-243.

Xia, B., Qiu, H., Knorr, K.-H., Blodau, C., & Qiu, R. (2018). Occurrence and Fate of Colloids and Colloid-Associated Metals in a Mining-Impacted Agricultural Soil Upon Prolonged Flooding. *Journal of Hazardous Materials, 348*, 56-66.

Xu, W., & Parise, J. B. (2012). Temperature and Humidity Effects on Ferric Sulfate Stability and Phase Transformation. *American Mineralogist, 97*(2-3), 378-383.

Yadav, S., & Bajpai, P. K. (2018). Effect of Substrate on Cus/Pva Nanocomposite Thin Films Deposited on Glass and Silicon Substrate. *Soft Nanoscience Letters, 8*(2), 9-19.

Zdanowicz, C. M., Banic, C. M., Paktunc, D. A., & Kliza-Petelle, D. A. (2006). Metal Emissions from a Cu Smelter, Rouyn-Noranda, Quebec: Characterization of Particles Sampled in Air and Snow. *Geochemistry: Exploration, Environment, Analysis, 6*(2-3), 147-162.

Zhang, H., & Zhou, Z. (2018). Recalcitrant Carbon Controls the Magnitude of Soil Organic Matter Mineralization in Temperate Forests of Northern China. *Forest Ecosystems, 5*(1), 1-10.

Zhao, J., Huggins, F. E., Feng, Z., & Huffman, G. P. (1994). Ferrihydrite: Surface Structure and Its Effects on Phase Transformation. *Clays and Clay Minerals, 42*(6), 737-746.

Chapter 3: Atom probe tomography and transmission electron microscopy: A powerful combination to characterize the speciation and distribution of Cu in nano-sized pore spaces of organic matter

Abstract

This study explores the role of nanopores within organic matter (OM) in the sequestration of Cu and other metal(loid)s in the contaminated oxic soils around the Horne smelter, Rouyn Noranda, Quebec, Canada. The sequestration of Cu in nanopores within OM is studied using a combination of scanning electron microscopy (SEM), TEM and APT. TEM analysis indicates that Cu occurs as incidental NP of Cu-Zn-bearing magnetite (Fe_3O_4), cuprite (Cu_2O) and spertiniite ($Cu(OH)_2$) within pre-mineralized OM. APT analysis indicates the occurrence of Cu-(hydr)oxide clusters composed of dimers and trimers within the OM matrix, which may be the precursors of cuprite or spertiniite incidental NP. Incidental NP of predominantly Fe-(hydr)oxides occur in close association with silicates, indicating that the favorable surface chemistry of silicates (presence of hydrophilic Si-O groups) promotes their formation. Availability of metal(loid)-bearing species controlled by the hydrodynamic properties of pore channels and PCS effects controls the formation of incidental NP within pre-mineralized OM. A model is developed which proposes that the sequestration of Cu and other metal(loids) in OM requires (I) pre-mineralization of the OM matrix, adsorption of Cu aqueous species and their diffusion into OM matrix; (II) formation of precursors and nucleation and stabilization of Cu-bearing incidental NP; (III) the presence of porous zones and hydrophobic functional groups which promote the diffusion of ions within OM; (IV) a favorable surface chemistry of silicates which promotes heterogeneous nucleation; (V) the availability of metal(loid) species, which in turn is controlled by the hydrodynamic properties of the pore channels; (VI) the presence of silicates and silicic acid in OM which stabilize meta-stable phases such as ferrihydrite through inhibiting their transformation and promoting their aggregation.

3.1. Introduction

The development of instrumental techniques for the analysis of materials at a sub-nanometer scale is one of the recent trends in geochronological and geochemical research. This

development is driven by the fact that sub-nanometer analysis provides detailed insights into complex geochemical processes occurring during the alteration of geological material and thus complements the interpretation of data collected at larger scales (Reddy et al., 2020). Multi-scale tiered workflows for the characterization of geological material are becoming a common approach to get a better understanding of the geological and environmental processes. However, few analytical techniques are capable of the compositional analysis of geological material at sub-nanometer scale and one such technique is the APT, a technique based on time-of-flight mass spectrometry that has the ability to characterize ionic species and relative position with a sub-nanometer spatial resolution (Saxey et al., 2018). This technique has produced novel contributions that address questions related to the distribution of isotopes and elements in both terrestrial and extra-terrestrial minerals due to its low detection limit (parts per million) and its ability to map the 3-D composition of a sample at the atomic scale (Blum et al., 2018; Devaraj et al., 2018).

APT has been in development since the 1970s and was initially used in materials science for the analysis of conductive materials but the total number of APT publications has gradually increased since 2005 due to the commercial development of laser-assisted APT (Reddy et al., 2020). Since then APT is used to characterize a wide range of geological materials including carbonates (Branson et al., 2016; Reinhard et al., 2016; Pérez-Huerta & Laiginhas, 2018), oxides (El Dien et al., 2019; Genareau et al., 2019; Taylor et al., 2019), sulfides (Gopon et al., 2019; Wu et al., 2019), sulfates (Schmidt et al., 2019), silicates (Cao et al., 2019) and diamonds (Schirhagl et al., 2015; Mukherjee et al., 2016) at the sub-nanometer scale. However, the majority of APT studies have focused on the trace element distribution and mobility in minerals but this technique is still in development stages with respect to its widespread application in other geoscience domains (Reddy et al., 2020). The earliest reported applications of APT in geoscience were the characterizations of a meteoritic alloy by Miller & Russell (1992) and a metamorphosed magnetite by Kuhlman et al. (2001). There are several complimentary microscopy techniques such as SEM, EDS, TEM, STEM, electron backscatter diffraction (EBSD) and SEM-based time-of-flight secondary ion mass spectrometry (TOF-SIMS), which provide chemical data on a larger scale and thus can be used to identify regions of interest for APT analysis (Saxey et al., 2018; Reddy et al., 2020).

Depending on the type of material, the spatial resolution of TEM is similar or lower than that of APT. TEM can be a useful complementary technique to APT as it allows phase identification and a better resolution of textural relations between phases. Analytical studies using TEM and APT are commonly conducted on either the same extracted specimen or specimens extracted from areas in close proximity to each other (Bonef et al., 2015; Grenier et al., 2015; Weber et al., 2016; Rout et al., 2017). For example, Seydoux-Guillaume et al. (2019) highlighted the significance of the TEM-APT combination in geochronology and demonstrated for the first time that this approach can open new ways for nano-geochronology, allowing the identification of processes that are undetectable with conventional dating methods. Additionally, Montalvo et al. (2019) studied a zircon ($ZrSiO_4$)–reidite ($ZrSiO_4$) interface and low angle boundary within reidite using the combination of TEM and APT to identify enrichments of trace elements at the sub-nanometer scale.

The combination of APT and TEM has, to our knowledge, never been applied to understand complex chemical and mineralogical processes in soils at the nanoscale. The latter processes are commonly investigated with bulk analytical techniques such as synchrotron based-techniques and sequential extractions or with micro- to nano-analytical techniques such as TEM and STEM (Knight & Henderson, 2006; Lanteigne et al., 2012; Mantha et al., 2012; Lanteigne et al., 2014). Hence, this study will use for the first time the combination of TEM and APT to explore the occurrence of minerals and atomic clusters in porous organic material (OM) from smelter-contaminated surficial soils in Rouyn-Noranda, Quebec, Canada. The study will specifically focus on the occurrence of Cu-bearing minerals and clusters and their associations with Fe-(hydr)oxides and clay minerals in OM to better understand the sequestration of Cu in surficial soil environments.

3.1.1. A short overview of Atom Probe Tomography

APT also known as atom probe microscopy is a destructive analytical technique that is capable to position and identify almost every atom in a specimen. APT data acquisition utilizes time-of-flight mass spectrometry to generate a large dataset comprising information about several million individual atoms in a 3D spatial coordinate system (Reddy et al., 2020).

APT systems utilize the application of either ultra-fast voltage or laser pulses to erode the atoms located at the tip of a needle-shaped specimen and convert them into charged ions by a process known as field evaporation. An electric field accelerates these ions towards a position-

sensitive detector that registers the time of flight and impact position of each individual ion (Reddy et al., 2020).

The energy applied to the surface of a specimen is already known and can be used to calculate each ion's mass-to-charge ratio based on its travel time, which is in most cases sufficient for the identification of each individual atom. Impact positions on the position-sensitive-detector plot the locations of individual atoms. The locations and identity of individual atoms can be used to calculate a 3D plot that has both the chemical composition and atomic structure of the specimen and can serve as a powerful tool to examine interfaces between different regions (Saxey et al., 2018; Reddy et al., 2020). Chemical and mineralogical processes along the interfaces often result in the formation of NP as they provide pore spaces and saturated interfacial pore solution, required for NP formation (Jadoon & Schindler, 2021). The characterization of environmental interfaces with APT may thus provide insights into the underlying mechanisms for the formation of NP in the environment.

3.1.2. Incidental nanoparticles in the environment

Anthropogenic processes such as mining, smelting and wastewater treatment facilities often produce metal(loid)-bearing incidental NP (INP). INP in contrast to engineered NP are not purposely manufactured to be at the nanoscale but form directly or indirectly through anthropogenic activities (Johnson et al., 2014). INP can sequester metal(loid)s via processes such as absorption and adsorption but can also play an important role in the transportation of metal(loid)s over greater distances via Aeolian, alluvia and fluvial processes (Chopin & Alloway, 2007; Plathe et al., 2010; Yang et al., 2015). Therefore, the study of processes governing the formation, mobilization and sequestration of INP provide insights into the fate of contaminants in various environmental compartments. Formation, sequestration and mobilization of INP within porous organic matter (OM) may have a great impact on their transport in water and soil environments (Mantha et al., 2019). The role of OM in the sequestration of metal(loid)s as secondary INP and the factors which control these sequestration mechanisms are often overlooked. This paper will show that the structural, chemical and mineralogical complexity of pore spaces in soil organic matrices result in various physical, chemical and mineralogical processes, which promote the formation of INP. The formation of INP in contaminated soils is primarily linked to the type and weathering of particulate matter (PM) emitted by anthropogenic sources such as smelters and mining activities and the availability of porous phases such as OM. However, the

mechanisms that control the sequestration of metal(loid)s and formation of INP within OM in these mining-, smelter-impacted soils are not well understood.

3.1.3. Smelter-impacted soils

The majority of studies on the fate and deposition of particulate matter (PM) around smelter complexes mainly focused on the bio-availability and spatial distribution of metal(loid)s in various components of the environment (Lanteigne et al., 2012; Lanteigne et al., 2014; Ettler, 2016). Although these studies are important, they often do not characterize the chemical and mineralogical composition of the PM or do not address its role in the formation of secondary mineralogical phases in soils. In organic-rich soils, heavy metal(loid)s such as Cd, Cu and Zn sorb effectively to OM and this mode of sequestration controls often their transport, cycling and thus fate in surficial soil environments (Lair et al., 2007; Palansooriya et al., 2020). Humic substances (HS) such as fulvic acids (FA) and humic acids (HA) are metal(loid)-complexing organic substances, which form during the decomposition of OM. The extent of metal(loid) complexation by HS depends on the nature/origin of HS and physico-chemical conditions such as pH and ionic strength (Alloway, 2012; Pham et al., 2012).

3.1.4. The fate of Cu in organic-rich soils

Classical sequential-extraction studies suggest that Cu dominantly sorbs to OM in surficial soil layers (Thomasi et al., 2015). Sorption of Cu and other metal(loid)s on OM commonly depends on the total surface area and chemical and mineralogical composition of OM and associated phases (minerals, amorphous material) (Adamo et al., 1996; Gustafsson et al., 2003; Neagoe et al., 2012). In this regard, synchrotron-based studies have not provided a clear picture on the speciation of Cu in surficial soil environments containing both inorganic and organic phases (Li et al., 2006; Strawn & Baker, 2007); i.e. synchrotron-based spectroscopic studies such as extended X-ray Absorption Fluorescence (EXAF) studies cannot always resolve differences in the bonding structure of adsorption complexes involving Cu and surface sites of either OM and Fe-(hydr)oxides. Therefore, sequestration mechanisms of Cu by OM in the surficial (oxic) environment and the factors that influence them are still uncertain. Similarly, the effects of OM complexation on the stability of Fe(II)- and Fe(III) in organic-rich soils are not well understood (Bhattacharyya et al., 2018; Kügler et al., 2019). For example, Steinmann & Shotyk (1995) propose that Fe(III) is relatively more stable due to complexation with OM, whereas Bhattacharyya et al. (2018) argue that both Fe(II) and Fe(III) can coexist in organic rich soil environments.

3.1.5. Cu-bearing nanoparticles in soils

Cu-bearing NP are extensively studied and commonly exist in anoxic environments such as anaerobic wetlands, flooded soils and within interlayer spaces of Fe^{2+}-bearing clay minerals (Ilton & Veblen, 1988;1993; Ahn et al., 1997; Gammons & Frandsen, 2001; Weber et al., 2009; Hofacker et al., 2013). Hoffmann et al. (2020) explored the growth, stability and dissolution of Cu-sulfide NP under both anoxic and oxic conditions. Their study showed that these NP can remain stable for at least 22 days when their environment is changed from anoxic to oxic. Mantha et al. (2019) explored the sequestration of Cu in OM particles through the study of focused ion beam (FIB) sections with transmission electron microscopy (TEM). The authors showed that Cu is sequestered as metallic Cu and covellite, CuS_x INP within the pore spaces. The authors proposed that the INP formed through the diffusion of Cu- and S- bearing species into the interior of the OM and the reduction of these species resulted in the formation of metallic Cu and Cu-sulfide phases within OM. Jadoon & Schindler (2021) characterized the sequestration of metal(loid)-bearing NP within organic colloids in surficial soils and showed that secondary Cu-sulfide (CuS_x) NP are often associated with other inorganic phases such as Fe-(hydr)oxide and amorphous silica. The authors proposed that the nucleation of CuS_x NP was favored by reactive surface sites and available pore spaces around the Fe-(hydr)oxide and silica inclusions within the OM matrix.

The formation of NP in a porous material is controlled among many factors by the size of a pore. The pore size is related to the saturation required of a phase via Ostwald–Freundlich equation (1) (Hiemstra, 2015), where S_d is the required superstation to stabilize a nucleus, S_0 is the supersaturation in bulk solution, V_m is the molar volume, γ is the interfacial tension, R is the gas constant, r is the radius of nuclei and T is the absolute temperature.

$$S_d = S_0 \exp \frac{2V_m\gamma}{RTr} \qquad (1)$$

Equation (1) indicates that small pore spaces require a higher degree of saturation for nucleation to occur relative to the bulk solution as indicated by PCS. In this regard, the above-mentioned studies did not fully address the effects of PCS and the role of other elements and mineral phases on the formation of Cu-bearing NP.

3.1.6. Objectives

Hochella et al. (2019) proposed that the nanoparticle cycle involves three compartments: (I) bulk size Earth material such as minerals and rocks, (II) precursors such as atoms, ionic species and clusters formed during weathering of the bulk Earth materials, and (III) nanoparticles formed either through weathering of the bulk Earth material or through precipitation of the precursors. The combination of APT and TEM allows now to investigate the occurrence of both precursors and nanoparticles, in organic porous matrices. These studies shed light on the formation and stability of Cu-, Fe-, and Zn-bearing secondary phases within porous OM matrices and on the role of porosity and the presence of inorganic phases on the sequestration of Cu. Hence, the objectives of this study are to examine whether

(a) PCS controls nucleation of phases within pore spaces of OM;
(b) Precursors of nanoparticles exist within OM;
(c) Concentration gradients of Cu can be used to identify potential diffusion pathways of Cu within OM;

In this study, the term *organic matter* (OM) is used for HS that are mainly formed during the decomposition of organic material. The term *dissolved organic matter* (DOM) is used to describe carbon-based aqueous species and the terms *nanoparticle* (NP) and *incidental nanoparticle* (INP) represent particles that have a diameter of <100 nm.

3.1.7. Background information on smelter-impacted soils and study area

The deposition of PM in mining impacted soils is a global concern. The deposition of metal(loid) bearing PM increases the concentration levels of metal(loid)s in the surficial layers of soils (Schindler & Hochella, 2017). The weathering of PM is controlled by both soil environmental/matrix conditions and composition of PM and results in the release of metal(loid)s and their subsequent sequestration by solid and colloidal phases composed of OM and minerals (Ettler, 2016). Studies assessing the environmental fate of PM in mining/smelter impacted soils cannot always explain the observed moieties of metal(loid) species in soils. In this regard, Lanteigne et al. (2012) and Schindler et al. (2016) showed that the higher mobility of Cu vs Ni in soils around the smelter complexes in Sudbury is a result of the higher solubility of Cu- versus Ni-mineral phases occurring in the micrometer-sized fraction of the smelter emissions.

The area of this study extends around the city limits of Rouyn-Noranda, Quebec. It surrounds the Horne smelter, which is considered a critical emission source of PM contaminated

with heavy metal(loid)s. The ore processed at the Horne smelter included minerals like sphalerite, pyrite, galena, pyrrhotite, chalcopyrite and magnetite, as well as native silver and gold (Kerr & Gibson, 1993) with pyrite, pyrrhotite, chalcopyrite and magnetite comprising up to 85% of the mass (Denis, 1933). PM emissions from the Horne smelter occurred for over a century (Kettles & Bonham-Carter, 2002). Since 1976, the smelter predominantly processes electronic waste containing base metal(loid)s such as Cu.

Studies on the environmental impact of smelting activities in Rouyn Noranda focused on the concentrations and speciation of metal(loid)s in lakes, soils, rock coatings, snow samples and biota (Bonham-Carter et al., 2006; Knight & Henderson, 2006; Telmer et al., 2006; Zdanowicz et al., 2006; Masson et al., 2010; Dinis et al., 2020). Knight & Henderson (2006) classified PM in the surficial soils surrounding the smelter based on size, texture and composition and showed that rounded and spherical smelter-derived PM are the most abundant type of PM. The rounded particles are further classified into tabular (Fe and Fe+Al+Si), plated (Fe), granular (Fe+Al+Si), etched (Cu+Fe+Si), and lunar (Na+Al+Si) textures, which mostly represent slag based dust released from Cu smelting operations over the course of time. The above authors proposed that this slag based dust is very resistant to weathering and hardly contributes to the metal(loid) concentrations in humus, whereas the majority of Cu, Zn and Pb metal(loid) phases in humus represent weathered and alteration products of labile dust released from smelting operations.

3.1.8. Studying soil processes at the atomic- nano- and micrometer scale

Soil properties and processes at the nanometer scale such as erosion and cohesion affect processes at the kilometer scale such as the formation of landscapes and flooding. Atomic- and nano-scale examinations can provide greater insights into the mobility of metal(loid)s within porous matrices. For example, the observed high affinity of Cu towards OM in contaminated surficial soils is explained to some extent by TEM examinations, which show that this high affinity might be due to the diffusion of Cu species into the organic matrix and subsequent formation of metallic Cu and Cu-sulfide phases within pore spaces of OM (Mantha et al., 2019). However, atomic and nano-scale studies often face challenges to establish a statistical representation of their findings with respect to those at the bulk- (centimeter), area- (meter) and regional-scale (km). Hence, this study is not intended to encompass the representative features of the soils at Rouyn Noranda. Instead its goal is to explore sequestration mechanisms of metal(loid)s in greater detail using a tiered approach through data gathered at the bulk-, micro-, nano-, and atomic scale.

3.2. Methodology

Twenty-one surficial soil samples (upper 5 cm) were collected at seven different sites within a two-km radius of the Horne smelter in Rouyn-Noranda in the late summer of 2017. The sampling sites were selected based on the study of Knight & Henderson (2006) which characterized the regional distribution of metal(loid)s around the Horne smelter. Samples 5A, 7A-B were selected for further characterization based on their distance from the smelter and their Cu- and Zn concentrations (Tables S1 and S2). None of the surficial soil samples were collected in proximity to surficial waters (at least 50 m from a shoreline lake, river bank or wetland) and thus were most likely only water-saturated during the spring thaw. The chemical and mineralogical compositions of the soil samples were characterized with ICP-MS for Ag, Co, Cu, Pb, Sb, Sn and Zn, C-N-S analyzer for C, N and S (Tables 3S1, 3S2, 3S3, 3S4 and 3S5) and X-ray powder diffraction for mineral phases, respectively (Figure 3-S2).

Nano-scale processes within OM may be studied using combinations of the FIB technology with TEM and APT as the former technology allows a site-specific extraction of samples from the OM. Polished epoxy pucks with soils from the samples 5A and 7A-B were embedded into epoxy and examined with SEM to characterize the chemical composition of organic material and to identify suitable locations for subsequent FIB extractions. Two FIB sections for TEM (FIB-TEM sections) and numerous FIB sections for APT (FIB-APT sections) were extracted from two distinct areas. The FIB-TEM and FIB-APT were taken from each site in close proximity to each other with the FIB-APT extracted from areas of lower porosity (Figures 3-3a and 3-3b). All FIB sections were extracted by lift-out technique (Mantha et al., 2019) with a FEI Helios 600 NanoLab FIB at the Pacific North West National Laboratory (PNNL), USA. (August, December, 2020). For quality control purposes, the FIB-APT were preliminary characterized at PNNL using a Titan 80-300 scanning transmission electron microscope (STEM). A more thorough characterization of the FIB-TEM sections was conducted with a field emission TEM FEI Talos F200x at the Manitoba Institute of Materials, University of Manitoba, Canada.

Preparation of FIB-APT consists of two main steps, (1) sample lift-out and (2) FIB milling (Figure 3-1). The lift-out involves the creation of trenches around the area of interest and the extraction of sections through a micromanipulator and their subsequent attachment to a micropost (Figure 3-1a. 3-1b, 3-1c and 3-1d). The FIB milling involves reshaping of the specimens by carving

them with a gallium ion beam to tips (Figures 3-1e, 3-1f, 3-1g). APT analysis was conducted at the Pacific North West National Laboratory (PNNL), USA on a total of three tips. APT measurements were conducted in laser mode with a UV laser (λ = 355 nm), a pulse rate of 100-200 kHz and a pulse energy range of 5-25 pj.

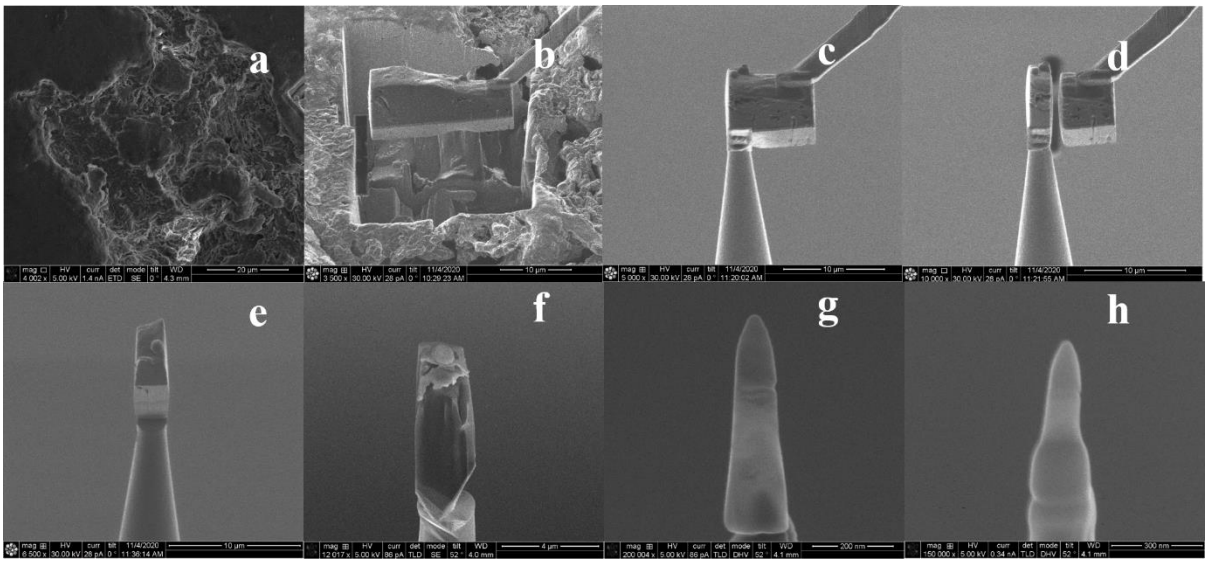

Figure 3-1: **FIB-based preparation of APT specimens samples.** (a) SEM image in secondary electron mode of a region from a polished epoxy puck selected for APT-FIB-extraction; (b)-(h) Sequence of steps in the APT sample (b) trenching of a lamellar wedge with a protective Pt cap and respective lift-out; (c-d) Attachment of the extracted lift-out to a Si micropost. (e-h) Reshaping of the sample through ion milling. (g) Final morphology of the tip with a diameter of 100 nm. (h) Same tip as shown in (g) but after APT analysis.

The data was processed using the IVAS v3.6.18 software package. The mass spectra of all APT datasets are very complex due to the presence of complex metal(loid)-bearing species with different charge states (Figures 3-S3 and 3-S4). Hence, the quantification of metal(loid)s at the atomic level through APT is not straightforward and requires interpolation of data. Some atomic species are represented by multiple peaks or by peaks corresponding to complex-ions. As a result, peaks corresponding to species of different atomic identities and charge-to-mass ratios overlap. For example, Fe and Si produce several overlapping peaks in the mass to charge ratio vs counts

spectrum. Hence, only characteristic peaks for both Fe (46 Da) and Si (30 Da) were used to generate distribution plots for both elements as otherwise differences in their locations in the 3D space could not be resolved. The identified locations of atomic species in the 3D space are shown in this study in the form of 2D spatial maps representing their density (ions per nm^3). However, the bonding between different atoms is resolved in 3D and the parameters (bond lengths and ionic sizes) were calculated using the ionic radii of Shannon (1976).

Technical details for each type of analysis and the methodology for the mineral identification are provided in the materials and methods section in the Appendix B (Supplementary information).

3.3. Results

We will first address the bulk chemistry and mineralogy of the collected samples before reporting our observations at the nanometer and atomic scale.

3.3.1. Bulk Chemistry and Mineralogy

Only samples selected for further examination with SEM, TEM and APT are described here in detail. Sample 5A is an organic, black, fibric and mineral-rich layer with litter on top, and has color code 10YR [2/1] (dry) and pH of 4.74 (Figure 3-S1). Sample 7A is composed of a brown thin litter of fibric mineral layer over a light reddish-brown organic layer, and has color code 7.5YR [4/2] (dry) and pH of 4.39 (Figure 3-S1). Sample 7B mostly represents black humus, has a color code 5YR [2.5/1] (dry) and pH of 3.84 (Figure S1). All these samples contain Cu, Zn and Pb concentrations above the average of all collected samples (Tables 3-S1 and 3-S2). All samples contain high amounts of OM (total C $\geq$ 22%, Table 3-S1 and 3-S3) and contain the major phases albite ($NaAlSi_3O_8$) and quartz (SiO_2), with traces of with traces of magnesioferrite ($MgFe_2O_4$), protoenstatite ($Mg_2Si_2O_6$), magnetite (Fe_3O_4) and clinochlore $Mg_5Al(AlSi_3O_{10})(OH)_8$ (Figure 3-S2).

3.3.2. Size and chemical composition of organic particles

OM particles are mainly in the fine to coarse sand size fraction (>180 μm) and contain Fe-, Cu-, Zn- and Si-bearing phases within their porous matrix and on their surfaces. Some of these phases are euhedral to subhedral detrital particles. Some particles show sharp interfaces towards OM, whereas others form diffuse interfaces with metal(loid)-rich OM (Figure 3-2). Fe-bearing particles are the most abundant inorganic-based particles in larger OM particles (in blue in Figure

3-2). Copper occurs either finely distributed within the matrix of OM particles or in Fe-oxide particles (Figures 3-2b and 3-2f). TEM-FIB-1 and APT-FIB-1 were extracted from an interface of OM towards a lenticular Cu-Fe-bearing particle (50 x 10 μm) with a Cu and Fe elemental ratio of 1 : 2 (Figure 3-3b). Furthermore, one OM particle (350 x 50 μm) contains SiO_2 and silicate phases throughout its matrix. TEM-FIB-2 and APT-FIB-2 were extracted from an area in an OM particle (average diameter = 100 μm) which is in close proximity to metal(loid)-rich particles containing As, Cu+ Fe+ Zn and Sn+Sb in a 3 : 2 : 1 ratio (Figure 3-3c).

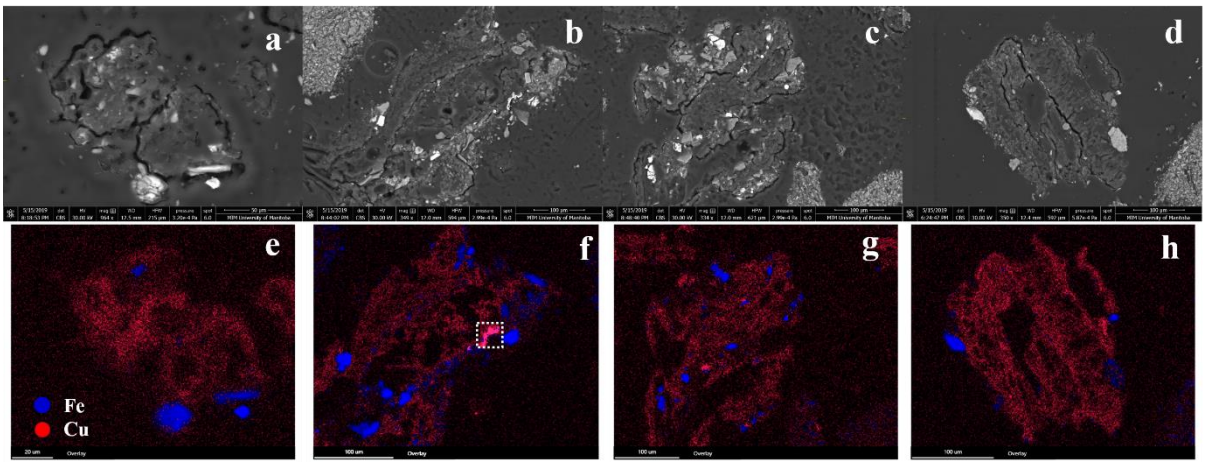

Figure 3-2: (a-d) SEM images in backscattering electron mode (BSE) of organic particles from sample 5A and (e)-(h) their corresponding SEM-EDS chemical distribution maps for Fe (blue) and Si (red). The maps indicate that Cu is homogenously distributed within the OM particles, whereas Fe is concentrated within certain regions; white dashed square in (f) indicates one of the two regions selected for TEM-FIB and APT-FIB-extraction.

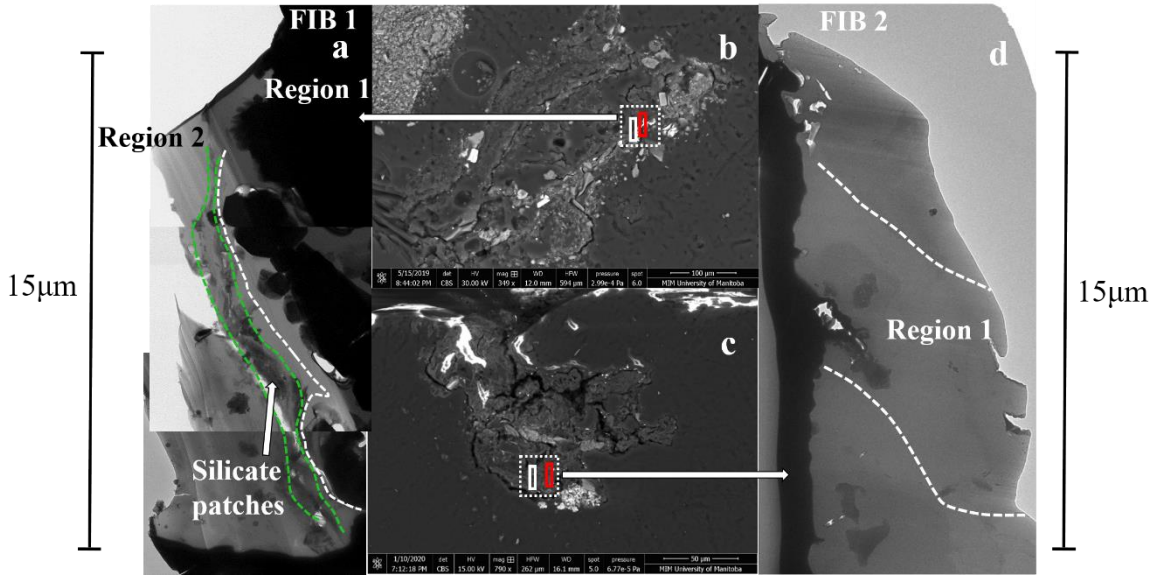

Figure 3-3: (a) and (d) TEM images of the TEM-FIB-1 and TEM-FIB-2 FIBs that were extracted from the areas (marked with white solid line within white dashed line boxes) indicated in (b) and (c); (b)-(c) SEM images in BSE mode of the two residues; the locations from which the TEM-FIBs and APT-FIBs were extracted are labelled with white and red rectangles, respectively, inside a box indicated with dashed white lines. (a), (d) TEM-FIB-1 and TEM-FIB-2 are divided into regions 1 and 2 on the basis of particle size distributions (marked with white dashed lines) and mineralogical composition. The occurrences of silicate patches in TEM-FIB-1 are marked with green dashed lines.

3.3.3. Mineralogical and chemical composition of the TEM-FIB sections

On the basis of the size distribution of particles, TEM-FIB-1 can be divided into two distinct regions: In region 1 occur larger euhedral cuprospinel particles (average width = 200 µm) within OM. Region II contains smaller metal(loid)-bearing particles (< 100 nm), which occur in a network of amorphous silicate patches or channels; this network has an average width of 1 µm and stretches along the entire length of the FIB section (Figure 3-3). The channels can have variable amounts of Al and Cu (up to 12 wt% Cu; Figures 3-3, 3-4, 3-5, 3-6, 3-7, 3-8, 3-9, 3-10 and 3-11). For example, amorphous silicate patches with average diameters of circa 70 nm occur along the outer edges of larger cuprospinel particles (Figure 3-4) and form sharp (Figure 3-4a, 3-4b and 3-4c) and diffused (Figure 3-4c, 3-4d and 3-4f) interfaces towards the latter.

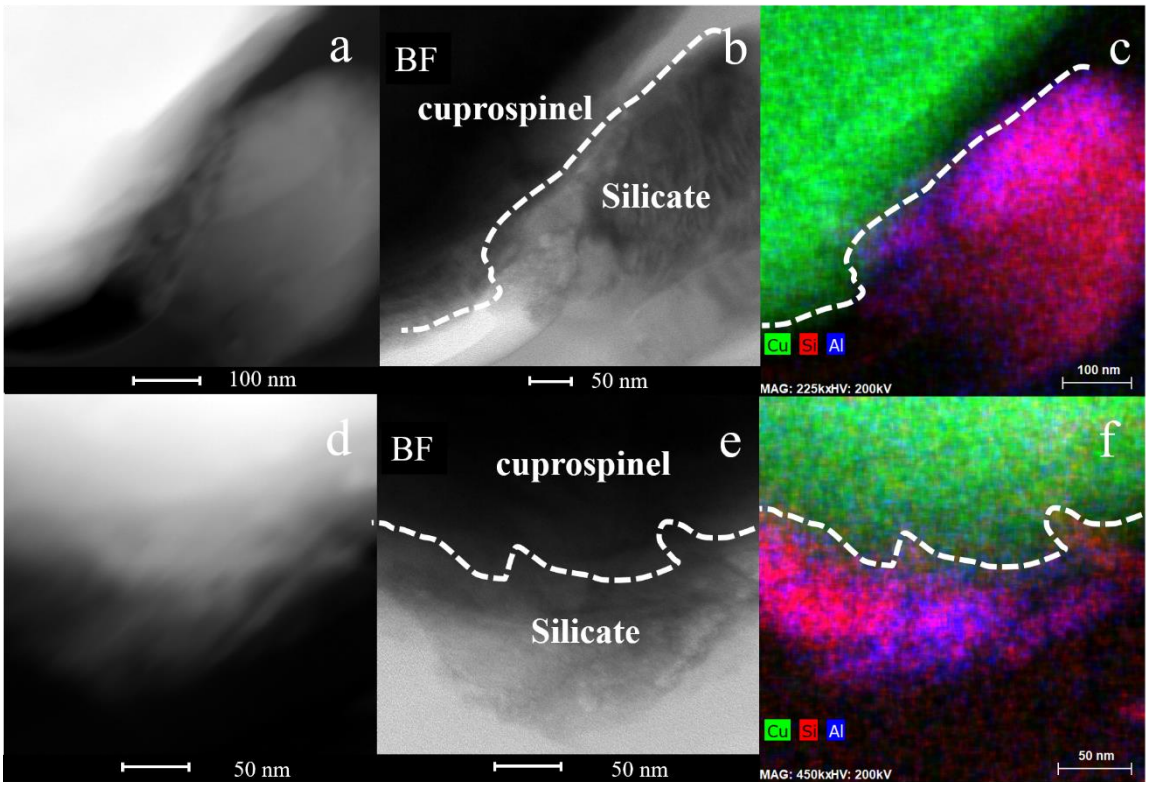

Figure 3-4: Sharp and diffused OM-silicate interfaces in TEM-FIB-1: (a) STEM image, (b) high-resolution TEM image and (c) STEM-EDS chemical map for (b) showing the distribution of Cu (green), Si (red) and Al (blue) and indicating a cuprospinel NP embedded within an OM matrix forming a sharp interface with a silicate phase (outlined with white dashed line in (b) and (c)). (d) STEM image, (e) high-resolution TEM image and (f) STEM-EDS chemical map for (c) showing the distribution of Cu (green), Si (red) and Al (blue) and indicating a cuprospinel NP embedded within an OM matrix forming a diffused interface with a silicate phase (outlined with white dashed line in (e) and (f)).

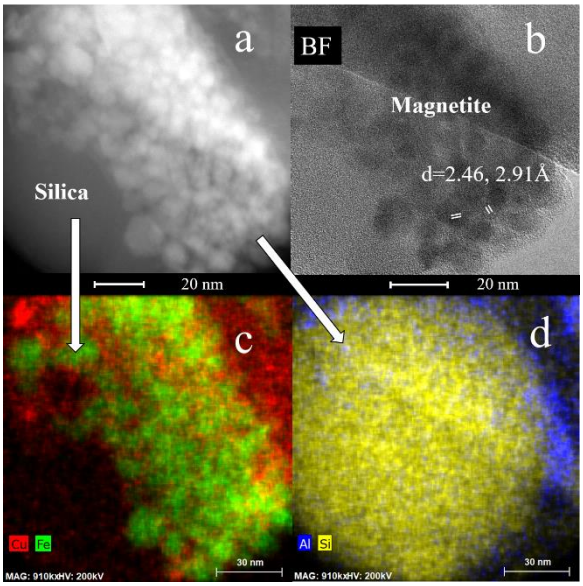

Figure 3-5: Magnetite (spinel phase) within the OM matrix of TEM-FIB-1: (a) STEM image; (b) high-resolution TEM image indicating lattice fringes with d = 2.46 Å and 2.91 Å; (c)-(d) STEM-EDS chemical distribution maps for (c) Cu (red), Fe (green) and (d) Al (blue) and Si (yellow) indicating magnetite NP aggregate within a SiO_2 patch, which is embedded in the OM matrix and contains heterogeneously distributed Al and Cu.

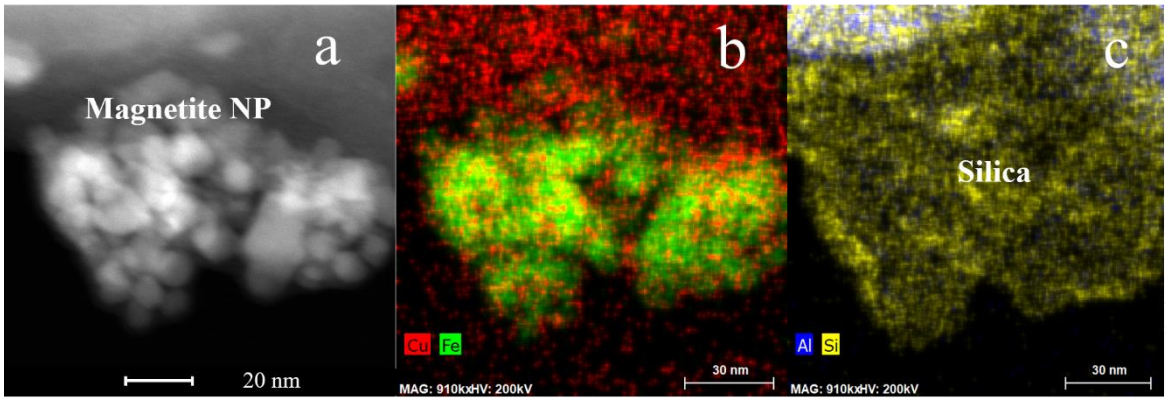

Figure 3-6: Magnetite (spinel phase) within the OM matrix of TEM-FIB-1: (a) STEM image, (b) high-resolution TEM image of lattice fringes with d = 2.46 Å and 2.91 Å and (c-d) STEM-EDS chemical distribution map for (b) Cu (red), Fe (green) and (c) Al (blue) and Si (yellow) indicating magnetite NP aggregate within a SiO_x patch (indicated in yellow in c) that is embedded in the OM matrix and contains heterogeneously distributed Al and Cu.

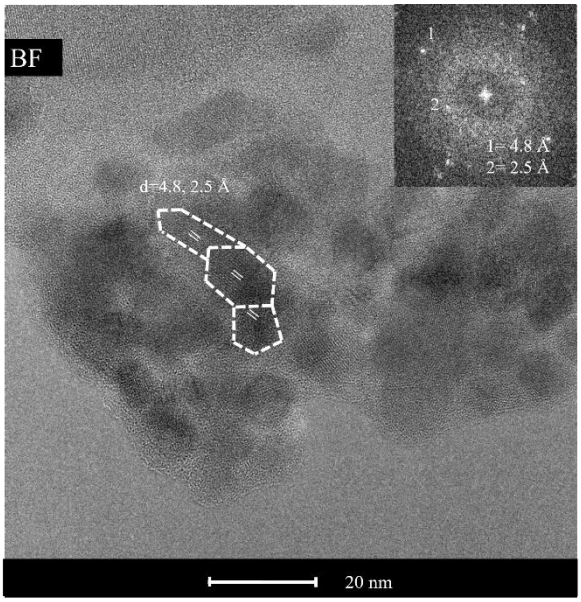

Figure 3-7: High-resolution TEM image of lattice fringes with *d* = 4.8 Å and 2.5 Å indicating individual and aggregated magnetite NP shown in Figure 3-6. The magnetite NP show oriented attachment with one another within SiO_2 matrix (highlighted with white dashed lines).

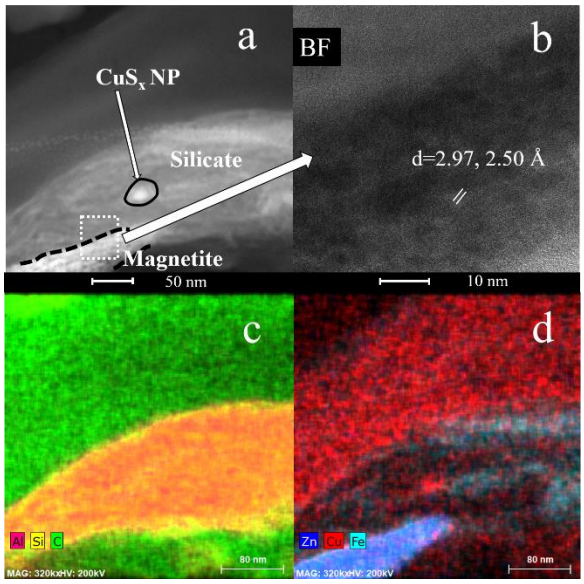

Figure 3-8: Magnetite (spinel phase) within the OM matrix of TEM-FIB-1: (a) STEM image, (b) high-resolution TEM image of lattice fringes with *d* = 2.97 Å and 2.50 Å; (c)-(d) STEM-EDS chemical distribution map for (c) Al (pink), Si (yellow) and C (green) and (d) Zn (blue), Cu (red) and Fe (turquoise) indicating the occurrence of Cu-bearing magnetite attached to a silicate phase; the interfaces between magnetite, silicate and OM are sharp at the nanometer scale (highlighted in black dashed lines in (a)). CuS_x NP occur individually (highlighted in black solid line in (a)) in the silicate phases but could not be unequivocally identified.

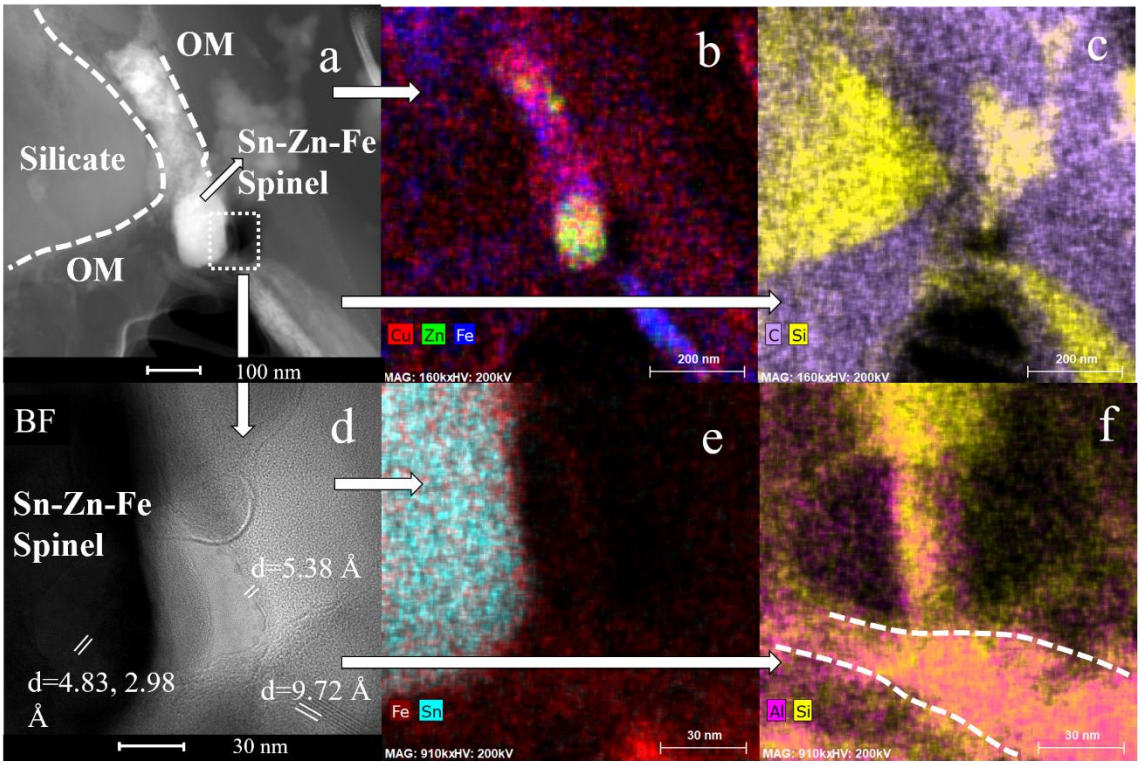

Figure 3-9: Sn-, Zn-, Fe-bearing spinel phase (with heterogeneously distributed Cu) showing sharp and diffused interfaces towards OM and silicate phases in TEM-FIB-1: (a) STEM image and (b)-(c) STEM-EDS chemical distribution maps for (b) Cu (red), Zn (green) and Fe (blue) and (c) C (purple) and Si (yellow) indicating nucleation of Sn-bearing spinel phase within OM matrix and in close proximity to silicate phases; OM-spinel and silicate-spinel interfaces are highlighted in white dashed lines in (a). (d) High-resolution TEM image indicating lattice fringes (highlighted in solid white line) with d = 4.83, 1.59, 5.38 and 9.72 Å and (e)-(f) STEM-EDS chemical distribution map for (e) Fe (brown) and Sn (turquoise) and (b) Al (pink) and Si (yellow) indicating an Al-Si-rich pore channel connecting the spinel NP with a silicate phase.

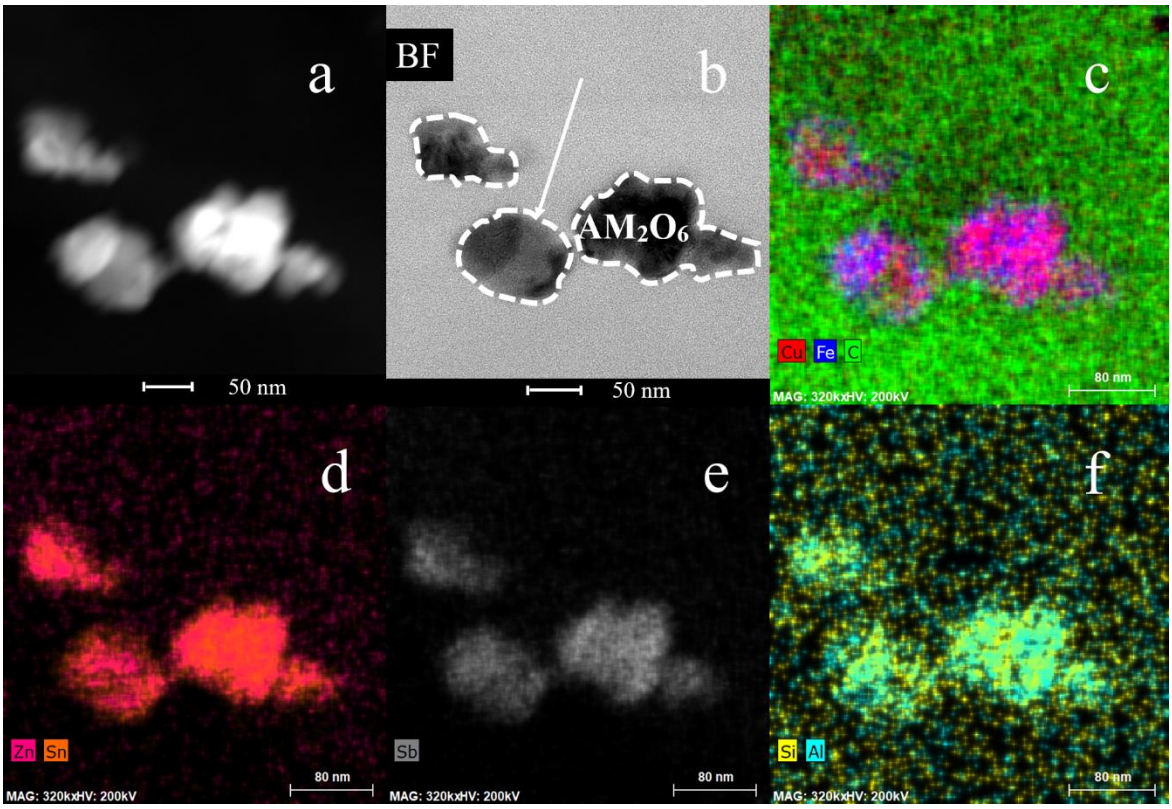

Figure 3-10: OM-spinel interrelations: (a) STEM image, (b) high-resolution TEM image (note sharp interfaces marked by dashed lines) and (c) STEM-EDS chemical distribution map for (c) Cu (red), Fe (blue), C (green) and (d) Zn (pink), Sn (orange) and (e) Sb (gray) and (f) Si (yellow) and Al (turquoise) indicating the occurrence of a Si-Al-rich AM_2O_6 (*A* = Cu, Fe and *M* = Sn, Sb) phase embedded in OM.

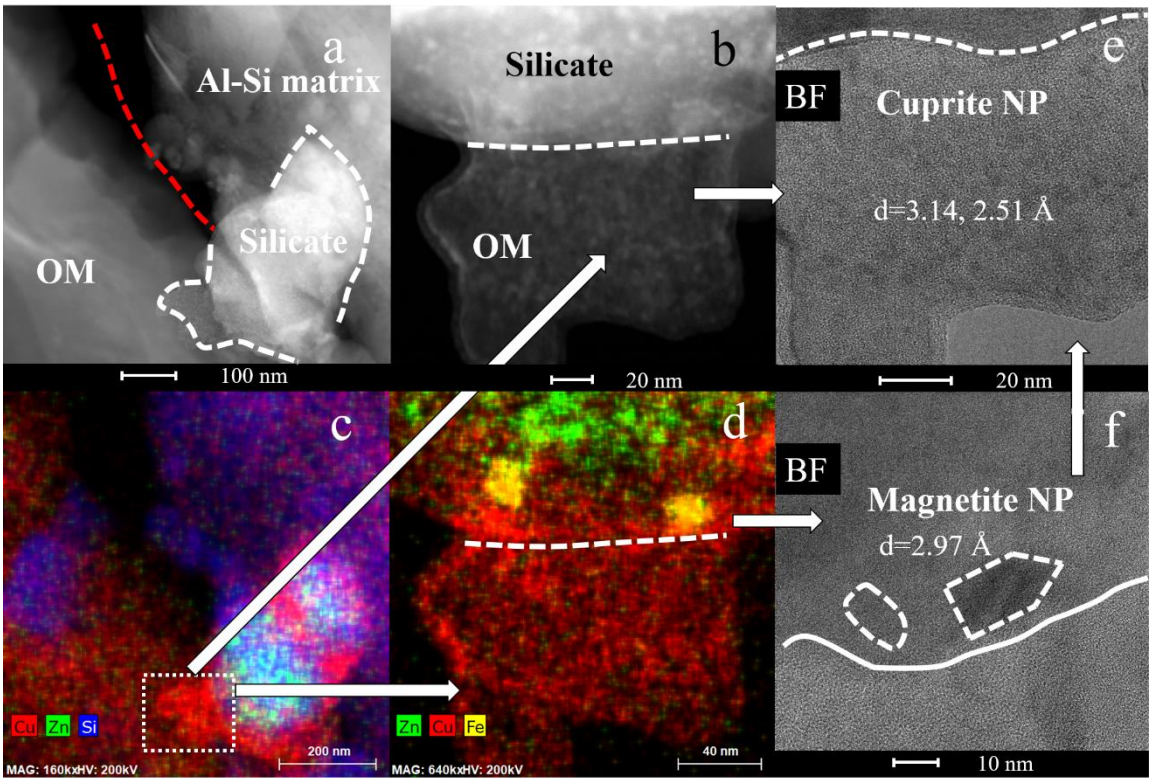

Figure 3-11: Silicate phase rich in Zn NP in association with aggregates of cuprite and magnetite NP in TEM-FIB-1: (a) and (b) STEM images, (c)-(d) STEM-EDS chemical distribution maps for (c) Cu (red), Zn (green) and Si (blue) and (d) Zn (green), Cu (red) and Fe (yellow); (e)-(f) high-resolution TEM images of lattice fringes with d = 3.14 Å, 2.51 Å and 2.97 Å; interfaces between OM, Al-Si matrix, a silicate phase (rich in Zn), cuprite and magnetite NP are indicated with red and white dashed lines.

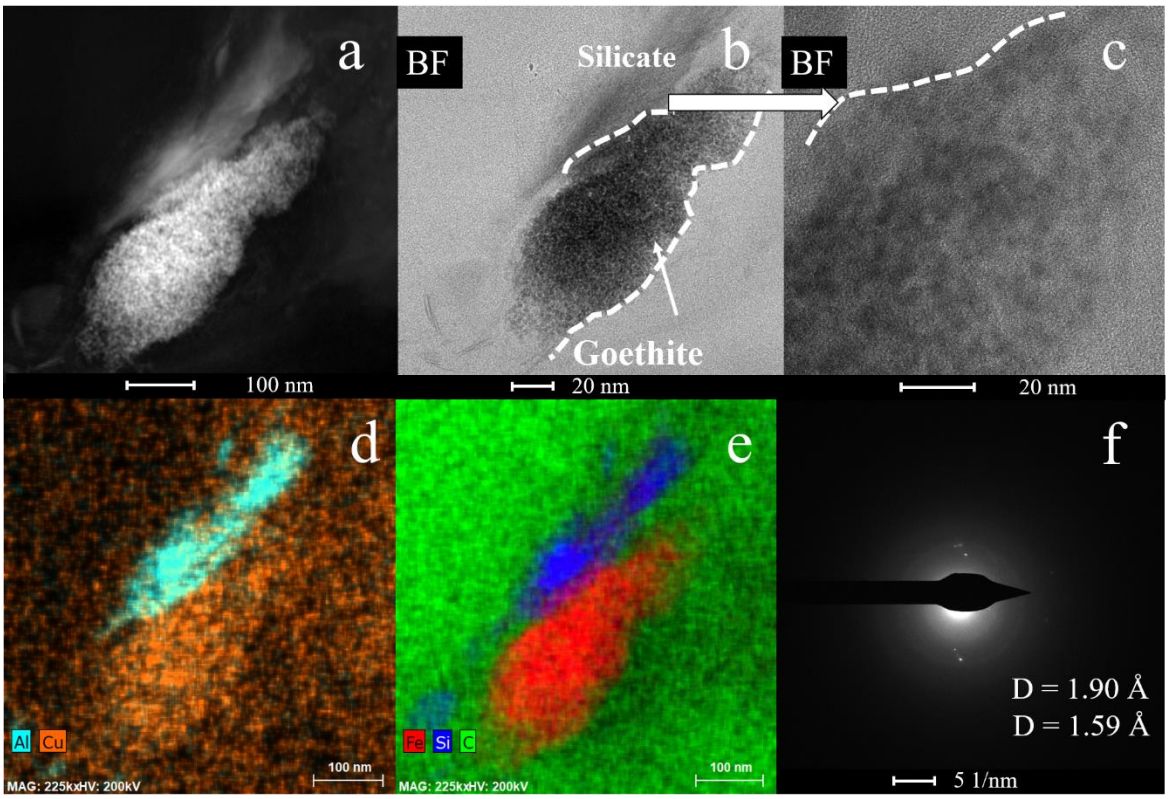

Figure 3-12: Fe-(hydr)oxide (FeO_x) and silicate interfaces within the OM matrix of in TEM-FIB-2: (a) STEM image, (b)-(c) high-resolution TEM images and (d)-(e) STEM-EDS chemical distribution maps for (d) Al (blue) and Cu (orange) and (e) Fe (red), Si (blue) and C (green) indicating a FeO_x aggregate and an illite phase within OM showing a diffused interface between FeO_x-Clay and FeO_x-OM (highlighted in white dashed lines); f) SAED pattern indicating peaks at d = 1.9 Å and 1.6 Å which suggest the occurrence of goethite.

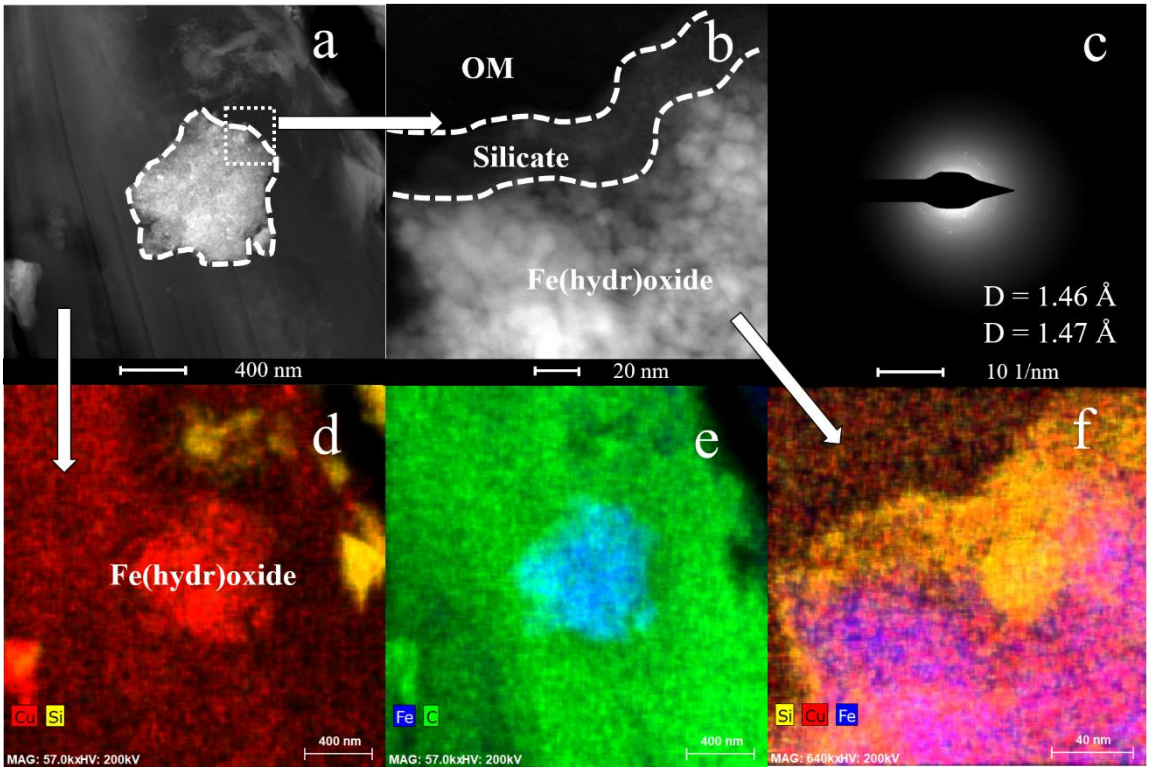

Figure 3-13: Silver NP and Si- and Cu-rich pore channels surrounding a FeO_x aggregate within the OM matrix of TEM-FIB-1: (a)-(b) STEM images, (b) high-resolution TEM image indicating lattice fringes (highlighted in solid white line) with d = 2.5 and 1.43 Å and (d)-(f) STEM-EDS chemical distribution map for (d) Si (blue), Cu (red) and Fe (yellow) and (e) Cu (red), C (green) and Si (blue) and (f) Fe (yellow) indicating the presence of ferrihydrite; The outlines of the Ag nanoparticles sharp and diffused interfaces between FeO_x-OM and FeO_x-silicate are highlighted with white solid and dashed lines in (a)-(c) and (e), respectively.

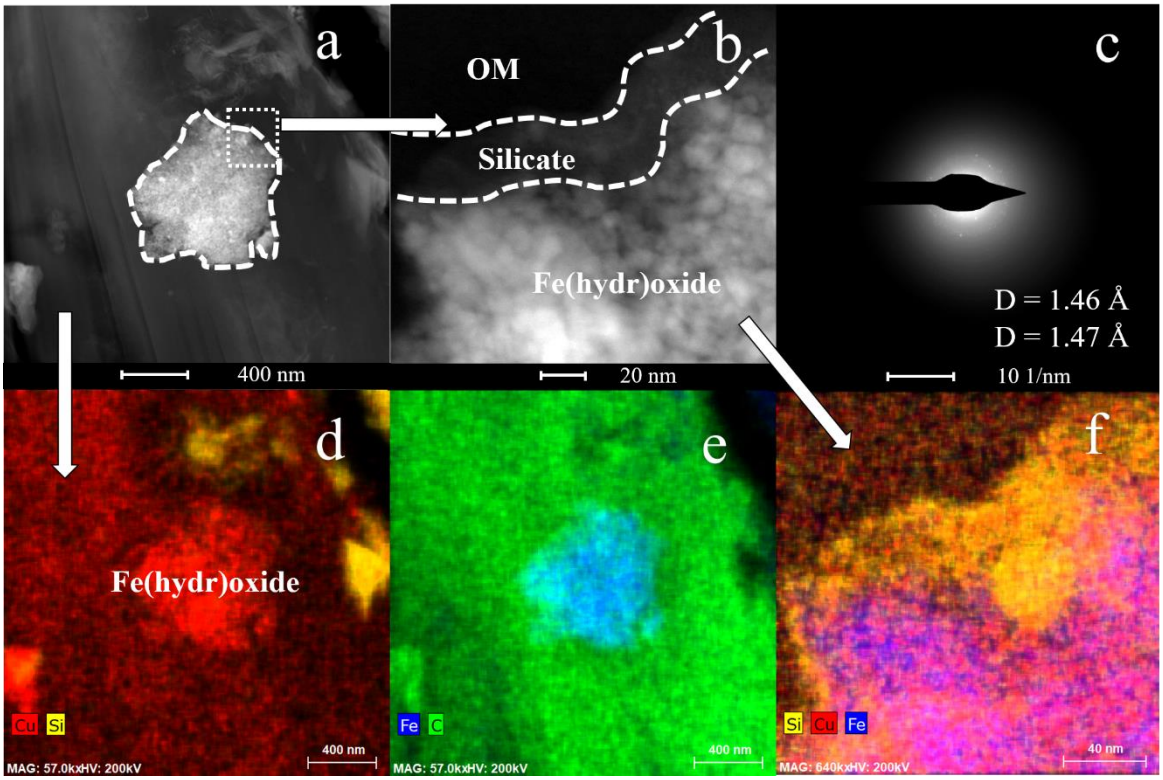

Figure 3-14: FeO_x phase with silicate rim in the OM matrix of TEM-FIB-1: (a)-(b) STEM images, (c) SAED pattern indicating d-spacing of 1.46 Å and (d)-(f) STEM-EDS chemical distribution map for (d) Cu (red), Si (yellow) and (e) Fe (blue) and C (green) and (f) Si (yellow), Cu (red) and Fe (blue) indicating a ferrihydrite (Fh) phase within OM matrix. Silicate phases form a rim (30 nm width) around Fh aggregate in some regions (highlighted in white dashed lines in (b)), whereas the whole Fh aggregate forms a diffused interface towards OM (highlighted in white dashed lines in (a)).

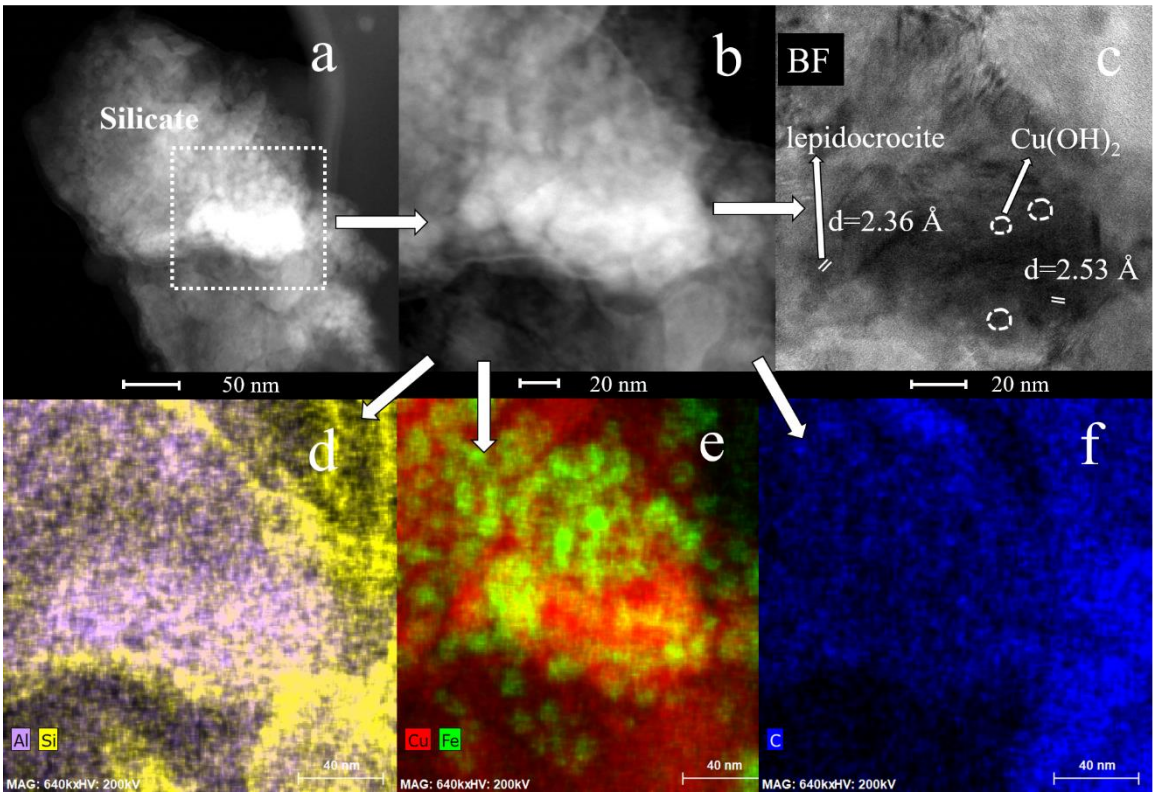

Figure 3-15: Aggregation of FeO_x NP (most likely lepidocrocite) and $Cu(OH)_2$ NP within an amorphous silicate matrix that is embedded in the OM matrix of TEM-FIB-1: (a)-(b) STEM images, (c) high-resolution TEM image indicating lattice fringes with d = 2.36 and 2.53 Å and (d)-(f) STEM-EDS chemical distribution map for (d) Al (purple), Si (yellow) and (e) Cu (red) and Fe (green) and (f) C (green) indicating the occurrence of larger FeO_x NP (most likely lepidocrocite) (average NP size = 10 nm) and smaller $Cu(OH)_2$ NPs (< 5 nm and highlighted in white dashed line in (c)) in an amorphous silicate matrix.

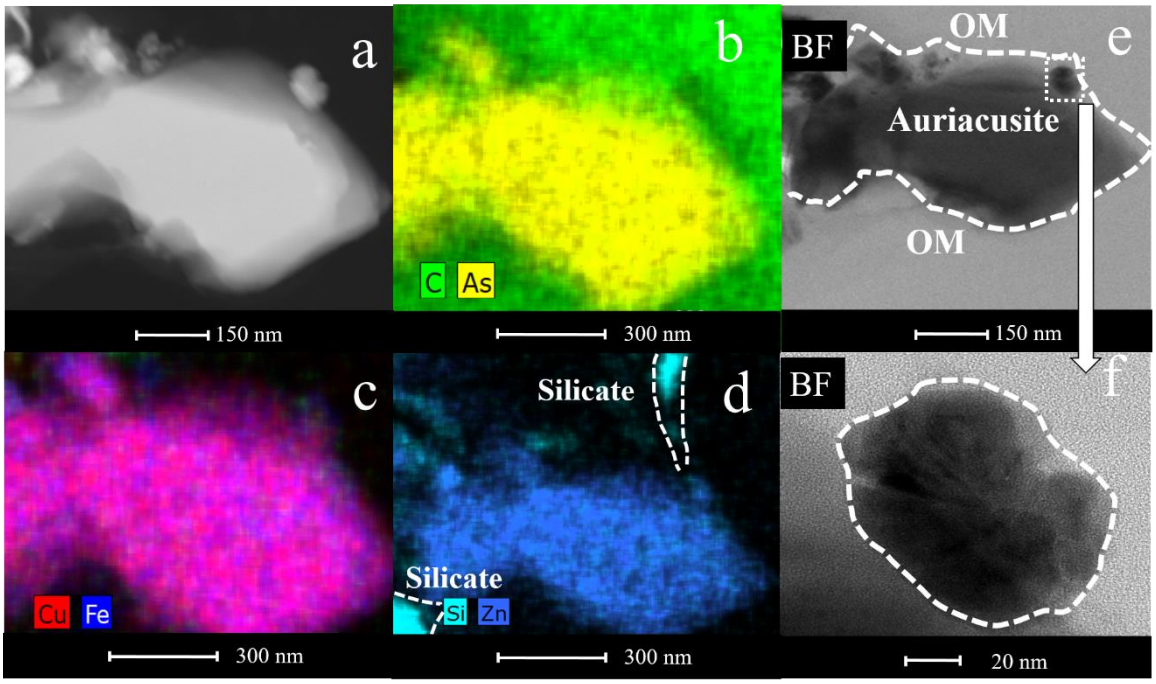

Figure 3-16: Cu-, Zn-, Fe-bearing arsenate phase in OM of TEM-FIB-2: (a) STEM image, (b)-(d) STEM-EDS chemical distribution maps for (d) Cu (red) and Fe (blue) and (e) C (green) and As (yellow) and (f) Si (turquoise) and Zn (light-blue) and (e)-(f) high-resolution TEM images indicating auriacusite precipitate embedded in the OM matrix forming a sharp interface with OM (highlighted in white dashed line in (b-c)).

TEM-FIB-2 is thicker than TEM-FIB-1 and thus nano-domains are less visible and are only identifiable in a thinner part of the former FIB section, which is termed here region 1. Here, metal(loid)-rich phases (diameter = 70-200 nm) occur in close proximity to Si- and Al-rich phases (Figure 3-3).

Only complex mineralogical features observed in regions 1 and 2 of TEM-FIB-1 and region 1 of TEM-FIB-2 are discussed below in detail. In these regions, common features of interest are the occurrence of Cu-bearing Fe-(hydr)oxide and Fe-spinel phases along various interfaces between amorphous silicates and OM (Figures 3-4, 3-5, 3-6, 3-7, 3-8, 3-9, 3-10, 3-11, 3-12, 3-13, 3-14, 3-15 and 3-16). These mineral phases are described here in their order of their abundance.

3.3.3.1. Spinels and silicates

Aggregates of subhedral to anhedral nanoparticles of spinel-type phases such as magnetite (Fe_3O_4) and ($Cu_{0.75}Zn_{0.75}Sn_{0.75}Fe_{0.67}O_4$) occur in close association with silicate patches (Figures 3-5, 3-6, 3-7, 3-8, 3-9, 3-10 and 3-11). Individual NP have diameters of circa 10 nm to 100 nm (Figures 3-5, 3-6, 3-7, 3-8, 3-9, 3-10 and 3-11). For example, magnetite NP (average diameter = 10 nm) form aggregates within the matrices of silica patches (Figures 3-5, 3-6, 3-7, 3-8, 3-9, 3-10 and 3-11). In some cases, magnetite NP attached to each other show lattice fringes in the same orientation (Figure 3-7). Copper NP are heterogeneously distributed in and around the silica patches, whereas Al can be enriched along the rims of the patches (Figures 3-6 and 3-7).

NP comprising of Cu- and Zn-bearing magnetite (Figure 3-8) and Sn-, Zn-, Fe-bearing spinel phases (average diameter 100 nm) occur also in close association with silicate phases and are usually connected to Cu-, Si/Al-rich patches or pore channels (Figure 3-9). These phases have elevated concentrations of Cu (10 wt%) and form sharp and diffused interfaces towards silicates and OM. CuS_x NP (average diameter = 25 nm) occur within Si/Al-rich patches or pore channels but they could not be unequivocally identified (Figure 3-8a). Mineral phases with a general formula of AM_2O_6 (*A*=Zn, Cu and *M*=Sn, Sb) also occur within the OM matrix. These phases form NP with average diameters of 80 nm and can contain up to 9.5 wt% Cu. They form sharp interfaces towards the OM (Figure 3-10).

3.3.3.2. Silicates and cuprite

Silicates are rich in metal(loid)s throughout both FIB-sections but nano-domains are only visible in thin regions, such as those around holes or along cracks in the FIB section. For example, a silicate phase rich in Zn-bearing NP occurs along a crack running parallel to the interface between OM and a silicate matrix (Figure 3-11a). The rim around the Zn-silicate also contains NP of cuprite (Cu_2O) (average diameter = 5 nm) (Figures 3-11b and 3-11e) and magnetite (average diameter = 20 nm) (Figure 3-11f). The cuprite NP aggregate around the edges of the rim towards the OM (Figures 3-11d and 3-11e). The OM region in close proximity to the silicate contains also cuprite NP (average diameter = 5 nm) but these NP do not form larger aggregates (Figures 3-11c and 3-11e).

3.3.3.3. Fe-(hydr)oxide and silicates

. Fe-(hydr)oxide aggregates with diameters of circa 100 to 300 nm occur within the OM matrix (Figures 3-12, 3-13, 3-14 and 3-15). These aggregates mostly comprise ferrihydrite

($Fe_{10}O_{14}(OH)_2$) NP, which occur commonly along silicate rims (30 nm thickness) (Figures 3-13 and 3-14). The silicates are composed predominantly of illite (Figures 3-13 and 3-14) with the average composition of $K_{0.5}Al_{1.03}Mg_{0.86}Fe_{0.4}[(Al_{0.5}Si_{3.5})O_{10}](OH)_2$. For example, Figure. 3-12 shows a possible goethite aggregate forming a sharp interface towards illite and OM. The goethite aggregate is enriched in Cu (6 wt%) relative to illite. The surrounding OM matrix also contains a substantial amount of Cu (3 wt%) forming a diffuse interface with both illite and the goethite aggregate (Figure 3-12). Ferrihydrite aggregates occurring in close association with patches of amorphous silicates are also connected to Cu-, Si-Al-rich patches or pore channels that contain Cu concentration up to 10 wt% (in blue in Figure 3-13). Fe-(hydr)oxide aggregates of possible lepidocrocite (γ-$Fe^{3+}O(OH)$) NP occur within an amorphous silicate patch. The lepidocrocite NPs have an average size of 10 nm, whereas smaller spertiniite NP (< 5nm) occur within and along the lepidocrocite aggregate (Figures 3-15 and 3-S6).

3.3.3.4. Arsenates

A larger precipitate of auriacusite, ($Fe_{1.0}Cu_{0.8}Zn_{0.2}(AsO_4)O$) occurs embedded in the OM matrix.(Figure 3-16) and smaller NP (average diameter = 20 nm) are attached to its surface forming a sharp interface with the surrounding OM (Figure 3-16). The auriacusite precipitate is in close proximity to smaller silicate patches, which appear to form a connected pore system toward the auriacusite-filled pore space (Figure 3-16d).

3.3.4. Chemical features in the APT-FIB sections

Spatially reconstructed APT data from all three tips represent approximately 9.5 million atoms in total. Reconstructions of the APT reveal that Na, K, Ca, Si, Al, As, C, Fe, Zn and Cu occur in the OM matrices above the detection limit of the instrument (circa 1 ppm) (Figures 3-17, 3-18, 3-19, 3-20 and 3-21).

Two-dimensional APT plots of the reconstructed data indicate the occurrence of distinct zones in each of the extracted APT-FIBs. For example, the APT-FIB-1 (Figure 3-17) may be divided into three distinct zones (Figure 3-17a): Zone I contains high densities of K, Na, Al and C (OM), whereas zones II and III are characterized by high densities of C (OM) and Si/Fe, respectively. Similarly, the APT-FIB-2 (Figure 3-19) may be divided into three distinct zones (Figure 3-19a): Zone I contains high densities of Ca and Fe, Zone II is characterized by high densities of C (OM), Si, Al, Cu and Zn and zone III contains the highest densities for Cu, Zn and Fe in this sample (Figure 3-19).

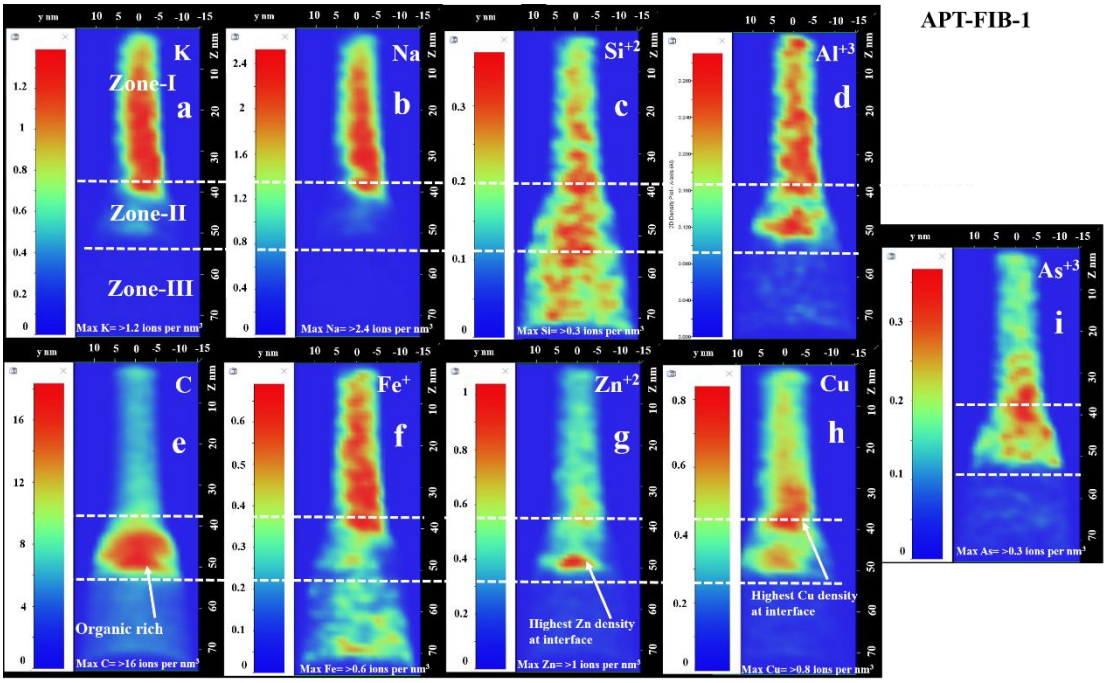

Figure 3-17: Two-dimensional (2D) maps of an APT reconstruction for K, Na, Si, Al, As, C, Fe, Zn and Cu: APT-FIB-1 may be divided into three distinct zones (a): zone I contain high densities of K, Na, Al and C (OM), whereas zones II and III are characterized by high densities of C (OM) and Si/Fe, respectively; metal(loid)s such as Zn, Cu, As and Fe do not occur as prominent clusters but occur in higher densities in certain areas at the interface of zone I and II or within zone II; high densities of metal(loid) overlap with high densities of Si and Al at the zone I-zone II interface or within zone II. All density values are in at./nm^3

In APT-FIB-1 Cu occurs mostly at the interface of zone I and II and is often associated with Si and Al within zone II (Figure 3-17). Fe is homogeneously distributed within zone I, whereas Si and other identified metal(loid)s are heterogeneously distributed within zone I (Figure 3-17). Metal(loid)s such as Zn, Cu, As and Fe do not occur as prominent clusters but occur in higher densities in certain areas along the interface of zone I and II or within zone II; these high densities of metal(loid)s correlate with high densities of Si and Al along the interface of zones I and II and within zone II (Figure 3-17).

Chemical bonding between atomic species may be identified using the atomic radius for Cu^0 (1.28 Å) and the ionic radii for Cu^+ (0.46 Å), Cu^{2+} (0.55 Å), As^{5+} (0.42 Å) C^{4+} (0.17 Å) and O^{2-} (1.4 Å) (Shannon, 1976). Analysis of the APT indicates that all Cu atoms are surrounded by O atoms, thus excluding the presence of metallic Cu species. The bonding between ionic Cu species or between Cu species and other ions may be visualized through plotting the location of Cu species using the sum of the ionic radii of Cu^{2+} and O^{2-} ($0.55+1.4 \approx 2$ Å). Similarly, the occurrence of C and As species may be also plotted using the sums of the ionic radii of As and O ($0.42 + 1.4 \approx 1.8$ Å) and C and O ($0.17 + 1.4 \approx 1.6$ Å). Hence, an overlap between two Cu spheres or one Cu and one As sphere would then represent the presence of Cu-O-Cu and Cu-O-As bonds, respectively. As such, clusters of three Cu-O species (labelled as Cu-O-Cu-O-Cu), one Cu-O and one C-O species (labelled as Cu-O-C) or one As-O and one C-O (labelled as As-O-C) were identified in zone II (Figure 3-18). Clusters containing Cu-O species may be even larger or more complex within the OM matrix considering that only 40% of all atoms are recovered during an APT measurement (Larson et al., 2013).

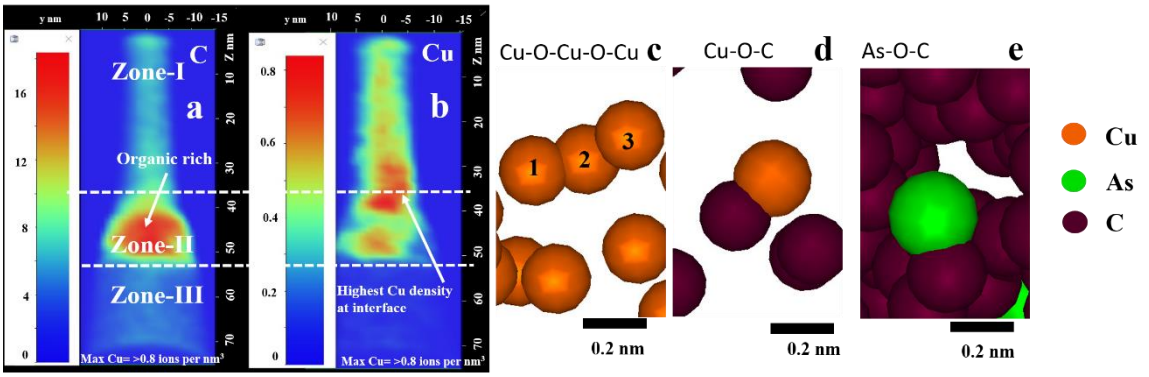

Figure 3-18: (a)-(b) Two-dimensional (2D) maps of an APT reconstruction for (a) C and Cu; (c)-(e) atomic representation of trimer species such as (c) Cu-O-Cu-O-Cu (one O-Cu-O is shown as an orange sphere) and dimer species such as (d) Cu-O-C (the O-C-O species is shown as brown sphere), and (e) As-O-C (the O-As-O species is shown as a green sphere) in zone II which is highlighted with white dashed lines in (a) and (b).

In APT-FIB-2 the densities of Si, Al, Zn and Cu are higher in zone II than I and gradually increase within zone II towards zone III (Figure 3-19a, 3-19b, 3-19c, 3-19d, 3-19d, 3-19e, 3-19f and 3-19g). The densities of Si and Al are higher within zone II and gradually increase towards zone III (Figures 3-19b and 3-19g). High densities of Cu, Fe, Zn correlate within zone II and III and intercalate high densities of Si and Al in zone II (Figure 3-19). Identified clusters containing Cu-O species in zone II and III include, for example, three Cu-O species (Cu-O-Cu-O-Cu) and dimers composed of Cu-O-C and Cu-O-Cu (Figures 3-19h, 3-19i and 3-19j). 3D iso-density maps indicate that size and number of pores with high densities of Cu and Si increase within zone II towards zone III, which has a lower density of C than the interior of zone II (OM) (Figure 3-20). Pore spaces with a high density of Cu in zone II are irregular but are lenticular in zone III and follow the morphology of the interface between zones II and II. Pores with a high density in Si occur in both zones I and II, whereas lenticular pore spaces with a high density in Fe only occur in zone III (Figure 3-20).

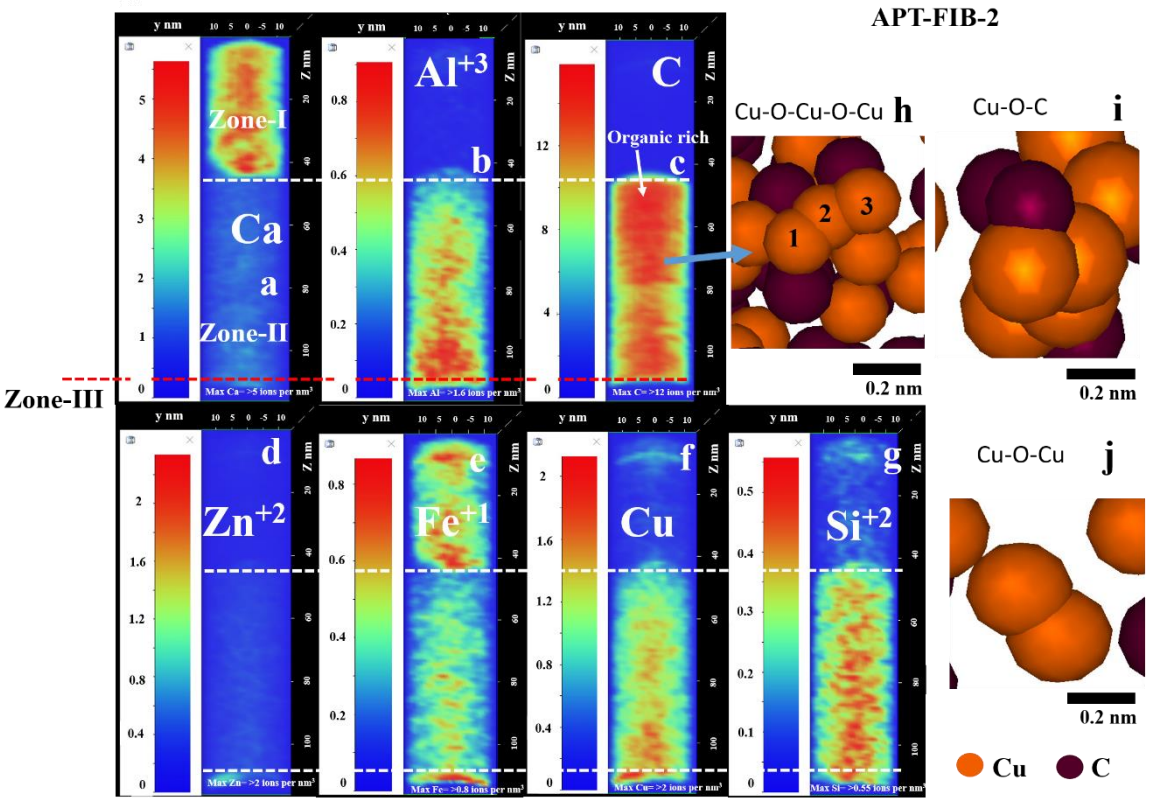

Figure 3-19: Two-dimensional (2D) maps of an APT reconstruction for Ca, Al, C, Zn, Fe, Cu and Si and atomic representation of trimer and dimer species within regions that have high densities of C (OM): APT-FIB-2 may be divided into three distinct zones highlighted with white dashed lines in (a): (a-g) zone I contains high densities of Ca and Fe, whereas Zone II is characterized by high densities of C (OM), Si, Al, Cu and Zn and zone III is characterized by high densities of Cu, Fe and Zn. At a sharp interface between zone I and zone II, the densities of Si, Al, Zn and Cu are relatively higher in zone II and gradually increase within zone II towards zone III. (h)-(j) Trimer species such as (h) Cu-O-Cu-O-Cu (O-Cu-O in orange) and dimer species such as (i) Cu-O-C (O-C-O in purple) and (j), Cu-O-Cu occur in zone II; all density values are in at./nm^3.

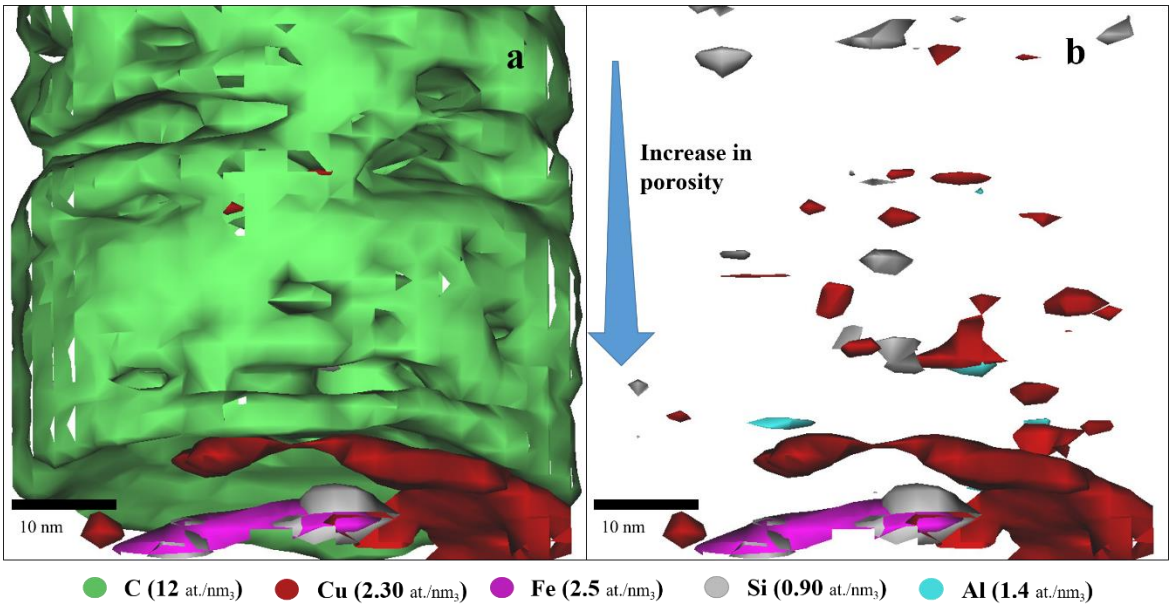

Figure 3-20: 3D-iso density map of APT-FIB-2: (a-b) Gradual increase in the size of high-density Cu regions from 50 to 2 nm may indicate PCS effects. Lenticular zones of high densities for Cu and Fe suggest that the pore shape may have controlled the nucleation of incidental NP within the OM matrix.

To better understand the speciation of Cu in Cu-rich areas , the frequency Cu-*R*-Cu bonds with *R* = O, C, Fe and Zn in zone II and zone III of APT-FIB-2 has been determined using a Cu-Cu nearest neighbor analysis (1NN). The 1NN analysis included the experimental (actual) Cu distribution and compared this distribution with a randomized (averaged) Cu distribution (Philippe et al., 2010; Perea et al., 2015). Little deviation is visually observed between the experimental and random Cu-Cu distribution for zone II, as opposed to zone III of APT-FIB-2. A chi-square statistical test is conducted to quantitatively confirm or reject deviation from randomness. For the chi-square statistical test, the null hypothesis is that the experimental distribution is consistent with the expected random distribution. For the zone II, the calculated X^2 value of 80.8 is greater than the expected X^2 value of 38 on the basis of 27 degrees of freedom and a 95% confidence. The differences between the latter two X^2 values rejects the null hypothesis and confirms that the experimental Cu-Cu 1NN distribution is non-random. Similarly, the 1NN analysis for Zone III

shows a non-random Cu-Cu distribution as the observed X^2 value of 754.6 is much larger than the expected X^2 value of 38 on the basis of 27 degrees of freedom and a 95% confidence. Although Cu-Cu 1NN distributions of both zones exhibit non-randomness, it is obvious that there is greater departure from the randomness for zone III than II, indicating a higher degree of clustering of Cu atoms in zone III than II.

The 1NN analysis investigates the distance between the nearest neighbors of the same element. For example, the distance of Cu to the nearest Cu atom is calculated from the perspective of each individual Cu atom located in the sample space. Although this method allows the investigation of the atomic-scale 3D arrangement of atoms, the lower than ideal detection efficiency of the APT strongly influences the analysis. For example, the loss of some nearest neighbors during APT analysis results in larger distances between the nearest neighbors. Hence, we ignored the absolute frequencies of distances between next neighbor Cu analyses and rather focused on the similarities between these values and those observed in crystal structures of known minerals such as cuprospinel.

The experimental and random Cu-Cu distributions for zones II (Figure 3-21a) and III (Figure 3-21b) indicate that Cu atoms show a short-range order within both zones because the Cu-Cu nearest neighbor distances display maximum frequencies of 5 ± 1.6 Å and 4 ± 1.3 Å, respectively. Here, the full width at half maximum of the Cu-Cu nearest neighbor distance distribution is greater for zone II (mainly OM) than zone III (high proportion of a Cu-bearing phase) (Figure 3-21).

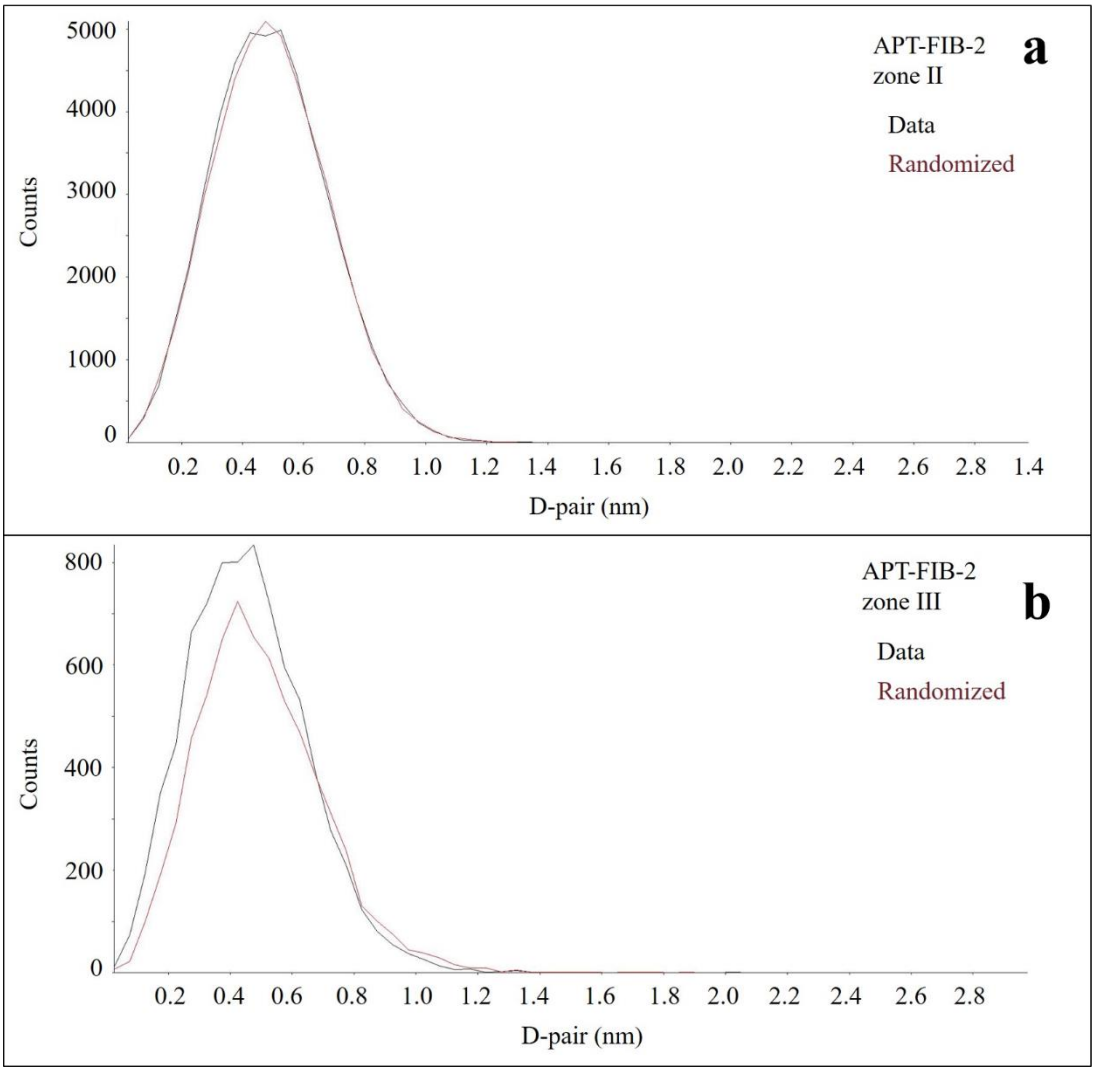

Figure 3-21: First Cu-Cu nearest-neighbor distance distributions in zone II (a) and zone III (b) of APT-FIB-2.

In general, the densities of Cu are higher at the interfaces between the above-described zones (Figures 3-17 and 3-19) or within zones that have C (OM) in high density (Figure 3-19). Within zones that have a high density of C (OM), dimer clusters such as Cu-O-C and Cu-O-Cu are more abundant than trimer clusters such as Cu-O-Cu-O-Cu (Figures 3-18 and 3-19) and higher-order molecular associations of more than three Cu atoms do not occur in regions with the highest density of Cu.

3.4. Discussion

The observed mineralogical composition in the two FIB sections will be discussed first before addressing processes controlling nucleation and aggregation of minerals in nano-sized pore spaces.

3.4.1. Mineralogy of the FIBs

Spinel-type minerals have the general formula AB_2X_4 where the cation A can either occupy a tetrahedrally coordinated site (normal spinel) or an octahedrally coordinated site (inverse spinel) (O'Neill & Navrotsky, 1983). Spinels crystallize in a wide range of environments from the upper mantle to the crust and in extra-terrestrial bodies such as meteorites and moon (Schindler et al., 2019). They are of great significance in geological, environmental and material sciences due to their physical properties and their ability to incorporate a variety of mono-, di-, tri-, tetra- and pentavalent cations (Schindler et al., 2019). Many spinel group minerals do not have widespread geological occurrences but some such as chromite ($FeCr_2O_4$) occur in sufficient quantity to be called important ore minerals. Fe-bearing spinel-group minerals such as magnetite (Fe_3O_4) and maghemite (Fe_3O_4) occur commonly in igneous massifs, metamorphic terrains and in sedimentary deposits (Schindler et al., 2019). Spinel-type minerals such as magnetite also occur as NP in the upper horizons of soils that can form through various abiotic and biotic processes (Schindler et al., 2019). Sn-bearing spinels do not occur in nature and are synthesized for various industrial applications (Šepelák et al., 2012; Yongvanich et al., 2012).

In the current study, a large almost micrometer-size inclusion of cuprospinel occurs in TEM-FIB section 2 (Figure 3-3) and magnetite NP occur in silicate matrices surrounding the larger network of silicate patches or pore channels (Figures 3-5, 3-6, 3-7 and 3-8). Apart from magnetite NP, nano inclusions of lenticular Sn-bearing spinel NP (Figure 3-9) and AM_2O_6 NP with A=Zn, Cu and M=Sn, Sb (Figure 3-10) also occur in close association with silicates in the OM matrix.

Fe-(hydr)oxides commonly occur in various environments such as in sediments formed in oceanic and lacustrine and fluvial systems, laterites and soils, magmatic and metamorphic rocks, hydrothermal and volcanogenic systems, subsurface environments and extraterrestrial materials (Fernández-Remolar, 2015). Fe-(hydr)oxides are common in the Earth's crust and actively participate in various biogeochemical cycles (Fernández-Remolar, 2015). Fe-(hydr)oxide NP are of great environmental significance due to their large surface area and high chemical activity, and

can immobilize heavy metal(loid)s through adsorption or incorporation (Guo & Barnard, 2013). These NP are mostly formed in low-temperature environmental conditions (Guo & Barnard, 2013). Ferrihydrite is usually the first Fe-(hydr)oxide phase to precipitate due to its metastable nature and lowest interfacial free energy and later transforms to more stable phases such as hematite, goethite and lepidocrocite (Guo & Barnard, 2013). The latter minerals are stable under a wide range of environments (Guo & Barnard, 2013). For example, higher humidity, lower temperatures, acidic or alkaline pH conditions favor the formation of goethite over hematite (Guo & Barnard, 2013).

Ferrihydrite is a nano-crystalline phase that has a high density of defects and contains variable amounts of (OH) groups and H_2O molecules (Zhao et al., 1994). The lack of long-range ordering has prevented so far the determination of its structure using X-ray single crystal diffraction data. However, progress is still being made to understand the structure of ferrihydrite using ab-initio calculations (Rancourt & Meunier, 2008; Michel et al., 2010; Boily & Song, 2020). XRD powder patterns of ferrihydrite are commonly composed of either 2 or 6-8 broad peaks and are used to distinguish between 2-line ferrihydrite and 6-line ferrihydrite (Jambor & Dutrizac, 1998; Cornell & Schwertmann, 2003).

This study shows that ferrihydrite NP occur in close association with silicates and contain up to 6 wt% Cu (Figures 3-13 and 3-14). Their occurrence within or in close proximity to silicate patches in the OM matrix suggests that silica species inhibit their transformation and aggregation towards thermodynamically more stable Fe-(hydr)oxide phases. This inhibiting effect of silica species on the transformation of Fe-(hydr)oxide minerals has been widely reported (Zhao et al., 1994; Rzepa et al., 2016).

The formation of silicates, especially clay minerals and amorphous silica provide insights into important geochemical processes in soils and the underlying processes of their formation within OM are still debated. For example, the formation of petrified wood is mainly divided into two broad categories based on the preservation processes, premineralization (formation of silica or other minerals within porous OM matrix) and replacement (formation of silica and other minerals and decomposition of OM). Both of these ideas have been long perpetuated by researchers but Mustoe (2017) indicated for the first time that the premineralization and replacement can occur simultaneously and physiochemical parameters (pH and Eh) dictate which process operates dominantly. Furthermore, X-ray microanalysis of a transverse specimen of pre-

mineralized modern *Pinus contorta* (lodgepole pine) by Hellawell et al. (2015) reveals that silicification mostly occurred near exterior surfaces and along cracks. Subsequent penetration of silicic acid and aluminum hydroxide controls the formation of silicate minerals in a clay matrix (Beardmore et al., 2016).

The formation of these secondary phases in the OM may have been controlled by unique environmental conditions often observed in nano- to micrometer- sized pore spaces. These unique conditions will be discussed next.

3.4.2. Factors controlling nucleation within pore spaces

Nucleation within a porous medium of heterogeneous nature is often difficult to model in experimental setups because various factors such as surface charges, surface energies, matrix effects, diffusion and elemental composition of solute may control the stability of nucleated phases. Here, we will discuss how surface charges, matrix effects, diffusion and pore sizes may have affected the formation of the observed phases in the OM.

3.4.2.1. Surface charge and matrix effects

Surface charge plays an important role in interactions between OM and mineral phases in the soil. These interactions include, for example, the selective adsorption of ionic species along pore walls and channels and the subsequent heterogeneous nucleation of secondary phases. OM has commonly a negative surface charge in the pH range (pH = 3-4), whereas cationic species of Fe, Al and Cu as well as Fe- and Al-(hydr)oxide phases have a positive charge/surface charge over the same pH range. Hence, an electrostatic attraction between OM and Fe- and Al-(hydr)oxides NP should exist in the absence of adsorbed species and electrolytes (Kretzschmar & Schafer, 2005).

Surface interactions are difficult to model due to complex solution chemistry and heterogeneity of OM in soils. For example, OM has diverse surface reactive sites ranging from cationic sulfhydryl (R-SH), and amino groups (R-NH2) to anionic hydroxyls (R-OH) and carboxylic groups (R-COOH) and also the neutral aromatic (-Ar-) and aliphatic ([-CH_2-]n) moieties (Thompson & Goyne, 2012). Furthermore, metal(loid) ionic species such as Cu^{2+} can form both inner-sphere and outer-sphere complexes on negatively charged surfaces and the characterization of the charge distribution in these surface complexes is still a significant challenge (Brown Jr & Calas, 2011).

Type, porosity and permeability of OM create matrix induced effects that can control mineralization of an OM matrix and hence the nucleation within pore spaces (Stack et al., 2014; Mustoe, 2017). Characterization of the quantity and type of functional groups in OM at the nanoscale is impractical, which makes the interpretation of observed features difficult.

Porous zones developed in OM due to pre-mineralization events can be highly selective in ion intake. For example, Plecis et al. (2005) showed that pore opening and channels with negatively charged density can selectively promote and inhibit the diffusion of cations and anions, respectively. Furthermore, the diffusion of an ion into pore spaces is also controlled by its size. For example, experiments by Yang & Garde (2007) showed that the intake of larger relative to smaller cations is favored in the presence of negatively-charged densities within the pore system. Furthermore, pore channels with a higher proportion of hydrophobic surface terminations promote faster diffusion of water than their hydrophilic counterparts with the same diameter (Wang, 2014).

OM matrix can also stabilize metastable Fe-(hydr)oxide phases. For example, ferrihydrite occurs in lipid vesicles and protein nanocages during biomineralization processes leading to magnetite formation in the chiton tooth; biosynthesis of magnetite in the chiton tooth is a two-step process that begins with the formation of ferrihydrite and its transformation to magnetite (Tester et al., 2012; Gordon & Joester, 2013). Fe transport and storage through encapsulation within nano-sized ferritins and similar proteins is a ubiquitous process in biology (Baumgartner et al., 2013). The formation and stability of ferrihydrite in these nano-sized proteins is most likely due to unique conditions induced by the pore size (see below), organic acids and availability of Fe^{3+} species (Baumgartner et al., 2013; Gordon & Joester, 2013; Siponen et al., 2013).

3.4.2.2. Silicon mobility and interactions

Silicon (Si) is a major element within the Earth's crust and is an essential element for plants as it increases their resistance to a wide variety of diseases and pests (Klotzbücher et al., 2020). Si is mainly present as monomeric (H_4SiO_4) or polymeric-silicic acid in soil solutions and its concentrations vary depending on the solubility and composition of primary and secondary silicate minerals (Nguyen et al., 2017b; Klotzbücher et al., 2020). The interaction of silicic acid with mineral surfaces is the major control on the leaching of Si in terrestrial ecosystems (Klotzbücher et al., 2020).

A study by Leo & Barghoorn (1976) revealed that during pre-mineralization of OM, initial silicic acid penetration occurs due to its chemical affinity for hydroxyl groups in holocellulose and lignins, which are the primary structural components of plant vascular tissue and this sets the stage for the episodic intake of silicic acid that ultimately leads to the replacement of OM by silica. After this pre-mineralization process of OM, Si settles mostly in the form of silicates and silica (Mustoe, 2017). Silicic acid can have also a profound effect on the dispersibility of silicates and aggregation of silicates and Fe-(hydr)oxides. For example, Nguyen et al. (2017b) showed that adsorption of silicic acid leads to greater dispersibility of an Fe-rich kaolinitic clay fraction within a specific pH range (4-6) due to reduced zeta potential (which is a measure of the effective electric charge on a specific surface). The lower zeta-potential inhibits the formation of face – edge structures between clay particles, which is necessary to keep their "house-of-cards" structure intact. A study by Nguyen et al. (2017a) showed that adsorption of silicic acid lowers the zeta potential of goethite particles which promotes their aggregation due to the higher abundance of van der Waals (vdW) forces between adsorbed silica species. Si-rich phases such as amorphous silica can serve as favorable heterogeneous nucleation sites due to the presence of hydrophilic functional groups on their surface (Wang et al., 2019). For example, Jadoon & Schindler (2021) showed that CuS_x phases such as covellite NP preferentially nucleate on silica inclusions located within a matrix of organic colloids.

The presence of silica species and their subsequent attachment to ferrihydrite can suppress its transformation to more stable Fe-(hydr)oxide phases such as hematite and goethite (Zhao et al., 1994; Rzepa et al., 2016). This suppression effect is most likely induced by the formation of Fe-O-Si surface terminations, which impede crystal growth (Zhao et al., 1994). Furthermore, adsorption of silicate phases also lowers the internal arrangement and structural order of ferrihydrite particles, which results in higher required temperatures for the transformation of ferrihydrite into stable phases such as hematite (Rzepa et al., 2016).

3.4.2.3. Pore size-controlled solubility

Pore size can control the size of a forming nucleus, which, in turn, controls its solubility in a certain matrix; i.e. surface energy and solubility of a nucleus are inversely proportional to its size (Stack, 2015). In this regard, the pore size-controlled solubility model states that heterogeneous nucleation in smaller pores requires higher supersaturation as compared to larger pores (or bulk fluid) (Putnis, 2015). Hence, a phase may nucleate only in larger pores if smaller

pores or pore channels at a given degree of supersaturation are inhibiting its nucleation. For example, Weber (2017) used a combination of APT and TEM to study radium (Ra) uptake into porous barite and showed that nucleation of a Ra-bearing phase occurs preferentially within macro-pores, whereas nano-pores only contain water and salt precipitates at a given degree of intrinsic supersaturation.

Furthermore, Stack et al. (2014) showed that favorable surface chemistry such as the presence of polar functional groups along pore walls can promote nucleation in nanopores and can act as active redox zones. For example, oxidized and reduced HA and FA functional groups in the OM are active redox centers and can induce the reduction of metal(loid)-bearing species (Sansom & Biggin, 2001; Hyun et al., 2007; Akaighe et al., 2011; Fulda et al., 2013). This was confirmed by Maurer et al. (2013) who showed that the extensive formation of Cu^{+} and metallic Cu occurs at redox-active centers in OM.

3.4.2.4. Size-controlled mineral stability

Thermodynamic stability of NP shifts with a decrease in particle size due to unique physico-chemical properties and surface interactions at the nanoscale. A crossover in surface free energy with decreasing particle size contributes to this shift in stability of phases at bulk vs nanoscale (Chernyshova et al., 2007; Guo & Barnard, 2013). For example, a study by Navrotsky et al. (2008) showed that the shift in stability of Fe-(hydr)oxide phases occur at the nanoscale. These authors determined the surface area vs surface energy relationship using dissolution enthalpies (ferrihydrite values are approximated due to its variable chemical composition) and showed that Akaganeite (β-FeOOH) becomes a stable Fe-(hydr)oxide phases with decreasing particle size. Simulation studies based on thermodynamic data show that ferrihydrite is the most common and stable Fe-(hydr)oxide phase formed at the nanoscale and that its stability threshold lies at 8 nm and above this threshold, rearrangement, reordering and Ostwald ripening result in the transformation of ferrihydrite to nano-hematite or goethite (Hiemstra, 2015). Experimental studies are in accord with these calculations: they indicate that ferrihydrite NP are unstable above ~ 6 nm (Michel et al., 2010). Another study by Navrotsky et al. (2010) also showed that the surface energies of oxyhydroxide, spinel and oxide NP increases in the following order: oxyhydroxides < spinels < oxides and this order may represent their relative stability at a given size.

3.4.2.5. Crystallization through particle attachment

Brownian motion of NP results in random collisions among themselves and with other mineral phases (Hotze et al., 2010; De Yoreo et al., 2015). These collisions can result either in their attachment, rotation on the surface, or detachment depending on the strength of intermolecular forces. For example, Derjaguin–Landau–Verwey–Overbeek (DLVO) theory describes that attachment of particles is controlled by the sum of attractive and repulsive forces that are commonly vdW and EDL forces, respectively (Verwey et al., 1948; Hotze et al., 2010; De Yoreo et al., 2015). Factors such as surface charge, particle size, shape, the type of ionic species in solution, adsorbed species and alteration layers control the strength of these attractive and repulsive forces in a certain matrix (Hotze et al., 2010). Physical and chemical properties of a solution, flow paths, flow regimes (laminar or turbulent) and surface potentials of NP can also greatly influence the agglomeration of NP; i.e. higher values of Dean number (a dimensionless number giving the ratio of the viscous force acting on a fluid flowing in a curved pore channel to the centrifugal force) and particle density and lower values of Reynolds number (the ratio of inertial forces to viscous forces) and permeability can promote agglomeration of NP in a certain matrix (Choi et al., 2013; Liyanage et al., 2016). Minimization of surface charges can promote homoaggregation (aggregation of same types of NP), whereas opposite surface charges promote heteroaggregation (aggregation of different type of NP or attachment of NP to the surface of other minerals) (Schindler & Hochella, 2017). For example, Schindler & Hochella (2017) showed the occurrence of homoaggregation of anglesite and kintoreite NP (PZC = 4 $\approx$ pH_{bulk}) and the attachment of near neutral-charged NP of anglesite to negatively charged surfaces of illite (PZC < pH_{bulk}), assuming that the pH within pore spaces of mineralized OM is similar to the pH of the bulk soil.

An increasing number of studies show that in contrast to the conventional models that state that crystal growth occurs when individual ions are sequentially added to a growing crystal face, crystallization through particle attachment (CPA) is a common crystallization mechanism, especially in the case of biologically-induced nucleation processes (De Yoreo et al., 2015). CPA involves the attachment of already-formed NP in the solution to the growing crystal face. If NP are amorphous, their agglomeration occurs through amorphous-to-crystalline pathway. In the case of crystalline NP, agglomeration occurs either in oriented attachment (i.e. attachment of NP to a growing crystal face in a specific crystallographic orientation) or random attachment (i.e.

attachment of NP to a growing crystal face in random crystallographic orientation) (Schindler & Hochella, 2017). Coulombic and Lewis acid-base interactions between NP surfaces and larger aggregates control the oriented attachment, whereas incorporation of NP into bulk crystal via random attachment requires structural re-organization (Banfield et al., 2000; Zhang et al., 2014; De Yoreo et al., 2015). Schindler & Hochella (2017) observed CPA for anglesite and kintoreite NP in silica matrices within mineralized OM and showed that mineral growth via the non-conventional CPA model is of great environmental importance in contaminated oxic soils as it explains the formation and aggregation of metal(loid)-bearing NP.

3.4.2.6. Role of precursors in the formation of incidental NP

Natural NP have been abundant within the Earth's systems since the formation of the Earth. However, NP can form through anthropogenic activities and are classified into two major types: (I) engineered NP, which are purposely manufactured to be at the nano-sized and (II) incidental NP, which form through anthropogenic activities (Hochella et al., 2019). Incidental NP are more abundant than engineered NP and they almost rival their natural counterparts in many environmental components (Hochella et al., 2008). Incidental NP can form via various pathways, which include the formation of NP via complexes, clusters, small molecules and polyatomic ions (so called precursors) which in turn can form larger aggregates leading to bulk solids (De Yoreo et al., 2015; Van Driessche et al., 2016). The formation of NP aggregates via this pathway can lead to the production of NP heteroaggregates that are more stable than single-phase bulk crystals (Hochella et al., 2019). The transition of precursor to NP or NP aggregates is a complex process governed by various redox and hydrolysis processes as well as dissolution and precipitation reactions (Hochella et al., 2019). Precursors may or may not lead to bulk phases becuase their transition can stop at any point due to physico-chemical constraints induced by their surroundings (Hochella et al., 2019). These precursors usually form in manipulated lands such as urban, agricultural, industrial and mining areas or in the troposphere that lies over regions of high industrial activity or high population density. For example, the presence of sulfuric acid and other compounds in the atmosphere due to anthropogenic emissions leads to the formation of precursors, which aggregate and form stable NP through condensation of vapors containing OM in feasible conditions (Hochella Jr et al., 2012; Kulmala et al., 2014). Furthermore, precursors are usually not stable species but can persist for longer periods and can aggregate upon finding suitable surfaces. For example, Rozan et al. (2000) showed the presence of multinuclear metal(loid)-sulfide (Cu, Fe

and Zn) clusters in oxic rivers that are resistant to dissociation and oxidation and have high stability constants. The formation of NP through precursors, contributes approximately 74% of the total NP in the atmosphere (Merikanto et al., 2009); hence, their study is necessary to get insights into the complex formation mechanisms of stable incidental NP that persist in various environmental components and can transport metal(loid)s to greater distances.

3.5. Model of formation

The formation and stability of Cu- and Fe-bearing incidental NP within pores of OM may been controlled by the following processes and steps (Figure 3-22).

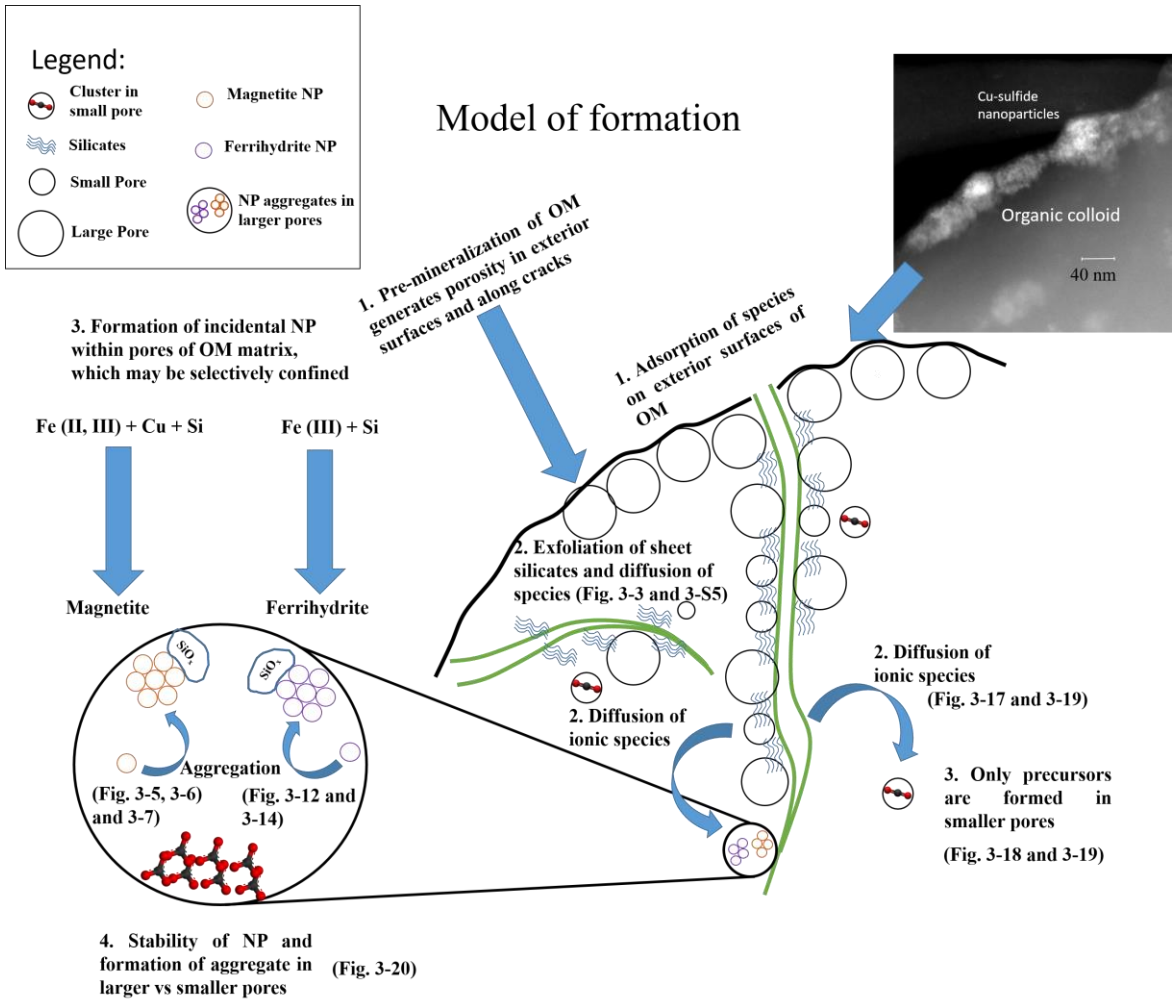

Figure 3-22: Model of formation: the sequestration of Cu and other metal(loid)s have occurred in the following sequence: (I) pre-mineralization of OM and adsorption of Cu

aqueous species, (II) diffusion of Cu aqueous species through porous zones, (III) Formation of precursors and their respective NP in nanosized pores, (IV) aggregation of NP and their long-term stabilization due to adsorbed silica species.

I. ***Premineralization and adsorption***

During pre-mineralization, the outer surfaces of the OM matrix are mineralized first and porosity is generated around the mineralized zones either due to OM degradation or cracks propagation (Figure 3-3) (Hellawell et al., 2015). This observation is consistent with experimental and simulation studies, which indicate that nucleation in a matrix preferentially occurs in regions of initial fluid penetration because they can easily become supersaturated with respect to a certain mineralogical phase (Figure 3-3) (Noiriel et al., 2016; Fazeli et al., 2020; Jadoon & Schindler, 2021). As pre-mineralization progresses, restructuring of flow paths and alteration of size, shape, connectivity and distribution of pores greatly alter the porosity-permeability of a matrix. Closure of pore throats, as well as variation in hydrodynamic properties of pore channels leading to them, can make certain pore spaces highly confined (Noiriel et al., 2016).

Electrostatic attraction most likely promoted the adsorption of cationic Fe- and Cu-bearing aqueous species on the surface of negatively charged pre-mineralized OM. Additionally, the adsorption of cations can reverse the charge of OM, which can then lead to the adsorption of anions as well (Tiberg et al., 2013; Schindler et al., 2016).

II. ***Diffusion***

Metal(loid) species adsorbed on OM surfaces and pore solutions containing metal(loid)-bearing aqueous species diffuse into the porous zones developed during the pre-mineralization of OM. The occurrence of silicate phases along cracks and formation of incidental NP in close proximity to these silicate phases indicate that pre-mineralization has strong control over the formation of incidental NP within OM. For example, the occurrence of metal(loid)-bearing NP (Fe-(hydr)oxides, spinels, cuprite, spertiniite, Cu-bearing arsenate) at the interface of silicate patches towards the OM indicates that these NP formed in areas pre-mineralized by silicate phases (Figure 3-3 and 3-16)). For example, NP of cuprite and spertiniite occur around a silicate phase (Figure 3-11) and a lepidocrocite NP aggregate (Figure 3-15), indicating that both types of NP formed after the generation of silicate and Fe-(hydr)oxides phases. Additionally, the occurrence of

silicate rims around Fe-(hydr)oxide NP (Figure 3-14) and the heterogeneous distribution of Si and Al within silicates (Figures 3-4, 3-5 and 3-6) indicate the episodic intakes of silicic acid and Al- and Fe-hydroxides. Silicate phases of the first generation may have exfoliated (Figure S5) with time (due to degradation of OM) and provided diffusion pathways and pore channels for the intake of silica- and Al-, Fe- and other metal(loid) species into the OM matrix (Smykatz-Kloss et al., 2003).

The occurrence of Cu in close association with the Si, Al and other metal(loid)s in the APT data and their common distribution within the OM matrix are in agreement with the TEM findings and indicate that zones with a high density of Si and Al are most likely pre-mineralized porous zones within OM that promoted the diffusion of Cu, Fe, Zn and other metal(loid)-bearing species (Figure 3-17, 3-18 and 3-19). For example, the distribution of K, Na and Al in zones I and II in APT-FIB-1 suggests different degrees of pre-mineralization of the OM matrix (Figure 3-17). The high density of Cu at the interface between zone I and zone II in APT-FIB-1 might be due to lower porosity in zone II and accumulation of Cu and other metal(loid) species along the zone boundary and their slow diffusion into zone II (Figure 3-17). Similarly, the common distribution (low to high from zone II towards zone III) of Cu, Fe, Zn, Si and Al within OM in zone II of APT-FIB-2 is most likely due to the fact that pre-mineralized zones within OM promoted the diffusion of metal(loid)-bearing species within the OM matrix (Figure 3-19).

III. ***Nucleation***

The presence and distribution of silicate phases have considerable control over the nucleation of incidental NP as they not only generate porosity but also provide favorable surfaces for heterogeneous nucleation (Jadoon & Schindler, 2021). Therefore, most of the incidental NP such as ferrihydrite, magnetite, cuprite and spertiniite occur in silicate matrices or in close association with silicate phases (Figure 3-17). The common occurrence of Cu, Fe, Zn, Al and Si in zone II of both APT-FIB-1 and APT-FIB-2 also confirms this relationship (Figures 3-17, 3-18, 3-19 and 3-20) and might indicate the preferential formation of phases in porous zones during pre-mineralization. These observations are in accord with the observation by Jadoon & Schindler (2021) who showed that heterogeneous nucleation of covellite NP often occurs on nano-sized silica inclusions within pre-mineralized OM. The authors suggested that silica stabilized and aided in the formation of covellite NP, which is most likely due to the presence of hydrophilic (polar) functional groups on the surface of the silica inclusions. Furthermore, the presence of hydrophobic

functional groups in OM may have promoted the growth of larger aggregates (Figures 3-12, 3-13 and 3-14), whereas smaller aggregates (Figures 3-5 and 3-6) occur on hydrophilic functional groups in silicates. For example, an experimental study by Deng et al. (2020) indicated that the nucleation free energy barrier on hydrophilic surfaces is lower than on hydrophobic surfaces. This results in a more rapid formation of smaller particles and aggregates on hydrophilic surfaces, whereas larger aggregates are observed on more hydrophobic surfaces. Occurrences of NP aggregates with lattice fringes in the same and different orientations (Figure 3-5, 3-6, 3-12, 3-13 and 3-14) and their oriented attachment (Figure 3-7) are indicative of both crystallization through particle attachment (CPA) and Ostwald ripening (Thanh et al., 2014), which could be the dominant processes leading to the formation of incidental NP in nanopore spaces.

Apart from the occurrence of silicate phases, availability of metal(loid) aqueous species most likely controlled the nucleation of incidental NP. For example, the low availability of Cu and Zn aqueous species in a pore space probably promoted the formation of ferrihydrite aggregates (Figures 3-13 and 3-14), whereas the increased availability of these elements most likely promoted the formation of magnetite NP (Figures 3-5, 3-6, 3-7 and 3-8) or Zn-Sn-Fe-spinel (Figure 3-9). The availability of metal(loid)-bearing aqueous species in pore spaces within OM matrix is probably controlled by the chemistry of the infiltrated pore solution as well as the hydrodynamic properties of the pore channels, which control the diversity of species reaching large pore spaces (Noiriel et al., 2016).

PCS can also have a profound effect on the nucleation of incidental NP within nanosized pores. For example, a gradual increase in the density of Cu from zone II towards zone III in APT-FIB-2 most likely indicates preferential nucleation within larger pores or a change from low to high porosity (Figure 3-20). This is in accord with the observations of Weber (2017) that the preferential nucleation of $Ba_xRa_{1-x}SO_4$ occurs in larger (200 nm) vs smaller pores (<50 nm). Pore shape also might have an effect on the morphology of the nucleated phases as indicated by the occurrence of lenticular spinel phases (Figures 3-8 and 3-9) as well as the occurrence of lenticular regions in zone III of APT-FIB-2 with high densities of Cu and Fe (Figure 3-20).

The type and number of polymerized Cu-polyhedra in areas with a high density of Cu may provide insights into the chemical composition of precursors. Cu-oxide species such as Cu_nO_n and Cu_nO_{n-1} series have linear structures for n = 2,3 and n = 2, 3 and 4 respectively (Abdul Latif et al.,

2018). More complex Cu-(hydr)oxide polymeric species occur in larger clusters such as $[Cu_{12}(OH)_{24}]$ or as 1-D chains in $Cu(OH)_2$ (Kondinski & Monakhov, 2017). Hence, the identified trimer of Cu-oxy or Cu-hydroxy polyhedra may represent parts of a complex polymeric Cu-oxide species, which subsequently leads to the nucleation of a Cu-(hydr)oxide. The occurrence of precursors, clusters and NP has also been observed in surfactant solution. In their work, Yao et al. (2010) reported that synthesis of gold NP occurred in three steps: (I) Formation of $AuCl_4^-$ dimers and trimers, (II) formation of small Au_{13} clusters and (III) formation of larger Au NP

A Cu-Cu nearest neighbor distance of 4 ± 1 Å in zone III of APT-FIB-2 most likely corresponds to a Cu-Cu distance of 4 Å in inverse spinel structure, where half of the octahedral sites are occupied by the Cu atoms (Figures 3-21 and 3-S7). Furthermore, the larger Cu-Cu nearest neighbor distance of 5 ± 1.25 Å in zone II (OM) of the APT-FIB-2 is most likely due to an increased proportion of Cu carboxylate chelate O-ring structures identified by Manceau & Matynia, 2010as they have a Cu-Cu distance of 5.26 Å along one of their axis (Manceau & Matynia, 2010) (Figures 3-21 and 3-S8).

IV. *Phase stability*

Size of NP might have controlled their stability in nano-sized pore space; however, pre-mineralization of OM might have also played a vital role in the stabilization of NP aggregates. The silicates formed during pre-mineralization of OM can not only provide favorable surface sites for heterogeneous nucleation but can also promote long-term stability and agglomeration of nuclei (Figures 3-5, 3-6, 3-7, 3-8, 3-9, 3-10, 3-11, 3-12, 3-13, 3-14 and 3-15). The occurrence of ferrihydrite NP aggregates within silica patches suggests that they formed through heterogeneous nucleation on silanol groups and silica might have suppressed the transformation of ferrihydrite to other stable Fe-(hydr)oxide phases such as hematite, goethite and lepidocrocite. Furthermore, the presence of silicate rims around ferrihydrite aggregates (Figure 3-14) suggests that episodic silicic acid intakes into pores might have also played a vital role in the stabilization of Fe-(hydr)oxide NP and promoted their aggregation (Nguyen et al., 2017a). This is in accord with the observations of Jadoon & Schindler (2021) who showed that the presence of silica could suppress transformation of ferrihydrite to stable Fe-(hydr)oxides in organic colloids and Schindler et al. (2009) who showed that silicic acid species have high affinity towards Fe-O surface terminations.

3.6. Conclusions

This study shows that the combination of TEM and APT can be a powerful method to study the formation of Cu-bearing incidental NP occurring at the nano- or subnano-scale. Most of the identified mechanisms related to the formation of Cu-bearing incidental NP or their precursors within OM matrix cannot be identified through bulk-techniques such as ICP-MS, XRD and various synchrotron-based techniques. Therefore, their characterization via a combination of TEM and APT provides valuable insights into geochemical and mineralogical processes related to the formation of incidental NP and their respective precursors within the OM.

We showed in this study that the formation of incidental NP within OM is a complex process and is primarily controlled by the pre-mineralization of OM, which results in the formation of silica and silicates along the exterior and interior surfaces and cracks, which in turn generate porous zones along these regions. Porosity promotes the diffusion of metal(loid) species and their adsorption on silica and silicate surfaces, which subsequently results in the formation of incidental NP. The diffusion of metal(loid) species is most likely controlled by the hydrodynamic properties of pore channels as well as by hydrophobic functional groups located within the OM. Availability of silica/silicates (which promote the heterogeneous nucleation), heterogeneity of OM (distribution of polar functional groups), availability of metal(loid) aqueous species and PCS effects most likely controlled the formation of precursors and their subsequent incidental NP. Non-conventional models of nucleation such as crystallization through particle attachment and Ostwald ripening may have operated dominantly during the formation of incidental NP. Furthermore, adsorption of silica species and episodic silicic acid intake most likely stabilized metastable Fe-(hydr)oxide phases such as ferrihydrite.

Our study provides new insights in the formation mechanisms of incidental NP in OM and indicates that sequestration of metal(loid)s within pre-mineralized OM can result in the formation of Cu clusters (precursors), which can either remain stable or aggregate to form NP in larger pores. However, more experimental studies are needed to (a) study the formation of metal(loid)-bearing precursors within the OM and (b) to understand their aggregation mechanisms in relation to PCS effects on the formation of NP.

3.7. References

Abdul Latif, M., Wu, J. W., Moriyama, R., Nakano, M., Ohshimo, K., & Misaizu, F. (2018). Stable Compositions and Structures of Copper Oxide Cluster Cations Cu N O M+(N= 2–8) Studied by Ion Mobility Mass Spectrometry. *ACS Omega, 3*(12), 18705-18713.

Adamo, P., Dudka, S., Wilson, M., & McHardy, W. (1996). Chemical and Mineralogical Forms of Cu and Ni in Contaminated Soils from the Sudbury Mining and Smelting Region, Canada. *Environmental Pollution, 91*(1), 11-19.

Ahn, J. H., Xu, H., & Buseck, P. R. (1997). Transmission Electron Microscopy of Native Copper Inclusions in Illite. *Clays and Clay Minerals, 45*(2), 295-297.

Akaighe, N., MacCuspie, R. I., Navarro, D. A., Aga, D. S., Banerjee, S., Sohn, M., & Sharma, V. K. (2011). Humic Acid-Induced Silver Nanoparticle Formation under Environmentally Relevant Conditions. *Environmental Science & Technology, 45*(9), 3895-3901.

Alloway, B. J. (2012). *Heavy Metals in Soils: Trace Metals and Metalloids in Soils and Their Bioavailability* (Vol. 22): Springer Science & Business Media.

Banfield, J. F., Welch, S. A., Zhang, H., Ebert, T. T., & Penn, R. L. (2000). Aggregation-Based Crystal Growth and Microstructure Development in Natural Iron Oxyhydroxide Biomineralization Products. *Science, 289*(5480), 751-754.

Baumgartner, J., Morin, G., Menguy, N., Gonzalez, T. P., Widdrat, M., Cosmidis, J., & Faivre, D. (2013). Magnetotactic Bacteria Form Magnetite from a Phosphate-Rich Ferric Hydroxide Via Nanometric Ferric (Oxyhydr) Oxide Intermediates. *Proceedings of the National Academy of Sciences, 110*(37), 14883-14888.

Beardmore, J., Lopez, X., Mujika, J. I., & Exley, C. (2016). What Is the Mechanism of Formation of Hydroxyaluminosilicates? *Scientific Reports, 6*(1), 1-8.

Bhattacharyya, A., Schmidt, M. P., Stavitski, E., & Martínez, C. E. (2018). Iron Speciation in Peats: Chemical and Spectroscopic Evidence for the Co-Occurrence of Ferric and Ferrous Iron in Organic Complexes and Mineral Precipitates. *Organic Geochemistry, 115*, 124-137.

Blum, T. B., Darling, J. R., Kelly, T. F., Larson, D. J., Moser, D. E., Perez-Huerta, A., Prosa, T. J., Reddy, S. M., Reinhard, D. A., & Saxey, D. W. (2018). Best Practices for Reporting Atom Probe Analysis of Geological Materials. *Microstructural Geochronology: Planetary records down to atom scale*, 369-373.

Boily, J.-F., & Song, X. (2020). Direct Identification of Reaction Sites on Ferrihydrite. *Communications Chemistry, 3*(1), 1-8.

Bonef, B., Gérard, L., Rouvière, J.-L., Grenier, A., Jouneau, P.-H., Bellet-Amalric, E., Mariette, H., André, R., & Bougerol, C. (2015). Atomic Arrangement at Znte/Cdse Interfaces Determined by High Resolution Scanning Transmission Electron Microscopy and Atom Probe Tomography. *Applied Physics Letters, 106*(5), 051904.

Bonham-Carter, G., Henderson, P., Kliza, D., & Kettles, I. (2006). Comparison of Metal Distributions in Snow, Peat, Lakes and Humus around a Cu Smelter in Western Quebec, Canada. *Geochemistry: Exploration, Environment, Analysis, 6*(2-3), 215-228.

Branson, O., Bonnin, E. A., Perea, D. E., Spero, H. J., Zhu, Z., Winters, M., Hönisch, B., Russell, A. D., Fehrenbacher, J. S., & Gagnon, A. C. (2016). Nanometer-Scale Chemistry of a Calcite Biomineralization Template: Implications for Skeletal Composition and Nucleation. *Proceedings of the National Academy of Sciences, 113*(46), 12934-12939.

Brown Jr, G. E., & Calas, G. (2011). Environmental Mineralogy–Understanding Element Behavior in Ecosystems. *Comptes Rendus Geoscience, 343*(2-3), 90-112.

Cao, M., Evans, N. J., Reddy, S. M., Fougerouse, D., Hollings, P., Saxey, D. W., McInnes, B. I., Cooke, D. R., McDonald, B. J., & Qin, K. (2019). Micro-and Nano-Scale Textural and Compositional Zonation in Plagioclase at the Black Mountain Porphyry Cu Deposit: Implications for Magmatic Processes. *American Mineralogist: Journal of Earth and Planetary Materials, 104*(3), 391-402.

Chernyshova, I., Hochella Jr, M., & Madden, A. (2007). Size-Dependent Structural Transformations of Hematite Nanoparticles. 1. Phase Transition. *Physical Chemistry Chemical Physics, 9*(14), 1736-1750.

Choi, C.-H., Su, Y.-W., & Chang, C.-h. (2013). Effects of Fluid Flow on the Growth and Assembly of Zno Nanocrystals in a Continuous Flow Microreactor. *CrystEngComm, 15*(17), 3326-3333.

Chopin, E., & Alloway, B. (2007). Trace Element Partitioning and Soil Particle Characterisation around Mining and Smelting Areas at Tharsis, Ríotinto and Huelva, Sw Spain. *Science of The Total Environment, 373*(2-3), 488-500.

Cornell, R. M., & Schwertmann, U. (2003). *The Iron Oxides: Structure, Properties, Reactions, Occurrences and Uses*: John Wiley & Sons.

De Yoreo, J. J., Gilbert, P. U., Sommerdijk, N. A., Penn, R. L., Whitelam, S., Joester, D., Zhang, H., Rimer, J. D., Navrotsky, A., & Banfield, J. F. (2015). Crystallization by Particle Attachment in Synthetic, Biogenic, and Geologic Environments. *Science, 349*(6247).

Deng, Y.-H., Yang, Z.-Q., & Ma, R.-M. (2020). Growth of Centimeter-Scale Perovskite Single-Crystalline Thin Film Via Surface Engineering. *Nano Convergence, 7*(1), 1-7.

Denis, F. T. (1933). An Investigation of the Mineral Composition of the Ores of Noranda Mines Ltd. *McGill University Libraries*.

Devaraj, A., Perea, D. E., Liu, J., Gordon, L. M., Prosa, T. J., Parikh, P., Diercks, D. R., Meher, S., Kolli, R. P., & Meng, Y. S. (2018). Three-Dimensional Nanoscale Characterisation of Materials by Atom Probe Tomography. *International Materials Reviews, 63*(2), 68-101.

Dinis, L., Bégin, C., Savard, M. M., & Parent, M. (2020). Impacts of Smelter Atmospheric Emissions on Forest Nutrient Cycles: Evidence from Soils and Tree Rings. *Science of The Total Environment*, 141427.

El Dien, H. G., Arai, S., Doucet, L.-S., Li, Z.-X., Kil, Y., Fougerouse, D., Reddy, S. M., Saxey, D. W., & Hamdy, M. (2019). Cr-Spinel Records Metasomatism Not Petrogenesis of Mantle Rocks. *Nature communications, 10*(1), 1-12.

Ettler, V. (2016). Soil Contamination near Non-Ferrous Metal Smelters: A Review. *Applied Geochemistry, 64*, 56-74.

Fazeli, H., Masoudi, M., Patel, R. A., Aagaard, P., & Hellevang, H. (2020). Pore-Scale Modeling of Nucleation and Growth in Porous Media. *ACS Earth and Space Chemistry, 4*(2), 249-260.

Fernández-Remolar, D. C. (2015). Iron Oxides, Hydroxides and Oxy-Hydroxides. *Encyclopedia of astrobiology*, 1268-1270.

Fulda, B., Voegelin, A., Maurer, F., Christl, I., & Kretzschmar, R. (2013). Copper Redox Transformation and Complexation by Reduced and Oxidized Soil Humic Acid. 1. X-Ray Absorption Spectroscopy Study. *Environmental Science & Technology, 47*(19), 10903-10911.

Gammons, C. H., & Frandsen, A. K. (2001). Fate and Transport of Metals in H2s-Rich Waters at a Treatment Wetland. *Geochemical Transactions, 2*(1), 1-15.

Genareau, K., Perez-Huerta, A., & Laiginhas, F. (2019). Atom Probe Tomography Analysis of Exsolved Mineral Phases. *JoVE (Journal of Visualized Experiments)*(152), e59863.

Gopon, P., Douglas, J. O., Auger, M. A., Hansen, L., Wade, J., Cline, J. S., Robb, L. J., & Moody, M. P. (2019). A Nanoscale Investigation of Carlin-Type Gold Deposits: An Atom-Scale Elemental and Isotopic Perspective. *Economic Geology, 114*(6), 1123-1133.

Gordon, L., & Joester, D. (2013). *Understanding the Biological Stabilization of Ferrihydrite and Its Transformation to Magnetite.* Paper presented at the APS March Meeting Abstracts.

Grenier, A., Duguay, S., Barnes, J., Serra, R., Rolland, N., Audoit, G., Morin, P., Gouraud, P., Cooper, D., & Blavette, D. (2015). Three Dimensional Imaging and Analysis of a Single Nano-Device at the Ultimate Scale Using Correlative Microscopy Techniques. *Applied Physics Letters, 106*(21), 213102.

Guo, H., & Barnard, A. S. (2013). Naturally Occurring Iron Oxide Nanoparticles: Morphology, Surface Chemistry and Environmental Stability. *Journal of Materials Chemistry A, 1*(1), 27-42.

Gustafsson, J. P., Pechová, P., & Berggren, D. (2003). Modeling Metal Binding to Soils: The Role of Natural Organic Matter. *Environmental Science & Technology, 37*(12), 2767-2774.

Hellawell, J., Ballhaus, C., Gee, C. T., Mustoe, G. E., Nagel, T. J., Wirth, R., Rethemeyer, J., Tomaschek, F., Geisler, T., & Greef, K. (2015). Incipient Silicification of Recent Conifer Wood at a Yellowstone Hot Spring. *Geochimica et Cosmochimica Acta, 149*, 79-87.

Hiemstra, T. (2015). Formation, Stability, and Solubility of Metal Oxide Nanoparticles: Surface Entropy, Enthalpy, and Free Energy of Ferrihydrite. *Geochimica et Cosmochimica Acta, 158*, 179-198.

Hochella Jr, M. F., Aruguete, D., Kim, B., & Madden, A. S. (2012). Naturally Occurring Inorganic Nanoparticles: General Assessment and a Global Budget for One of Earth's Last Unexplored Major Geochemical Components. *Nature's nanostructures*, 1-31.

Hochella, M. F., Lower, S. K., Maurice, P. A., Penn, R. L., Sahai, N., Sparks, D. L., & Twining, B. S. (2008). Nanominerals, Mineral Nanoparticles, and Earth Systems. *Science, 319*(5870), 1631-1635.

Hochella, M. F., Mogk, D. W., Ranville, J., Allen, I. C., Luther, G. W., Marr, L. C., McGrail, B. P., Murayama, M., Qafoku, N. P., & Rosso, K. M. (2019). Natural, Incidental, and Engineered Nanomaterials and Their Impacts on the Earth System. *Science, 363*(6434).

Hofacker, A. F., Voegelin, A., Kaegi, R., Weber, F.-A., & Kretzschmar, R. (2013). Temperature-Dependent Formation of Metallic Copper and Metal Sulfide Nanoparticles During Flooding of a Contaminated Soil. *Geochimica et Cosmochimica Acta, 103*, 316-332.

Hoffmann, K., Bouchet, S., Christl, I., Kaegi, R., & Kretzschmar, R. (2020). Effect of Nom on Copper Sulfide Nanoparticle Growth, Stability, and Oxidative Dissolution. *Environmental Science: Nano, 7*(4), 1163-1178.

Hotze, E. M., Phenrat, T., & Lowry, G. V. (2010). Nanoparticle Aggregation: Challenges to Understanding Transport and Reactivity in the Environment. *Journal of Environmental Quality, 39*(6), 1909-1924.

Hyun, J.-H., Smith, A. C., & Kostka, J. E. (2007). Relative Contributions of Sulfate-and Iron (Iii) Reduction to Organic Matter Mineralization and Process Controls in Contrasting Habitats of the Georgia Saltmarsh. *Applied Geochemistry, 22*(12), 2637-2651.

Ilton, E. S., & Veblen, D. R. (1988). Copper Inclusions in Sheet Silicates from Porphyry Cu Deposits. *Nature, 334*(6182), 516-518.

Ilton, E. S., & Veblen, D. R. (1993). Origin and Mode of Copper Enrichment in Biotite from Rocks Associated with Porphyry Copper Deposits; a Transmission Electron Microscopy Investigation. *Economic Geology, 88*(4), 885-900.

Jadoon, S., & Schindler, M. (2021). The Role of Nanopores within Organic Colloids in the Sequestration and Mobilization of Copper within Contaminated Oxic Soils (Submitted). *Environmetal Science: Nano*.

Jambor, J. L., & Dutrizac, J. E. (1998). Occurrence and Constitution of Natural and Synthetic Ferrihydrite, a Widespread Iron Oxyhydroxide. *Chemical reviews, 98*(7), 2549-2586.

Johnson, C. A., Freyer, G., Fabisch, M., Caraballo, M. A., Küsel, K., & Hochella, M. F. (2014). Observations and Assessment of Iron Oxide and Green Rust Nanoparticles in Metal-Polluted Mine Drainage within a Steep Redox Gradient. *Environmental Chemistry, 11*(4), 377-391.

Kerr, D. J., & Gibson, H. L. (1993). A Comparison of the Horne Volcanogenic Massive Sulfide Deposit and Intracauldron Deposits of the Mine Sequence, Noranda, Quebec. *Economic Geology, 88*(6), 1419-1442.

Kettles, I. M., & Bonham-Carter, G. F. (2002). Modelling Dispersal of Metals from a Copper Smelter at Rouyn-Noranda (Québec, Canada) Using Peatland Data. *Geochemistry: Exploration, Environment, Analysis, 2*(2), 99-110.

Klotzbücher, T., Treptow, C., Kaiser, K., Klotzbücher, A., & Mikutta, R. (2020). Sorption Competition with Natural Organic Matter as Mechanism Controlling Silicon Mobility in Soil. *Scientific Reports, 10*(1), 1-11.

Knight, R., & Henderson, P. (2006). Smelter Dust in Humus around Rouyn-Noranda, Quebec. *Geochemistry: Exploration, Environment, Analysis, 6*(2-3), 203-214.

Kondinski, A., & Monakhov, K. Y. (2017). Breaking the Gordian Knot in the Structural Chemistry of Polyoxometalates: Copper (Ii)–Oxo/Hydroxo Clusters. *Chemistry–A European Journal, 23*(33), 7841-7852.

Kretzschmar, R., & Schafer, T. (2005). Metal Retention and Transport on Colloidal Particles in the Environment. *Elements, 1*(4), 205-210.

Kügler, S., Cooper, R. E., Wegner, C.-E., Mohr, J. F., Wichard, T., & Küsel, K. (2019). Iron-Organic Matter Complexes Accelerate Microbial Iron Cycling in an Iron-Rich Fen. *Science of The Total Environment, 646*, 972-988.

Kuhlman, K., Martens, R., Kelly, T., Evans, N., & Miller, M. (2001). Fabrication of Specimens of Metamorphic Magnetite Crystals for Field Ion Microscopy and Atom Probe Microanalysis. *Ultramicroscopy, 89*(1-3), 169-176.

Kulmala, M., Petäjä, T., Ehn, M., Thornton, J., Sipilä, M., Worsnop, D., & Kerminen, V.-M. (2014). Chemistry of Atmospheric Nucleation: On the Recent Advances on Precursor Characterization and Atmospheric Cluster Composition in Connection with Atmospheric New Particle Formation. *Annual Review of Physical Chemistry, 65*, 21-37.

Lair, G., Gerzabek, M., & Haberhauer, G. (2007). Sorption of Heavy Metals on Organic and Inorganic Soil Constituents. *Environmental Chemistry Letters, 5*(1), 23-27.

Lanteigne, S., Schindler, M., & McDonald, A. (2014). Distribution of Metals and Metalloids in Smelter-Derived Particulate Matter in Soils and Mineralogical Insights into Their Retention and Release in a Low-T Environment. *The Canadian Mineralogist, 52*(3), 453-471.

Lanteigne, S., Schindler, M., McDonald, A. M., Skeries, K., Abdu, Y., Mantha, N. M., Murayama, M., Hawthorne, F. C., & Hochella, M. F. (2012). Mineralogy and Weathering of Smelter-

Derived Spherical Particles in Soils: Implications for the Mobility of Ni and Cu in the Surficial Environment. *Water, Air, & Soil Pollution, 223*(7), 3619-3641.

Larson, D. J., Prosa, T., Ulfig, R. M., Geiser, B. P., & Kelly, T. F. (2013). Local Electrode Atom Probe Tomography. *New York, US: Springer Science, 2*.

Leo, R. F., & Barghoorn, E. S. (1976). Silicification of Wood. *Botanical Museum Leaflets, Harvard University, 25*(1), 1-47.

Li, W., Zhang, S., Jiang, W., & Shan, X.-q. (2006). Effect of Phosphate on the Adsorption of Cu and Cd on Natural Hematite. *Chemosphere, 63*(8), 1235-1241.

Liyanage, D., Thamali, R. J., Kumbalatara, A., Weliwita, J., & Witharana, S. (2016). An Analysis of Nanoparticle Settling Times in Liquids. *Journal of Nanomaterials, 2016*.

Manceau, A., & Matynia, A. (2010). The Nature of Cu Bonding to Natural Organic Matter. *Geochimica et Cosmochimica Acta, 74*(9), 2556-2580.

Mantha, H., Schindler, M., & Hochella, M. F. (2019). Occurrence and Formation of Incidental Metallic Cu and Cus Nanoparticles in Organic-Rich Contaminated Surface Soils in Timmins, Ontario. *Environmental Science: Nano, 6*(1), 163-179.

Mantha, N. M., Schindler, M., Murayama, M., & Hochella Jr, M. F. (2012). Silica-and Sulfate-Bearing Rock Coatings in Smelter Areas: Products of Chemical Weathering and Atmospheric Pollution I. Formation and Mineralogical Composition. *Geochimica et Cosmochimica Acta, 85*, 254-274.

Masson, S., Couillard, Y., Campbell, P. G., Olsen, C., Pinel-Alloul, B., & Perceval, O. (2010). Responses of Two Sentinel Species (Hexagenia Limbata—Mayfly; Pyganodon Grandis—Bivalve) Along Spatial Cadmium Gradients in Lakes and Rivers in Northwestern Québec. *Journal of Environmental Monitoring, 12*(1), 143-158.

Maurer, F., Christl, I., Fulda, B., Voegelin, A., & Kretzschmar, R. (2013). Copper Redox Transformation and Complexation by Reduced and Oxidized Soil Humic Acid. 2. Potentiometric Titrations and Dialysis Cell Experiments. *Environmental science & technology, 47*(19), 10912-10921.

Merikanto, J., Spracklen, D., Mann, G., Pickering, S., & Carslaw, K. (2009). Impact of Nucleation on Global Ccn. *Atmospheric Chemistry and Physics, 9*(21), 8601-8616.

Michel, F. M., Barrón, V., Torrent, J., Morales, M. P., Serna, C. J., Boily, J.-F., Liu, Q., Ambrosini, A., Cismasu, A. C., & Brown, G. E. (2010). Ordered Ferrimagnetic Form of Ferrihydrite

Reveals Links among Structure, Composition, and Magnetism. *Proceedings of the National Academy of Sciences, 107*(7), 2787-2792.

Miller, M., & Russell, K. (1992). An Apfim Investigation of a Weathered Region of the Santa Catharina Meteorite. *Surface Science, 266*(1-3), 441-445.

Montalvo, S. D., Reddy, S. M., Saxey, D. W., Rickard, W. D., Fougerouse, D., Quadir, Z., & Johnson, T. E. (2019). Nanoscale Constraints on the Shock-Induced Transformation of Zircon to Reidite. *Chemical Geology, 507*, 85-95.

Mukherjee, S., Watanabe, H., Isheim, D., Seidman, D. N., & Moutanabbir, O. (2016). Laser-Assisted Field Evaporation and Three-Dimensional Atom-by-Atom Mapping of Diamond Isotopic Homojunctions. *Nano Letters, 16*(2), 1335-1344.

Mustoe, G. E. (2017). Wood Petrifaction: A New View of Permineralization and Replacement. *Geosciences, 7*(4), 119.

Navrotsky, A., Ma, C., Lilova, K., & Birkner, N. (2010). Nanophase Transition Metal Oxides Show Large Thermodynamically Driven Shifts in Oxidation-Reduction Equilibria. *Science, 330*(6001), 199-201.

Navrotsky, A., Mazeina, L., & Majzlan, J. (2008). Size-Driven Structural and Thermodynamic Complexity in Iron Oxides. *Science, 319*(5870), 1635-1638.

Neagoe, A., Iordache, V., & Fărcăşanu, I. C. (2012). The Role of Organic Matter in the Mobility of Metals in Contaminated Catchments *Bio-Geo Interactions in Metal-Contaminated Soils* (pp. 297-325): Springer.

Nguyen, M., Picardal, F., Dultz, S., Nguyen-Thanh, L., Dam, T., & Nguyen, K. (2017a). Effect of Silicic Acid on the Aggregation Properties of Goethite. *European Journal of Soil Science, 68*(5), 650-657.

Nguyen, M. N., Picardal, F., Dultz, S., Dam, T. T., Nguyen, A. V., & Nguyen, K. M. (2017b). Silicic Acid as a Dispersibility Enhancer in a Fe-Oxide-Rich Kaolinitic Soil Clay. *Geoderma, 286*, 8-14.

Noiriel, C., Steefel, C. I., Yang, L., & Bernard, D. (2016). Effects of Pore-Scale Precipitation on Permeability and Flow. *Advances in Water Resources, 95*, 125-137.

O'Neill, H. S. C., & Navrotsky, A. (1983). Simple Spinels; Crystallographic Parameters, Cation Radii, Lattice Energies, and Cation Distribution. *American Mineralogist, 68*(1-2), 181-194.

Palansooriya, K. N., Shaheen, S. M., Chen, S. S., Tsang, D. C., Hashimoto, Y., Hou, D., Bolan, N. S., Rinklebe, J., & Ok, Y. S. (2020). Soil Amendments for Immobilization of Potentially Toxic Elements in Contaminated Soils: A Critical Review. *Environment International, 134*, 105046.

Perea, D. E., Arslan, I., Liu, J., Ristanović, Z., Kovarik, L., Arey, B. W., Lercher, J. A., Bare, S. R., & Weckhuysen, B. M. (2015). Determining the Location and Nearest Neighbours of Aluminium in Zeolites with Atom Probe Tomography. *Nature Communications, 6*(1), 1-8.

Pérez-Huerta, A., & Laiginhas, F. (2018). Preliminary Data on the Nanoscale Chemical Characterization of the Inter-Crystalline Organic Matrix of a Calcium Carbonate Biomineral. *Minerals, 8*(6), 223.

Pham, A. N., Rose, A. L., & Waite, T. D. (2012). Kinetics of Cu (Ii) Reduction by Natural Organic Matter. *The Journal of Physical Chemistry A, 116*(25), 6590-6599.

Philippe, T., Cojocaru-Mirédin, O., Duguay, S., & Blavette, D. (2010). Clustering and Nearest Neighbour Distances in Atom Probe Tomography: The Influence of the Interfaces. *Journal of Microscopy, 239*(1), 72-77.

Plathe, K., von Der Kammer, F., Hassellöv, M., Moore, J., Murayama, M., Hofmann, T., & Hochella, M. (2010). Using Flfff and Atem to Determine Trace Metal–Nanoparticle Associations in Riverbed Sediment. *Environmental Chemistry, 7*(1), 82-93.

Plecis, A., Schoch, R. B., & Renaud, P. (2005). Ionic Transport Phenomena in Nanofluidics: Experimental and Theoretical Study of the Exclusion-Enrichment Effect on a Chip. *Nano Letters, 5*(6), 1147-1155.

Putnis, A. (2015). Transient Porosity Resulting from Fluid–Mineral Interaction and Its Consequences. *Reviews in Mineralogy and Geochemistry, 80*(1), 1-23.

Rancourt, D., & Meunier, J.-F. (2008). Constraints on Structural Models of Ferrihydrite as a Nanocrystalline Material. *American Mineralogist, 93*(8-9), 1412-1417.

Reddy, S. M., Saxey, D. W., Rickard, W. D., Fougerouse, D., Montalvo, S. D., Verberne, R., & Van Riessen, A. (2020). Atom Probe Tomography: Development and Application to the Geosciences. *Geostandards and Geoanalytical Research, 44*(1), 5-50.

Reinhard, D. A., Laiginhas, F., Martens, R. L., & Prosa, T. J. (2016). Atom Probe Tomography (Apt) of Carbonate Minerals. *Micron*.

Rout, S. S., Heck, P. R., Isheim, D., Stephan, T., Zaluzec, N. J., Miller, D. J., Davis, A. M., & Seidman, D. N. (2017). Atom-Probe Tomography and Transmission Electron Microscopy of the Kamacite–Taenite Interface in the Fast-Cooled Bristol Iva Iron Meteorite. *Meteoritics & Planetary Science, 52*(12), 2707-2729.

Rozan, T. F., Lassman, M. E., Ridge, D. P., & Luther, G. W. (2000). Evidence for Iron, Copper and Zinc Complexation as Multinuclear Sulphide Clusters in Oxic Rivers. *Nature, 406*(6798), 879-882.

Rzepa, G., Pieczara, G., Gaweł, A., Tomczyk, A., & Zalecki, R. (2016). The Influence of Silicate on Transformation Pathways of Synthetic 2-Line Ferrihydrite. *Journal of Thermal Analysis and Calorimetry, 125*(1), 407-421.

Sansom, M. S., & Biggin, P. C. (2001). Water at the Nanoscale. *Nature, 414*(6860), 157-159.

Saxey, D., Moser, D., Piazolo, S., Reddy, S., & Valley, J. (2018). Atomic Worlds: Current State and Future of Atom Probe Tomography in Geoscience. *Scripta Materialia, 148*, 115-121.

Schindler, M., Durocher, J. L., Abdu, Y., & Hawthorne, F. C. (2009). Hydrous Silica Coatings: Occurrence, Speciation of Metals, and Environmental Significance. *Environmental Science & technology, 43*(23), 8775-8780.

Schindler, M., & Hochella, M. F. (2017). Sequestration of Pb–Zn–Sb-and as-Bearing Incidental Nanoparticles by Mineral Surface Coatings and Mineralized Organic Matter in Soils. *Environmental Science: Processes & Impacts, 19*(8), 1016-1027.

Schindler, M., Lanteigne, S., McDonald, A. M., & Hochella Jr, M. F. (2016). Evidence of Cu-and Ni-Bearing Surface Precipitates and Adsorption Complexes in Remediated Soils at the Nanoscale: A Tem, Micro-Raman, and Laser-Ablation Icp-Ms Study of Mineral Surface Coatings. *The Canadian Mineralogist, 54*(1), 285-309.

Schindler, M., Mantha, H., & Hochella, M. F. (2019). The Formation of Spinel-Group Minerals in Contaminated Soils: The Sequestration of Metal (Loid) S by Unexpected Incidental Nanoparticles. *Geochemical Transactions, 20*(1), 1.

Schirhagl, R., Raatz, N., Meijer, J., Markham, M., Gerstl, S. S., & Degen, C. L. (2015). Nanometer-Scale Isotope Analysis of Bulk Diamond by Atom Probe Tomography. *Diamond and Related Materials, 60*, 60-65.

Schmidt, J. E., Ye, X., van Ravenhorst, I. K., Oord, R., Shapiro, D. A., Yu, Y. S., Bare, S. R., Meirer, F., Poplawsky, J. D., & Weckhuysen, B. M. (2019). Probing the Location and

Speciation of Elements in Zeolites with Correlated Atom Probe Tomography and Scanning Transmission X-Ray Microscopy. *ChemCatChem, 11*(1), 488.

Šepelák, V., Becker, S. M., Bergmann, I., Indris, S., Scheuermann, M., Feldhoff, A., Kübel, C., Bruns, M., Stürzl, N., & Ulrich, A. S. (2012). Nonequilibrium Structure of Zn 2 Sno 4 Spinel Nanoparticles. *Journal of Materials Chemistry, 22*(7), 3117-3126.

Seydoux-Guillaume, A.-M., Fougerouse, D., Laurent, A., Gardés, E., Reddy, S., & Saxey, D. (2019). Nanoscale Resetting of the Th/Pb System in an Isotopically-Closed Monazite Grain: A Combined Atom Probe and Transmission Electron Microscopy Study. *Geoscience Frontiers, 10*(1), 65-76.

Shannon, R. D. (1976). Revised Effective Ionic Radii and Systematic Studies of Interatomic Distances in Halides and Chalcogenides. *Acta crystallographica section A: crystal physics, diffraction, theoretical and general crystallography, 32*(5), 751-767.

Siponen, M. I., Legrand, P., Widdrat, M., Jones, S. R., Zhang, W.-J., Chang, M. C., Faivre, D., Arnoux, P., & Pignol, D. (2013). Structural Insight into Magnetochrome-Mediated Magnetite Biomineralization. *Nature, 502*(7473), 681-684.

Smykatz-Kloss, W., Heide, K., & Klinke, W. (2003). Applications of Thermal Methods in the Geosciences. *Handbook of Thermal Analysis and Calorimetry, 2*, 451-594.

Stack, A. G. (2015). Precipitation in Pores: A Geochemical Frontier. *Reviews in Mineralogy and Geochemistry, 80*(1), 165-190.

Stack, A. G., Fernandez-Martinez, A., Allard, L. F., Bañuelos, J. L., Rother, G., Anovitz, L. M., Cole, D. R., & Waychunas, G. A. (2014). Pore-Size-Dependent Calcium Carbonate Precipitation Controlled by Surface Chemistry. *Environmental Science & Technology, 48*(11), 6177-6183.

Steinmann, P., & Shotyk, W. (1995). Ion Chromatography of Organic-Rich Natural Waters from Peatlands V. Fe2+ and Fe3+. *Journal of Chromatography A, 706*(1-2), 293-299.

Strawn, D. G., & Baker, L. L. (2007). Speciation of Cu in a Contaminated Agricultural Soil Measured by Xafs, M-Xafs, and M-Xrf. *Environmental Science & Technology, 42*(1), 37-42.

Taylor, S. D., Liu, J., Zhang, X., Arey, B. W., Kovarik, L., Schreiber, D. K., Perea, D. E., & Rosso, K. M. (2019). Visualizing the Iron Atom Exchange Front in the Fe (Ii)-Catalyzed

Recrystallization of Goethite by Atom Probe Tomography. *Proceedings of the National Academy of Sciences, 116*(8), 2866-2874.

Telmer, K. H., Daneshfar, B., Sanborn, M. S., Kliza-Petelle, D., & Rancourt, D. G. (2006). The Role of Smelter Emissions and Element Remobilization in the Sediment Chemistry of 99 Lakes around the Horne Smelter, Quebec. *Geochemistry: Exploration, Environment, Analysis, 6*(2-3), 187-202.

Tester, C. C., Wu, C.-H., Weigand, S., & Joester, D. (2012). Precipitation of Acc in Liposomes—a Model for Biomineralization in Confined Volumes. *Faraday Discussions, 159*, 345-356.

Thanh, N. T., Maclean, N., & Mahiddine, S. (2014). Mechanisms of Nucleation and Growth of Nanoparticles in Solution. *Chemical Reviews, 114*(15), 7610-7630.

Thomasi, S., Fernandes, R., Fontes, R., & Jordão, C. (2015). Sequential Extraction of Copper, Nickel, Zinc, Lead and Cadmium from Brazilian Oxysols: Metal Leaching and Metal Distribution in Soil Fractions. *International Journal of Environmental Studies, 72*(1), 41-55.

Thompson, A., & Goyne, K. (2012). Introduction to the Sorption of Chemical Constituents in Soils. *Nature Education Knowledge, 4*(4), 7.

Tiberg, C., Sjöstedt, C., Persson, I., & Gustafsson, J. P. (2013). Phosphate Effects on Copper (Ii) and Lead (Ii) Sorption to Ferrihydrite. *Geochimica et Cosmochimica Acta, 120*, 140-157.

Van Driessche, A. E., Kellermeier, M., Benning, L. G., & Gebauer, D. (2016). *New Perspectives on Mineral Nucleation and Growth: From Solution Precursors to Solid Materials*: Springer.

Verwey, E. J. W., Overbeek, J. T. G., & Van Nes, K. (1948). *Theory of the Stability of Lyophobic Colloids: The Interaction of Sol Particles Having an Electric Double Layer*: Elsevier Publishing Company.

Wang, M., Dissanayake, T. U., Park, C., Gaskell, K., & Woehl, T. J. (2019). Nanoscale Mapping of Nonuniform Heterogeneous Nucleation Kinetics Mediated by Surface Chemistry. *Journal of the American Chemical Society, 141*(34), 13516-13524.

Wang, Y. (2014). Nanogeochemistry: Nanostructures, Emergent Properties and Their Control on Geochemical Reactions and Mass Transfers. *Chemical Geology, 378*, 1-23.

Weber, F.-A., Voegelin, A., Kaegi, R., & Kretzschmar, R. (2009). Contaminant Mobilization by Metallic Copper and Metal Sulphide Colloids in Flooded Soil. *Nature Geoscience, 2*(4), 267-271.

Weber, J. (2017). *Fundamental Insights into the Radium Uptake into Barite by Atom Probe Tomography and Electron Microscopy*: Forschungszentrum Jülich GmbH, Zentralbibliothek.

Weber, J., Barthel, J., Brandt, F., Klinkenberg, M., Breuer, U., Kruth, M., & Bosbach, D. (2016). Nano-Structural Features of Barite Crystals Observed by Electron Microscopy and Atom Probe Tomography. *Chemical Geology, 424*, 51-59.

Wu, Y.-F., Fougerouse, D., Evans, K., Reddy, S. M., Saxey, D. W., Guagliardo, P., & Li, J.-W. (2019). Gold, Arsenic, and Copper Zoning in Pyrite: A Record of Fluid Chemistry and Growth Kinetics. *Geology, 47*(7), 641-644.

Yang, L., & Garde, S. (2007). Modeling the Selective Partitioning of Cations into Negatively Charged Nanopores in Water. *The Journal of chemical physics, 126*(8), 084706.

Yang, Y., Colman, B. P., Bernhardt, E. S., & Hochella, M. F. (2015). Importance of a Nanoscience Approach in the Understanding of Major Aqueous Contamination Scenarios: Case Study from a Recent Coal Ash Spill. *Environmental Science & Technology, 49*(6), 3375-3382.

Yao, T., Sun, Z., Li, Y., Pan, Z., Wei, H., Xie, Y., Nomura, M., Niwa, Y., Yan, W., & Wu, Z. (2010). Insights into Initial Kinetic Nucleation of Gold Nanocrystals. *Journal of the American Chemical Society, 132*(22), 7696-7701.

Yongvanich, N., Visuttpitukul, P., Assawasilpakul, W., Srichan, W., & Sungsuwan, N. (2012). *Fabrication of Sn-Doped Zno Varistor by Solid State Processing.* Paper presented at the Applied Mechanics and Materials.

Zdanowicz, C. M., Banic, C. M., Paktunc, D. A., & Kliza-Petelle, D. A. (2006). Metal Emissions from a Cu Smelter, Rouyn-Noranda, Quebec: Characterization of Particles Sampled in Air and Snow. *Geochemistry: Exploration, Environment, Analysis, 6*(2-3), 147-162.

Zhang, H., De Yoreo, J. J., & Banfield, J. F. (2014). A Unified Description of Attachment-Based Crystal Growth. *ACS nano, 8*(7), 6526-6530.

Zhao, J., Huggins, F. E., Feng, Z., & Huffman, G. P. (1994). Ferrihydrite: Surface Structure and Its Effects on Phase Transformation. *Clays and Clay Minerals, 42*(6), 737-746.

Chapter 4: Conclusion and Recommendations of future work

4.1. Conclusion

This thesis shows that only nano-scale techniques can resolve mineralogical and chemical details on the occurrence of Cu and Fe in OM colloids and particles within contaminated oxic soils. It specifically demonstrates that identified sequestration mechanisms for Cu in organic-rich soils could be only deciphered using a combination of bulk and nano-scale analytical techniques. Hence, the characterization of OM through a combination of TEM and APT provide valuable insights into geochemical and mineralogical processes related to the formation of metal(loid)-bearing NP and their respective precursors within OM.

This study shows that the formation of Cu-bearing incidental NP within OM is a very intricate process and is primarily controlled by the pre-mineralization of OM, which generates porosity along exterior surfaces and cracks throughout the OM. Porosity promotes diffusion of metal(loid) species and silicates/silica provide favorable surfaces for the formation of NP within nanopore spaces. Hydrophobic functional groups of OM and hydrodynamic properties of pore channels most likely have a strong control over the diffusion of metal(loid) species. Furthermore, availability of silica/silicates, distribution of polar functional groups in OM, availability of metal(loid) aqueous species and pore size controlled solubility effects most likely promote the formation of metal(loid)-bearing NP and their precursors (which are revealed by the APT data) in OM. Non-conventional models of nucleation such as crystallization through particle attachment and Ostwald ripening have not been observed in the interior of organic colloids but appear to dominate in OM particles. CuS_x phases occur predominantly within organic colloids and their limited occurrence in OM particles may be attributed to a limited availability of sulfide species.

4.2. Application of study

This study highlights the importance of porous materials such as organic colloids and particles in the sequestration of metal(loid)s as well as their ability to promote nucleation and long-term stability of secondary metal(loid)-bearing mineralogical phases in surficial soils. Therefore, this study advocates the use of porous material such as biochar for the remediation of soils contaminated with toxic metal(loid)s, especially if biochar containing selectively confined pores

of specific size can be manufactured. Biochar has a carbon matrix with extensive surface area and high degree of porosity, allowing it to be used as sorbent for metal(loid)s (Chen et al., 2003; Beesley et al., 2011). Biochar is mostly derived from animal wastes and has high sorption capacity due to overall negative surface charge of the carbon matrix, a high ion exchange capacity and sorptive interactions induced by delocalized electrons (Cao et al., 2009; Sohi et al., 2010). Many studies have been conducted on the sorption of metal(loid)s on the biochar and its use as organic amendment to contaminated soils; however, its role in sequestration of metal(loid)s and formation of secondary metal(loid)-bearing mineralogical phase in its micro and nano pores still needs to be addressed by experimental studies. The latter studies may reveal how specific pore sizes can enhance the uptake of metal(loid)s by biochar and promote thus their long term immobilization. Physico-chemical properties of biochar such as pH, ion exchange capacity, surface area and size of matrix pores depend on the temperature of pyrolysis during its production (Yuan et al., 2013; Zhao et al., 2018). Therefore, this temperature can be adjusted to produce biochar with enhanced capacities to sequester metal(loid)s in contaminated surficial soils.

4.3. Future Work

Schindler & Hochella Jr (2015) showed that metal(loid)-rich phases can be preserved in low-accessible pore spaces over several decades. Their observations and the findings of this study suggest that Cu-bearing phases may remain unaffected by major changes in soil pH and soil composition when incorporated in pore spaces of OM. Hence, soil reclamation techniques such as liming, fertilization or the addition of organic amendments may not immediately affect the entire mineralogy of Cu in contaminated soils.

The identification of Cu-bearing incidental NP and their precursors in porous OM or secondary alteration products may impact how we approach future studies on the fate of Cu and other metal(loid)s in contaminated soils. For example, a combination of bulk analytical techniques, synchrotron-based spectroscopy, TEM and APT may provide a complete overview on various sequestration mechanisms for metal(loid)s in an impacted soil on the regional rather than on the centimeter scale (as conducted in this study).

Finally, I recommend that experimental studies should be carried out in order to better understand the formation of metal(loid)-rich phases in porous constituents of soils and sediments. These studies should use for example mesoporous silica or organic matter with known pore-size

dimensions to identify pore-size induced effects on the diffusion of metal(loid) aqueous species and the nucleation of metal(loid)-bearing NP.

4.4. References

Beesley, L., Moreno-Jiménez, E., Gomez-Eyles, J. L., Harris, E., Robinson, B., & Sizmur, T. (2011). A Review of Biochars' Potential Role in the Remediation, Revegetation and Restoration of Contaminated Soils. *Environmental Pollution, 159*(12), 3269-3282.

Cao, X., Ma, L., Gao, B., & Harris, W. (2009). Dairy-Manure Derived Biochar Effectively Sorbs Lead and Atrazine. *Environmental Science & Technology, 43*(9), 3285-3291.

Chen, X. Y., Shi, W., Cheng, P., Chen, J. T., Yan, S. P., Liao, D. Z., & Jiang, Z. H. (2003). Multi-Dimensional Copper (Ii) Coordination Polymers Via Self-Assembly Induced by Sodium Ions. *Zeitschrift für anorganische und allgemeine Chemie, 629*(11), 2034-2039.

Schindler, M., & Hochella Jr, M. F. (2015). Soil Memory in Mineral Surface Coatings: Environmental Processes Recorded at the Nanoscale. *Geology, 43*(5), 415-418.

Sohi, S. P., Krull, E., Lopez-Capel, E., & Bol, R. (2010). A Review of Biochar and Its Use and Function in Soil. *Advances in Agronomy, 105*, 47-82.

Yuan, H., Lu, T., Zhao, D., Huang, H., Noriyuki, K., & Chen, Y. (2013). Influence of Temperature on Product Distribution and Biochar Properties by Municipal Sludge Pyrolysis. *Journal of Material Cycles and Waste Management, 15*(3), 357-361.

Zhao, H., Li, Q., & Tao, J. (2018). Distribution Characteristic of Total Bacterioplankton and Environmental Influence Factors in Bohai Bay. *Water Resour Protect, 34*(5), 88-94.

Appendices

Appendix A: Chapter 2

Supplementary Information

Materials and methods

Sample preparation and Bulk Analytical Techniques

All collected samples were taken back to the lab in sealed plastic bags (circa 4 hours' drive), sieved (< 1.4 mm), dried in an oven at 80°C for three days and stored under dry conditions for further examinations.

The pH value of the soil samples was measured by mixing 2 g of soil with 10 mL of a 0.01 M $CaCl_2$ solution (OECD, 2002). The mixture was thoroughly stirred for 30 minutes and allowed to settle for 15 minutes before the pH measurement. Total carbon and sulfur of the samples 5A, 7A and 7B were measured in the Ontario Geological Survey Geoscience Laboratories (Geo Labs) with a LECO CS844. This analysis was conducted by combustion of 0.2g of soil in a stream of purified O2 gas and later passed over a heated catalyst, oxidizing total S and C to SO_2 and CO_2, respectively, which are then detected by two non-dispersive infrared cells (Amirault & Burnham, 2013). The soil digestion process and inductively coupled plasma-mass spectrometry (ICP-MS) measurements of the soil fractions were conducted at the Geo Labs, Sudbury, ON, Canada. Samples were prepared in a reverse aqua-regia digest following the Burnham method (Burnham, 2017) and analyzed with an iCAP Q ICP-MS (Thermo Scientific).

Powder X-ray diffraction (XRD) analysis was conducted at the Pacific North West National Laboratory with an automated Bruker D8 diffractometer using of Cu Kα radiation (1.5417 Å) at a current and voltage of 30 mA and 40 kV, respectively. The XRD patterns were collected from 10° 2θ to 110° 2θ with a step size and dwell time of 0.02° 2θ and 2s (2.7 hours), respectively.

Colloid sample preparation and TEM

Column leaching experiments were conducted to collect soil leachates by filling hollow, plastic tubes with approximately 2 g of the dried and sieved (<1.4 mm) 3 cm soil fraction which was covered on the top and bottom by a small layer of plastic beads (Figure 2-2b). A 0.02 mM $CaCl_2$ solution was passed through the leaching column at an approximate rate of 0.8 mL h^{-1} until

50 mL was collected in a flask below the column. A fraction of the leachate was centrifuged using a Beckman Coulter Max-Ultracentrifuge centrifuge rotor 40000 rpm at 120 minutes, which, according to the Stokes equation, will remove all spherical particles from solution with a density similar to CuS (4.76 g cm^{-3}) and a diameter greater than 4.5 nm.

ICP-MS analysis was conducted on the original leachate after acidification (to determine the total concentration of metal(loid)s) and on the leachate after centrifugation/filtering (0.1 μm) (to determine the concentrations of metal(loid)s in the dissolved fraction. Samples were analyzed on an ICP-MS (Agilent 8900) instrument at the center of earth observation and science (CEOS) at the University of Manitoba. The proportion of each element in the colloidal fraction was then determined through subtraction of the dissolved fraction from the total fraction.

Determination of the size distribution of the colloids

The size of colloids was determined through the dynamic light scattering method, in which a laser pulse is fired in the solution and a reflected laser light signal is deconvoluted to determine the size distribution of the particles via Fast Fourier Transform (FFT) analysis. The leachates (non-centrifuged) of two samples, 5A and 7A were analyzed on a Microtrac nanotrac dynamic light scattering instrument at the Manitoba Institute of Materials.

TEM analysis of the colloids

To prepare the colloids for TEM analysis, soil leachates were centrifuged using a Beckman Coulter Max-Ultracentrifuge centrifuge equipped with a MLS 50 swing-bucket rotor. A molybdenum TEM grid (400 mesh lacey carbon, 100 μm) was fixed to an epoxy support at the bottom of the centrifuge tube and the tube was then filled with 2 mL of the leachate. According to Stokes equation, spherical particles greater than 4.5 nm and a density similar to CuS (4.76 g cm^{-3}) deposit onto the grid during centrifugation for 120 minutes at a speed of 40000 rpm. The deposited colloidal fraction on the TEM grid was examined with a field emission TEM FEI Talos F200x at the Manitoba Institute of Materials. SAED and TEM imaging was performed with an accelerating voltage of 200 kV in bright and dark field mode with a Fischione high angle annular dark field (HAADF) detector and a 16 MB Ceta camera. STEM-EDS mode was used to perform compositional analysis with 4 SDD detectors.

Figures:

Figure 2-S1: A photograph of site 7 with the smelter stack in the background

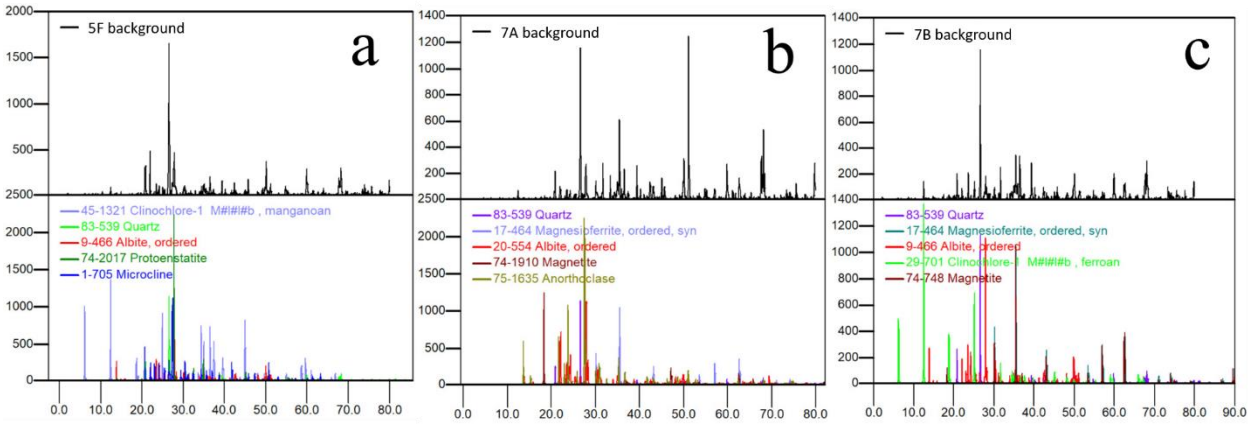

Figure 2-S2: (a, b and c) show the XRD patterns of samples 5A, 7A and 7B, respectively.

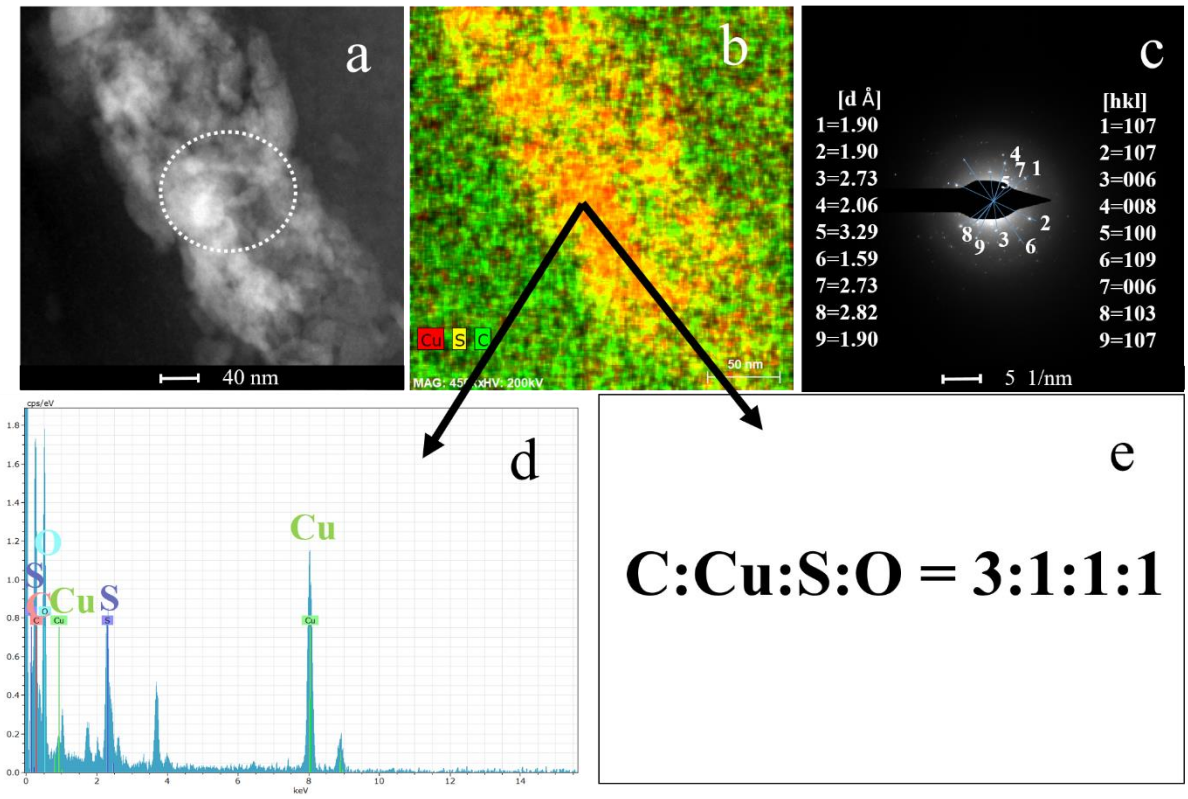

Figure 2-S3: Identification process of covellite: (a) STEM image and (b) STEM-EDS chemical distribution maps for Cu (red), S (yellow) and C (green); (c) selected area electron diffraction pattern (SAED) of area highlighted by white and black dashed lines in (a) indicating that all the of the observed d-spacings correspond to covellite. (d) STEM-EDS spectrum and (e) C, Cu, S and O ratio obtained from EDS spectrum indicating that C:Cu:S:O ratio corresponds to sulfide rather than sulfate as oxygen is associated with C, otherwise much more oxygen would have been present.

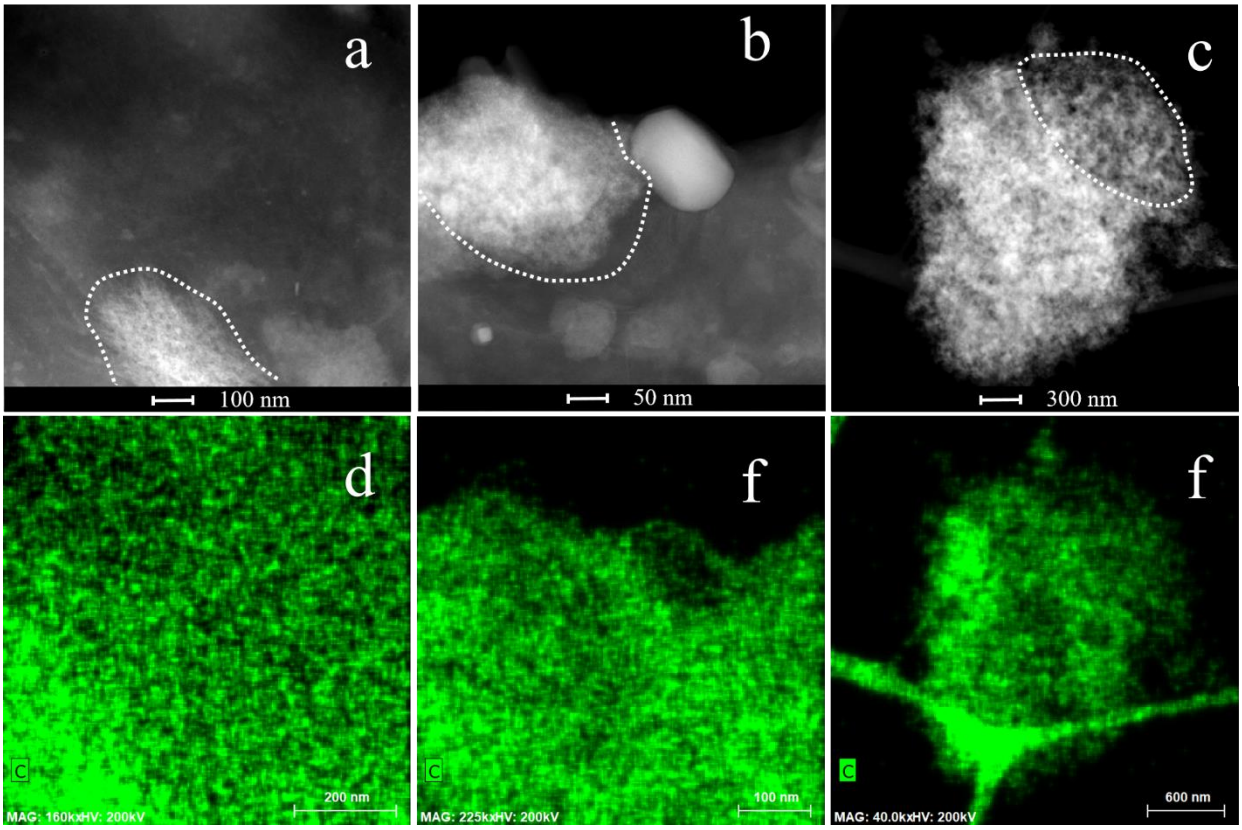

Figure 2-S4: Morphology of organic colloids: (a-c) STEM images and (d-f) STEM-EDS chemical distribution maps for C (green); (a-c) nanopores or porous zones are visible within organic colloids (highlighted with white dashed lines).

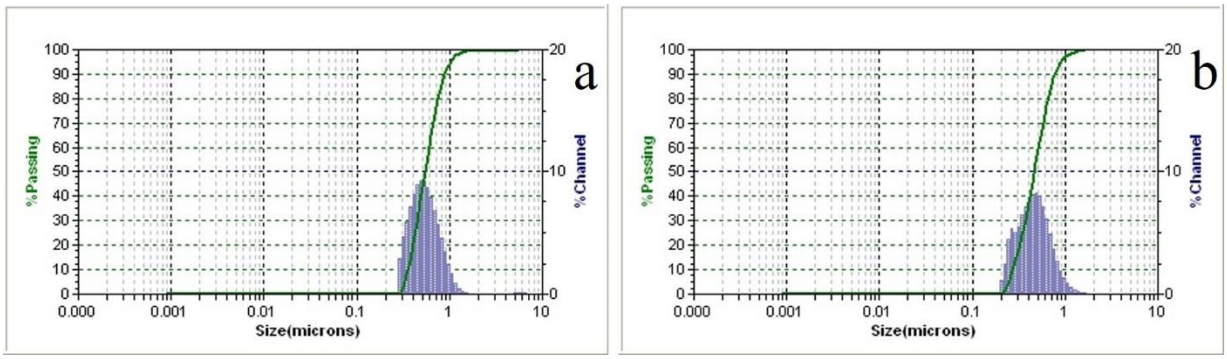

Figure 2-S5: Dynamic light scattering plots indicating the average particle size in samples (a) 5A and (b) 7A.

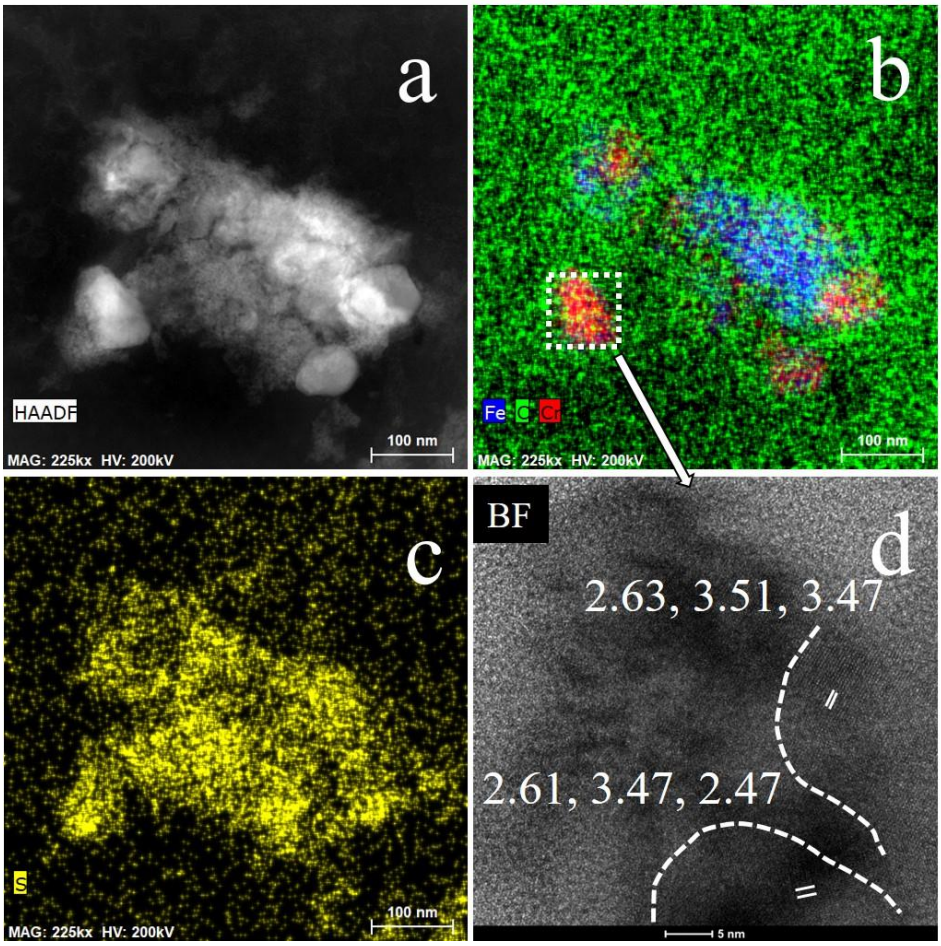

Figure 2-S6: (a)-(d) Almost euhedral Fe-Cr-sulfate NP located within organic colloids: (a) STEM image, (b) STEM-EDS chemical distribution maps for Fe (blue), Cr (red) and C (green) and (c) for S (yellow), (d) high-resolution TEM image indicating characteristic lattice fringes (highlighted with solid white lines) within nanodomains; all *d*-spacings are given in Å.

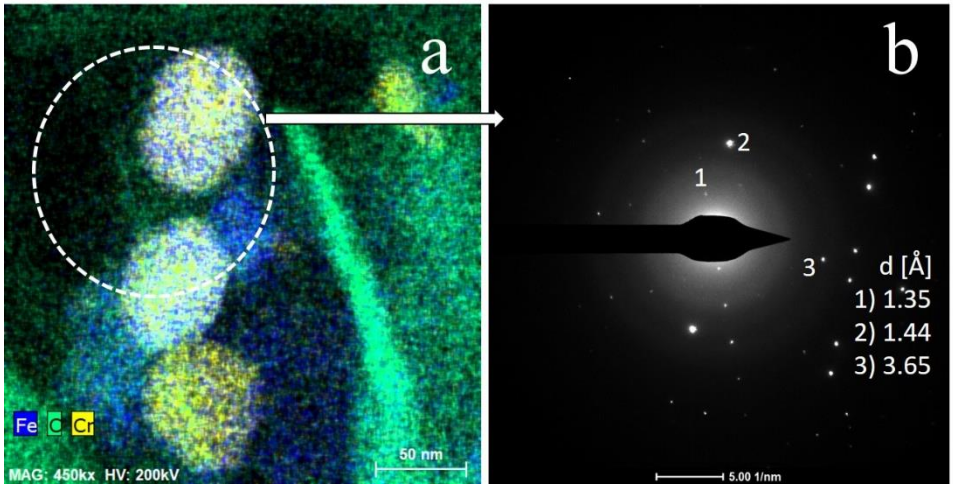

Figure 2-S7: (a)-(b) Almost euhedral Cr-bearing hematite (Hem) nanoparticles: (a) STEM-EDS chemical distribution maps for Fe (blue), Cr (yellow) and C (green) and (b) selected area diffraction pattern (SAED) of area highlighted by white dashed line in (a).

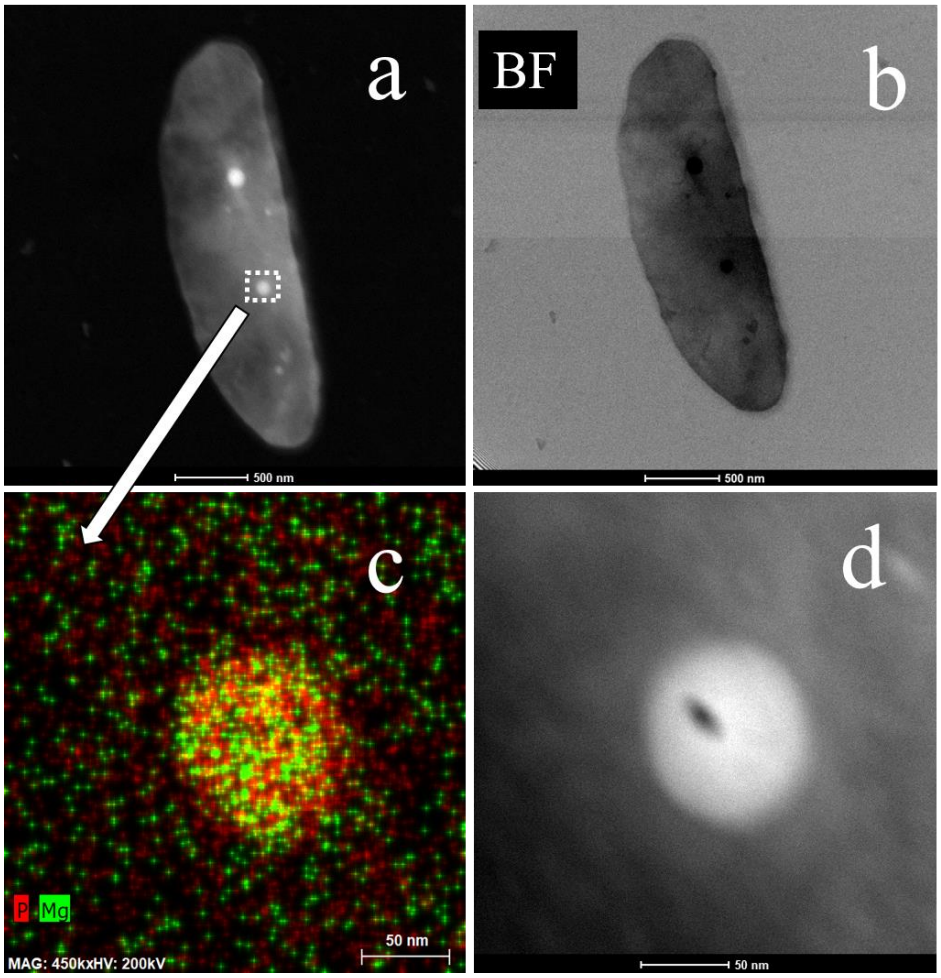

Figure 2-S8: (a)-(d) Possible calcium carbonate mineralized bacterium cell: (a and d) STEM images, (b) high resolution TEM image, (c) STEM-EDS chemical distribution map for P (red) and Mg (green) indicating the possible location of the former nucleus.

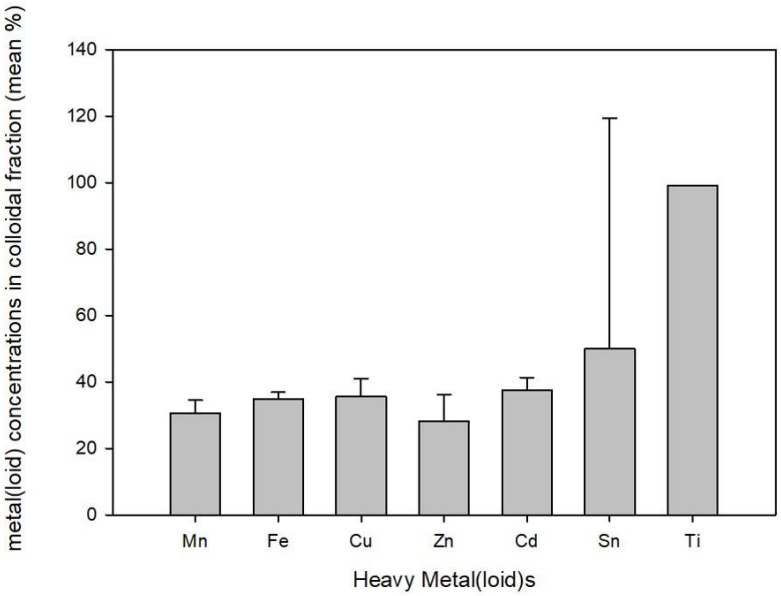

Figure 2-S9: shows the proportions of the metal(loid) in the colloidal fraction (mean %) with respect to their total concentrations in the leachate.

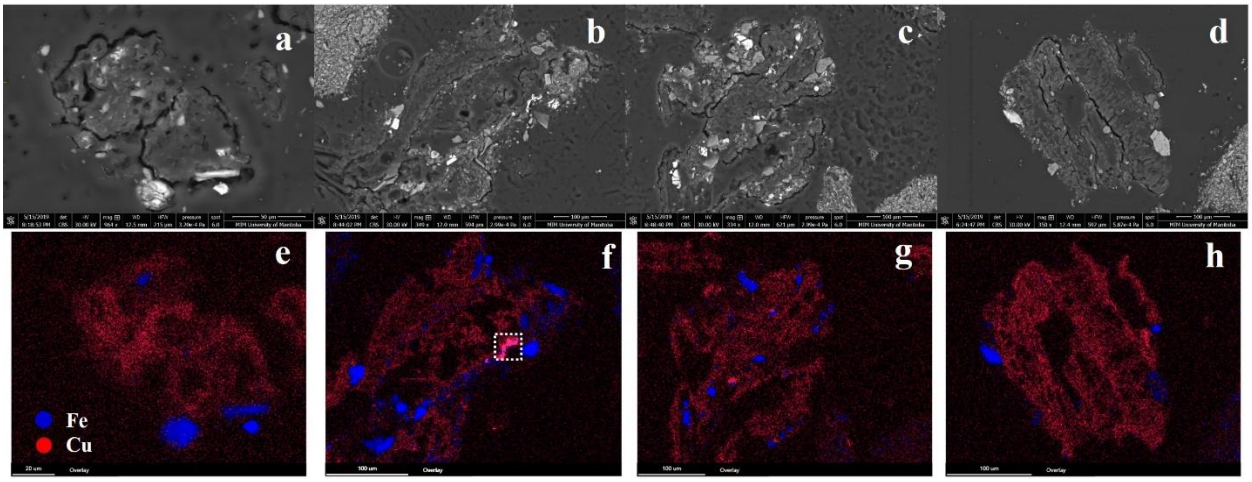

Figure 2-S10: (a-d) SEM images in backscattering mode (BSE) of organic particles from sample 5A and (e)-(h) their corresponding SEM-EDS chemical distribution maps for Fe (blue) and Si (red). The maps indicate that Cu is homogenously distributed within the OM particles, whereas Fe is concentrated within certain regions.

Tables:

Table 2-S1: Selected trace metal(loid) concentrations and physico-chemical parameters of the samples 5A, 7A and 7B.

	Trace metal concentration[a] (ppm)							Physico-chemical parameters			Distance to former smelter complex (km)
Sample	Ag	Co	Cu	Pb	Sb	Sn	Zn	pH	Total C (wt%)	Total S (wt %)	
5A	21.9	173.5	7974	3104.9	32.9	>90	1474.0	4.7	28.1	0.28	1.8 W
7A	7.4	184.1	2692	1261.9	48.9	>90	4225.0	5.4	22.0	0.19	1.8 NE
7B	7.2	88.0	3829	2023.9	42.6	>90	2178.0	3.6	22.8	0.37	1.8 NE

Table 2-S2: Trace metal(loid) concentrations in all collected samples around the Horne smelter in Rouyn Noranda.

	Trace metal concentration (ppm)							Distance to former smelter complex (Km)
Sample	Ag	Co	Cu	Pb	Sb	Sn	Zn	
1A	18.8	273.2	2864	1759.2	28.4	>90	263	3.5
1B	1.4	68.5	854	225.7	2.2	8.9	118	3.5
1C	19.2	143.1	4138	909.1	25.1	72.3	363	3.5
2A	5.1	295.5	5318	3825.8	26.1	>90	773	3.1
2B	2.6	154.4	789	377.8	4.8	21.5	83	3.1
2C	9.6	81.3	6120	2101.4	12.5	57.0	707	3.1
3A	8.8	124.6	2043	2166.3	13.7	>90	420	2.9
3B	2.7	122.6	1007	718.6	4.7	25.3	255	2.9
3C	1.4	274.8	523	175.9	2.1	7.9	516	2.9
4A	9.2	105.4	2853	601.6	12.9	29.1	656	2.9
4B	11.3	84.6	3419	835.6	14.6	36.1	507	2.9
4C	0.5	81.4	131	52.0	1.4	3.3	169	2.9
5A	21.9	173.5	7974	3104.9	32.9	>90	1474	1.8
5B	23.4	114.5	6916	1691.1	35.4	64.5	1521	1.8
6A	8.1	117.4	3421	494.7	10.1	24.8	615	1.2
6B	6.4	81.8	1740	926.6	15.6	32.4	246	1.2
6C	19.8	118.2	6535	1462.8	18.3	44.4	692	1.2
6F	12.8	99.2	3732	608.5	26.7	32.1	1154	1.2
7A	7.4	184.1	2692	1261.9	49.0	>90	4225	1.8
7B	7.3	88.0	3829	2023.9	42.6	>90	2178	1.8
7C	5.3	118.4	1903	875.1	38.9	>90	1480	1.8
Average	10	138	3276	1248	20	>50	887	

Table 2-S3: Carbon-nitrogen-sulfur concentrations in samples 7A, 7B and 5A; Carbon is measured as both Total carbon (TC) and Total organic content (TOC) in the analysis.

Sample	**Wt% N**	**Wt% TC**	**Wt% S**	**Wt%TOC**	**C/N**
7A	1.258	22.074	0.194	17.253	17.549
7B	1.258	22.822	0.365	18.784	15.317
5A	1.676	28.113	0.277	25.112	16.773

Table 2-S4: Selected trace metal(loid) concentrations in the colloidal fraction of samples 7A, 7B and 5A.

Sample	**Total concentration of selected metal(loid)s in the leachate (µg/L)**				
	Cd	Cu	Fe	Mn	Zn
7A	90	8220	5540	591	3183
7B	14	19047	18370	765	3712
5A	44	9889	1224	1496	2867

Table 2-S5: Proportion of metal(loid)s in the colloidal fractions with respect to their total concentrations in the leachates from samples 7A, 7B and 5A.

Sample	**Proportion of selected metal(loid)s in the colloidal fraction (%)**				
	Cd	Cu	Fe	Mn	Zn
7A	35	32	33	28	22
7B	40	40	36	33	34
5A	37	29	28	25	23

References:

Amirault, F., & Burnham, O. (2013). Carbon and Sulfur Analysis in Geological Samples by Combustion-Infrared: Verifying Method Capabilities on New Instrumentation. *Summary of Fieldwork and Other Activities 2013, Ontario Geological Survey Open File Report 6290*, 43-41.

Burnham, O. M. (2017). Inductively Coupled Plasma Mass Spectrometry Analysis of Trace Elements in Geological Samples after Aqua Regia Extraction at the Geoscience Laboratories: Revised Capabilities Resulting from New Instrumentation, in Summary of Field Work and Other Activities. *Open File Report 6333, Ontario Geological Survey*, 31.

OECD, D. (2002). Guidelines for the Testing of Chemicals: Leaching in Soil Columns: OECD-Organisation for Economic Cooperation and Development.

Appendix B: Chapter 3

Supplementary Information

Materials and methods

Sample preparation and Bulk Analytical Techniques

All collected samples were taken back to the lab in sealed plastic bags (circa 4 hours' drive), sieved (< 1.4 mm), dried in an oven at 80°C for three days and stored under dry conditions for further examinations.

The pH value of the soil samples was measured by mixing 2 g of soil with 10 mL of a 0.01 M $CaCl_2$ solution (OECD, 2002), The mixture was thoroughly stirred for 30 minutes and allowed to settle for 15 minutes before the pH measurement. Total carbon and sulfur of the samples 5A, 7A and 7B were measured in the Ontario Geological Survey Geoscience Laboratories (Geo Labs) with a LECO CS844. This analysis was conducted by combustion of 0.2g of soil in a stream of purified O_2 gas and later passed over a heated catalyst, oxidizing total S and C to SO_2 and CO_2, respectively, which are then detected by two non-dispersive infrared cells (Amirault & Burnham, 2013). The soil digestion process and inductively coupled plasma-mass spectrometry (ICP-MS) measurements of the soil fractions were conducted at the Geo Labs, Sudbury, ON, Canada. Samples were prepared in a reverse aqua-regia digest following the Burnham (2017) method and analyzed with an iCAP Q ICP-MS (Thermo Scientific).

Powder X-ray diffraction (XRD) analysis was conducted at the Pacific North West National Laboratory with an automated Bruker D8 diffractometer using of Cu Kα radiation (1.5417 Å) at a current and voltage of 30 mA and 40 kV, respectively. The XRD patterns were collected from 10° 2θ to 110° 2θ with a step size and dwell time of 0.02° 2θ and 2s, respectively.

Scanning electron microscopy (TEM)

Characterization of the chemical composition of organic particles was accomplished using scanning electron microscopy (SEM) with a Quanta 650 FEG Environmental SEM at Manitoba Institute of Materials, operating with an accelerating voltage of 15 kV and a beam current of 1 nA,

in combination with energy dispersive X-ray spectrometry (EDS). TEAMS software is used for the processing of chemical maps and spot analysis.

Transmission electron microscopy (TEM)

TEM-FIB-1 and TEM-FIB-2 were examined with a field emission TEM FEI Talos F200x at the Manitoba Institute of Materials. SAED and TEM imaging was performed with an accelerating voltage of 200 kV in bright and dark field mode with a Fischione high angle annular dark field (HAADF) detector and a 16 MB Ceta camera. STEM-EDS mode was used to perform chemical compositional analysis with 4 SDD detectors. TEM imaging and analysis software (v 4.15) is used to process the TEM and STEM images and to measure d-spacings through FFT (fast fourier transformation) analysis. Chemical composition analysis is conducted via esprit software (v 1.9).

Atom probe tomography (APT)

APT data acquisition

Atom probe tomographic analysis was conducted in a Cameca local-electrode atom-probe (LEAPXsi) tomograph using a pulsed laser (λ = 355nm, 160-500 kHz, 40-75 pJ per pulse). The ion evaporation rate was maintained between 0.0025-0.005 ions per laser pulse. The base temperature was maintained between 40 and 60 K with an ambient vacuum pressure <10-8 Pa. IVAS atom-probe data visualization and analysis software v 3.8.8 (Cameca) was used to perform the three-dimensional reconstructions of the APT data using published algorithms (Bas et al., 1995; Miller, 2012) and recommendations of Blum et al. (2018).

APT 2D iso-density plots and 3D rendering

Two-dimensional plots are created in IVAS (3.8.8) using a pixel size of 0.1 nm. Selective peaks are used in the mass to charge spectrum of the both APT-FIBs to minimize and avoid spectral overlaps (Figures 3-S3 and 3-S4). Therefore, some selected peaks might not represent the naturally abundant isotope of given metal(loid) species, for example, Na^{2+} is used instead of Na^{+} to avoid isobaric overlap. Sometimes only non-abundant isotopic species are identified in the mass-to-charge spectrum due to selected parameters of data acquisition. CO^{+} is not rendered due to the spectral overlap with $^{56}Fe^{2+}$. Similarly Si^{+2} peaks at 28 and 29 (Da) are not rendered due to spectral overlaps with Fe^{2+}.

Identification of metal(loid) bearing phases using TEM and STEM

The metal(loid)-bearing phases in the OM particles are identified based on a combination of d-spacings observed in selected area diffraction (SAED) pattern and high-resolution TEM (HRTEM) images (in combination with FFT pattern) and semi-quantitative chemical analyses determined with energy dispersive spectroscopy (EDS) analyses in Scanning TEM mode. In the absence of any structural information (no diffraction spots in SAED pattern or lattice fringes in HRTEM images), phases within OM particles are named based on their chemical composition (e.g. Fe-(hydr)oxide or Silicate).

Figures:

Figure 3-S1: Photographs of the organic-rich soils sampled at locations (a) 5A, (b) 7A and (c) 7B.

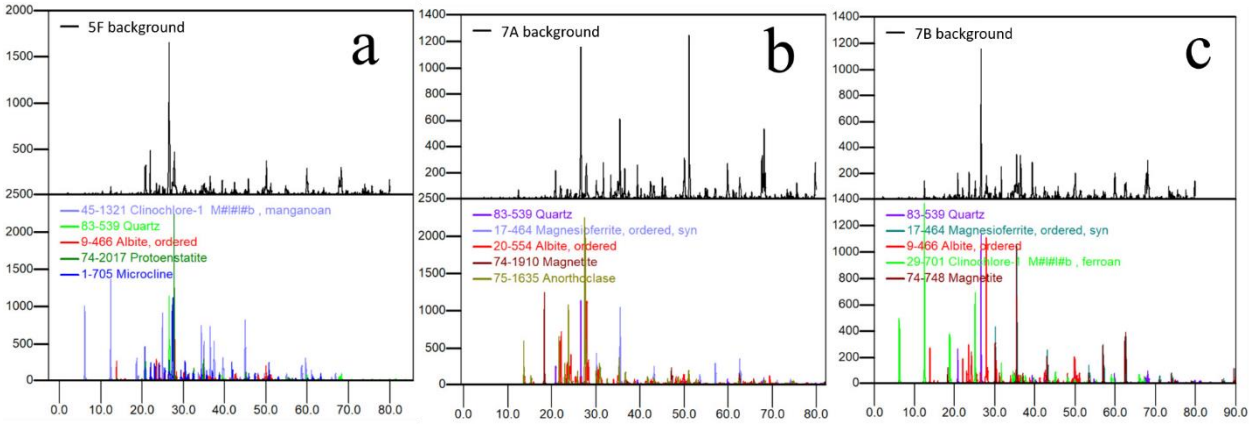

Fig 3-S2: (a, b and c) show the XRD patterns for the samples 5A, 7A and 7B.

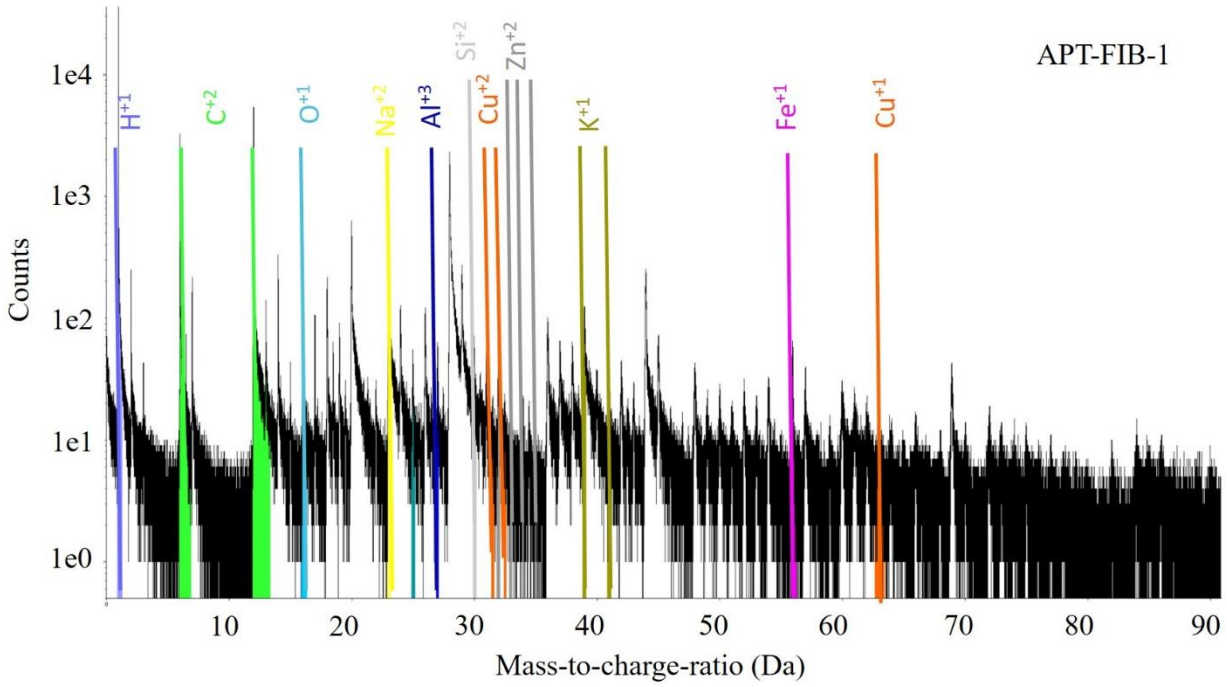

Fig 3-S3: APT mass spectrum for APT-FIB-1: Peaks are color-coded by atomic species showing the positions of H^{+}, C^{+2}, O^{+1}, Na, K^{+}, Al^{3+}, Si^{2+}, $Cu^{2+,1+}$, Zn^{3+} and Fe^{+}.

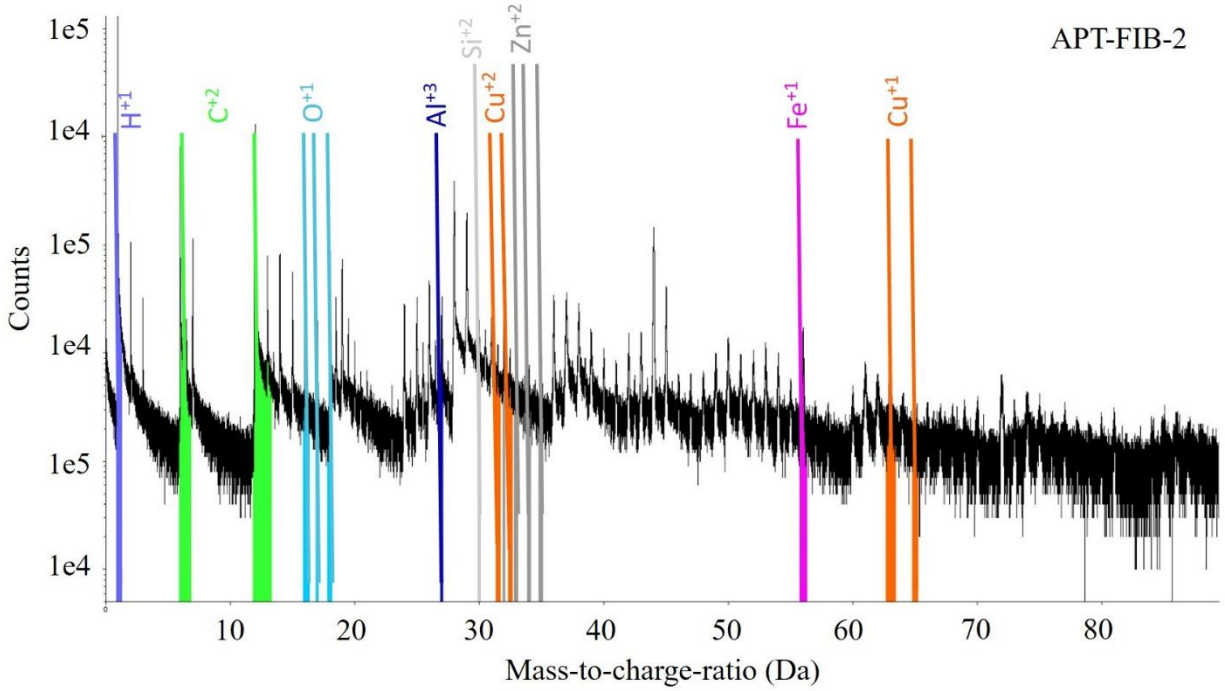

Fig 3-S4: APT mass spectrum for APT-FIB-1: Peaks are color-coded by atomic species showing the positions of H^{+}, C^{2+}, O^{+}, Al^{2+}, Si^{2+}, $Cu^{2+,1+}$, Zn^{2+} and Fe^{+}.

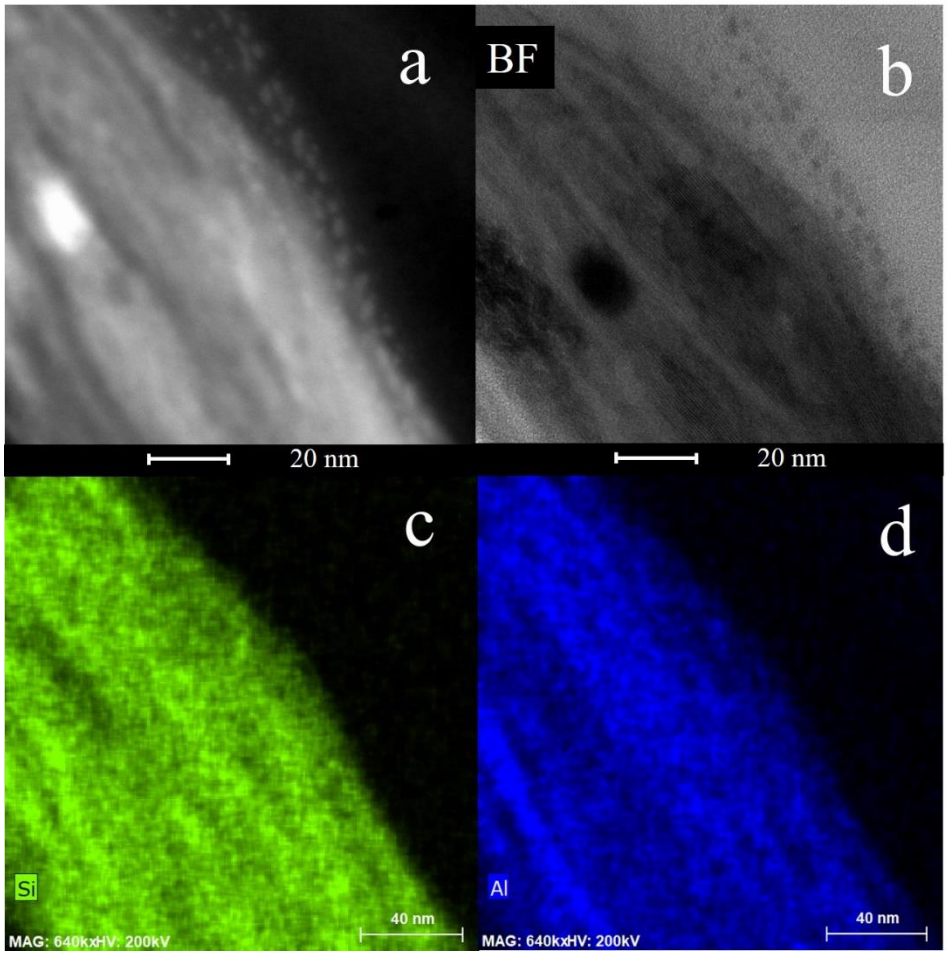

Fig 3-S5: (a)-(d) Exfoliation of silicate phase in the OM matrix of TEM-FIB-1: (a) STEM image, (b) high-resolution TEM image, (c) STEM-EDS chemical distribution map for Si (green) and (d) Al (blue) indicating distinct layers of Si and Al.

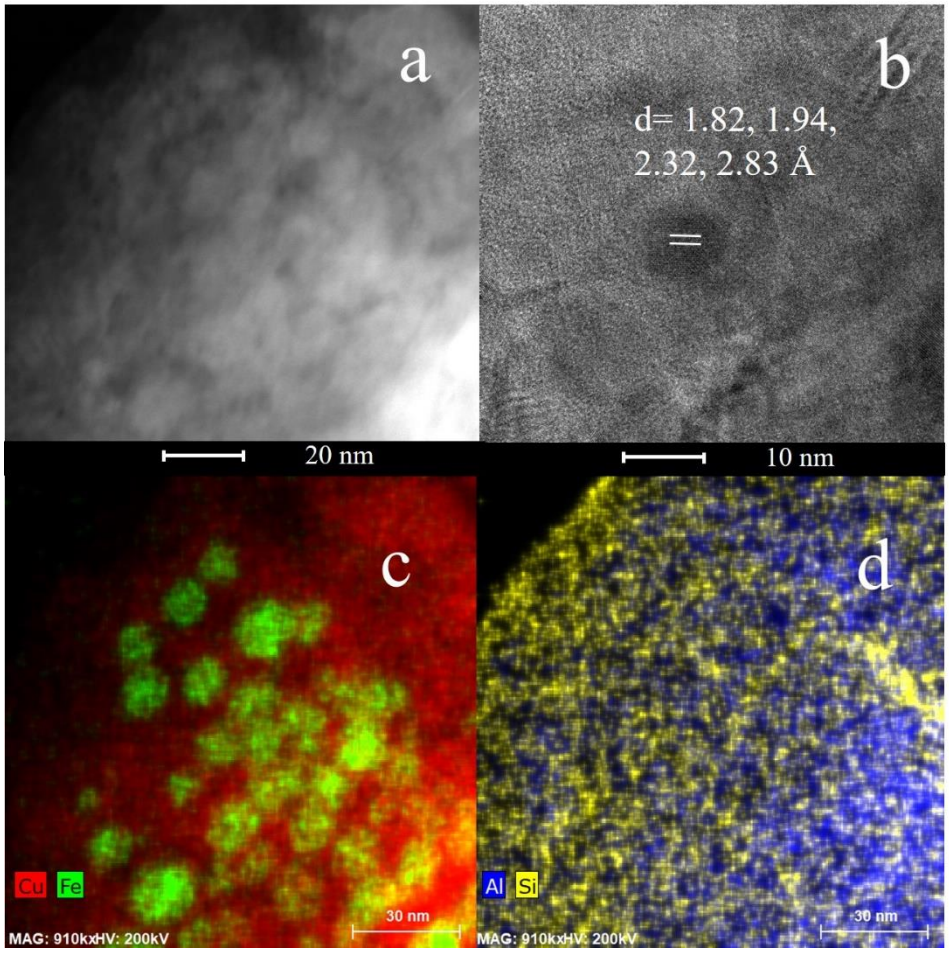

Figure 3-S6 (a)-(d) Aggregation of Fe-(hydr)oxide NP (most likely lepidocrocite) within an amorphous silicate matrix that is embedded in the OM matrix of TEM-FIB-1: (a) STEM image, (b) high-resolution TEM image indicating lattice fringes with *d*= 1.82, 1.94, 2.32, and 2.83 Å and (c)-(d) STEM-EDS chemical distribution maps for (c) Cu (red), Fe (green) and (d) Al (blue) and Si (yellow) indicating the occurrence of Fe-(hydr)oxide NP (most likely lepidocrocite) (average NP size = 10 nm) in an amorphous silicate matrix.

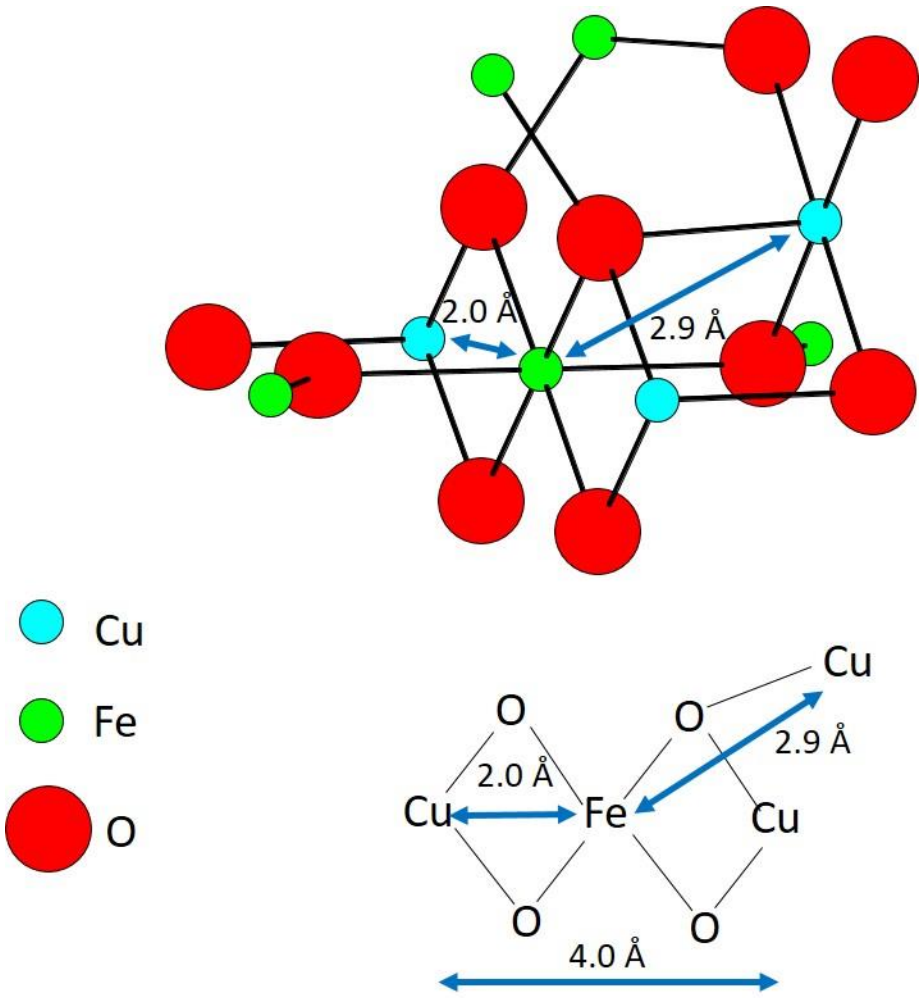

Figure 3-S7 Cu-Cu distance is 4.0 Å if only half the octahedral sites are occupied by Cu in inverse spinel structure.

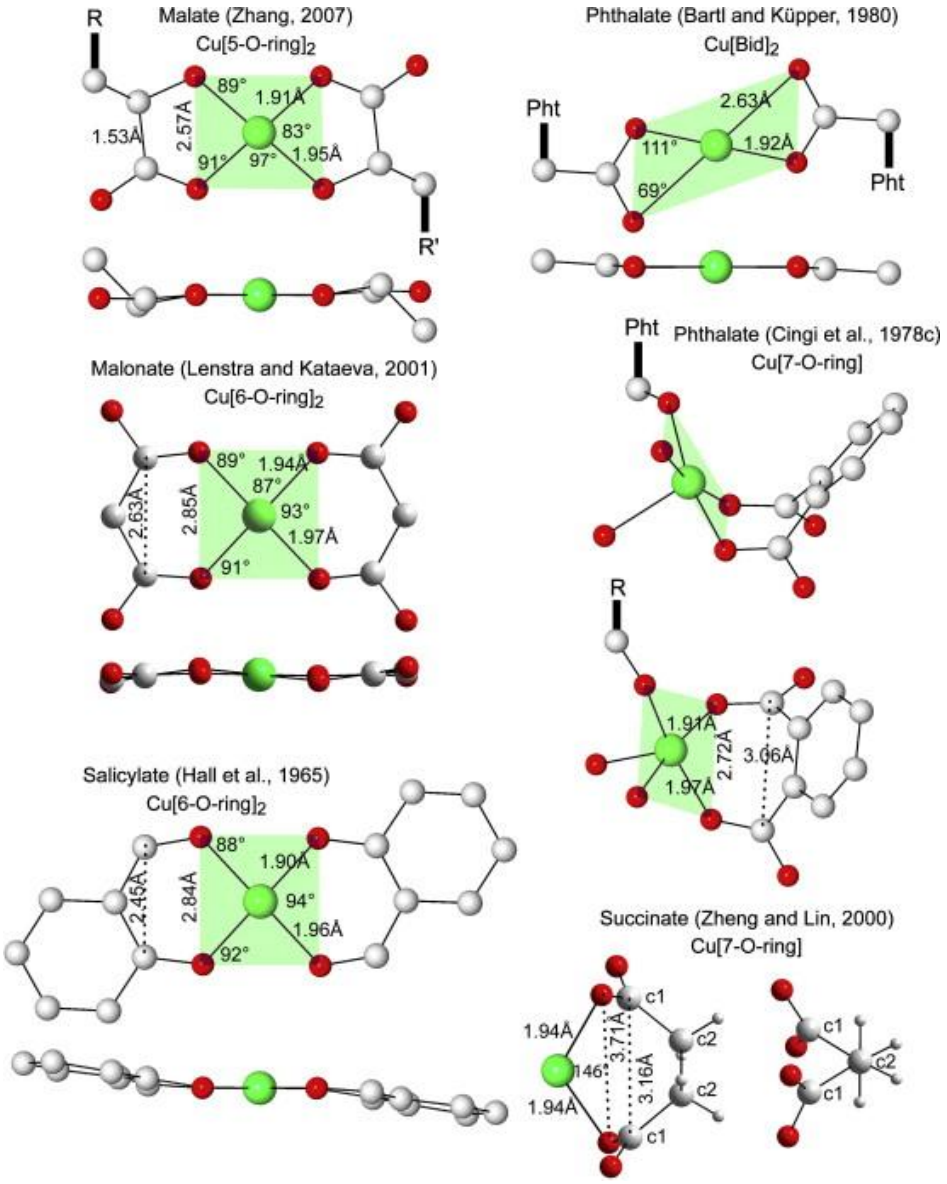

Figure 3-S8 Top- and lateral-views of the geometry of Cu carboxylate chelates (Manceau & Matynia, 2010).

Tables:

Table 3-S1: Selected trace metal(loid) concentrations and physico-chemical parameters of the samples 5A, 7A and 7B.

	Trace metal concentration[a] (ppm)							Physico-chemical parameters			Distance to former smelter complex (km)
Sample	Ag	Co	Cu	Pb	Sb	Sn	Zn	pH	Total C (wt%)	Total S (wt %)	
5A	21.9	173.5	7974	3104.9	32.9	>90	1474	4.7	28.1	0.28	1.8 W
7A	7.4	184.1	2692	1261.9	48.9	>90	4225	5.4	22	0.19	1.8 NE
7B	7.2	88	3829	2023.9	42.6	>90	2178	3.6	22.8	0.37	1.8 NE

[a] Concentrations are reported in ppm except where noted

Table 3-S2: Trace metal(loid) concentrations in all collected samples around the Horne smelter in Rouyn Noranda.

	Trace metal concentration (ppm)							Distance to former smelter complex (Km)
Sample	Ag	Co	Cu	Pb	Sb	Sn	Zn	
1A	18.8	273.2	2864	1759.2	28.4	>90	263	3.5
1B	1.4	68.5	854	225.7	2.2	8.9	118	3.5
1C	19.2	143.1	4138	909.1	25.1	72.3	363	3.5
2A	5.1	295.5	5318	3825.8	26.1	>90	773	3.1
2B	2.6	154.4	789	377.8	4.8	21.5	83	3.1
2C	9.6	81.3	6120	2101.4	12.5	57.0	707	3.1
3A	8.8	124.6	2043	2166.3	13.7	>90	420	2.9
3B	2.7	122.6	1007	718.6	4.7	25.3	255	2.9
3C	1.4	274.8	523	175.9	2.1	7.9	516	2.9
4A	9.2	105.4	2853	601.6	12.9	29.1	656	2.9
4B	11.3	84.6	3419	835.6	14.6	36.1	507	2.9
4C	0.5	81.4	131	52.0	1.4	3.3	169	2.9
5A	21.9	173.5	7974	3104.9	32.9	>90	1474	1.8
5B	23.4	114.5	6916	1691.1	35.4	64.5	1521	1.8
6A	8.1	117.4	3421	494.7	10.1	24.8	615	1.2
6B	6.4	81.8	1740	926.6	15.6	32.4	246	1.2
6C	19.8	118.2	6535	1462.8	18.3	44.4	692	1.2
6F	12.8	99.2	3732	608.5	26.7	32.1	1154	1.2
7A	7.4	184.1	2692	1261.9	49.0	>90	4225	1.8
7B	7.3	88.0	3829	2023.9	42.6	>90	2178	1.8
7C	5.3	118.4	1903	875.1	38.9	>90	1480	1.8
Average	10	138	3276	1248	20	>50	887	

Table 3-S3: Carbon-Nitrogen-Sulfur concentrations in the samples 7A, 7B and 5A; Carbon is measured as both Total carbon (TC) and Total organic content (TOC) in the analysis.

Sample	Wt% N	Wt% TC	Wt% S	Wt%TOC	C/N
7A	1.258	22.074	0.194	17.253	17.549
7B	1.258	22.822	0.365	18.784	15.317
5A	1.676	28.113	0.277	25.112	16.773

References:

Amirault, F., & Burnham, O. (2013). Carbon and Sulfur Analysis in Geological Samples by Combustion-Infrared: Verifying Method Capabilities on New Instrumentation. *Summary of Fieldwork and Other Activities 2013, Ontario Geological Survey Open File Report 6290*, 43-41.

Bas, P., Bostel, A., Deconihout, B., & Blavette, D. (1995). A General Protocol for the Reconstruction of 3d Atom Probe Data. *Applied Surface Science, 87*, 298-304.

Blum, T. B., Darling, J. R., Kelly, T. F., Larson, D. J., Moser, D. E., Perez-Huerta, A., Prosa, T. J., Reddy, S. M., Reinhard, D. A., & Saxey, D. W. (2018). Best Practices for Reporting Atom Probe Analysis of Geological Materials. *Microstructural Geochronology: Planetary records down to atom scale*, 369-373.

Burnham, O. M. (2017). Inductively Coupled Plasma Mass Spectrometry Analysis of Trace Elements in Geological Samples after Aqua Regia Extraction at the Geoscience Laboratories: Revised Capabilities Resulting from New Instrumentation, in Summary of Field Work and Other Activities. *Open File Report 6333, Ontario Geological Survey*, 31.

Manceau, A., & Matynia, A. (2010). The Nature of Cu Bonding to Natural Organic Matter. *Geochimica et Cosmochimica Acta, 74*(9), 2556-2580.

Miller, M. K. (2012). *Atom Probe Tomography: Analysis at the Atomic Level*: Springer Science & Business Media.

OECD, D. (2002). Guidelines for the Testing of Chemicals: Leaching in Soil Columns: OECD-Organisation for Economic Cooperation and Development.